UNIVERSIDAD DE NAVARRA
ESCUELA SUPERIOR DE INGENIEROS
SAN SEBASTIÁN

Laser-nanostructured metal oxide semiconductors
for conductometric gas sensors

DISSERTATION

presented to obtain the degree of Doctor of Philosophy by the University of Navarra by

LAURA PARELLADA MONREAL

Donostia-San Sebastián, January 2019

Be concerned about doing good work
Patti Smith

Per l'Eva i l'Alba,
amb elles tot ha sigut molt més fàcil

Acknowledgements

En primer lugar, me gustaría agradecer al Ceit-IK4 y a la Universidad de Navarra por darme la oportunidad de realizar esta tesis.

En segundo lugar, dar las gracias de manera especial a las dos personas que han dirigido y codirigido mi tesis. A Gemma García Mandayo por confiar en mí, guiándome cuando ha sido necesario, aunque siempre dejándome vía libre para exponer nuevas ideas y a Irene Castro Hurtado por su ayuda en el laboratorio y correcciones en ámbitos más físicos y técnicos.

Quiero agradecer la ayuda ofrecida desinteresadamente a varias personas con quien he compartido pasillo durante estos tres años y medio: Isabel Ayerdi, Enrique Castaño, Oihane Beldarrain y en especial, a Gorka Muñoz, sin él no podría haber llevado a cabo esta tesis.

También me gustaría agradecer las discusiones, debates y conversaciones con los que han sido mis compañeros de despacho y con los doctorandos del despacho 023, siempre dispuestos a echarte una mano en cualquier tema: Nerea, Imanol, Iñigo, Itziar, Oihane M., Miguel, Noemí, Alejandro y Sergio. Y dentro del Ceit, personas con quien he tenido la suerte de coincidir y me han ayudado: Javi y Lander.

I would also like to express my deep gratitude to the people who welcomed me in the University of Ferrara and helped me to take profit of my stage during the four coldest months of my life, so far: Sandro, Giulia, Cesare, Davide, Silvia and Marinela.

También quiero mostrar mi agradecimiento a investigadores con los que he tenido el privilegio de discutir sobre resultados de la tesis y de los que he aprendido mucho: Pep Bassa, Daniel Gamarra y especialmente Lionel Presmanes, gracias por darme la oportunidad de ir a Toulouse y realizar los experimentos Raman.

Gracias a mis amigos he podido distraerme de la tesis, salir, hacer viajes y han hecho que esta experiencia haya sido mucho más llevadera:

A Jordi Vila, la persona que em va fer escollir la carrera de Física i a qui mai li podré agrair suficientment.

Als meus amics de Barcelona, els de tota la vida, perquè tot i la distancia, sempre m'han fet costat, han vingut a veure'm a Donostia quan han pogut i canvien agendes cada cop que baixo a Barcelona: Roger, Maria, Naiara i Clara. I també als meus amics de Física, perquè em van fer veure que podia fer el doctorat i sempre m'han fet riure en els moments durs del recorregut: Irini, Lluís, Maria, Núria, Aleix, Ignasi, Néstor i Marc.

A los amigos de mi pueblo, Salillas, con quien coincido más bien poco, pero siempre

me han dado muchos ánimos: Ana, Raquel, Sandra y Rubén.

I would also like to thank the people with whom I discovered the scientific and research world in Grenoble, they were a key piece in this path: Ellie, Catalinda, Eric, Nikos, Stefanos and Martine.

Y a mis amigos de Donostia, que me han ayudado a disfrutar de esta bonita ciudad y a desconectar del trabajo. Y aunque la mayoría se dediquen a temas muy distintos, sé que han hecho un esfuerzo por entender mi doctorado: Caro, Ariane, Helena, Antia, Júlia, Julen, Victor, Carlota, Fernando, Esteve y Sergio.

Finalmente, y más importante, quiero dar las gracias a toda mi familia, pero en especial a mis dos tías abuelas favoritas, a mi hermano Daniel y su nueva familia Maria, Eva y Alba, que me han traído muchas alegrías durante este periodo y a mis padres, por la confianza y soporte incondicional que he recibido siempre.

A todos, eskerrik asko.

Abstract

Nanostructured materials present different physical properties in comparison to their bulk counterparts and the integration of this type of materials in conventional devices, such as gas sensors, can improve some of their characteristics such as sensitivity, selectivity and response. These enhanced features are important for the development of reliable gas sensors. In particular, nanostructuration of semiconductor metal oxides has been widely researched to be applied in conductometric gas sensors.

The two major drawbacks of most nanostructuring techniques are the low velocity of the process, not scalable for mass production and the need to transfer the nanostructures to the sensing device (ex-situ approaches). Hence, the present work studies the gas sensing performance of semiconductors nanostructured by two top-down techniques that are fast, inexpensive, in-situ process and automatable: direct laser interference patterning (DLIP) and femtosecond laser subwavelength patterning.

The DLIP is a non-contact technique that uses the interference patterns generated by two or more coherent laser beams to directly structure materials. On the other hand, femtosecond laser subwavelength patterning generates laser-induced periodic structures (LIPSS) when linearly polarized radiation interacts with a solid.

This work focuses on the detection of NO_2, since it is one of the most common pollutants, and needs to be detected in very low concentrations. In fact, the recommendation from the Scientific Committee on Occupational Exposure Limits for Nitrogen Dioxide of the European Commission establishes 0.5 ppm as the 8-hour TWA[1].

In particular, this thesis gathers the study of three different type of laser nanostructured semiconductor gas sensors for the detection of low concentration of NO_2: ZnO based sensors processed by DLIP, ZnO based sensors nanostructured with LIPSS and WO_3 based sensors processed by DLIP. In all the approaches, a response improvement has been obtained by the nanostructured sensors compared with classically annealed devices, pointing out the laser technologies potential.

Furthermore, the study of the operating conditions influence (flow and position of the sensor inside the chamber) on the sensors performance is investigated comparing experimental results with gas flow simulations. Finally, the integration of the fabricated sensors into a wireless platform is included in this dissertation.

---

[1]TWA is the employee's average airborne exposure in any 8-hour work shift of a 40-hour work week which shall not be exceeded.

Contents

List of Figures

List of Tables

Chapter 1

Objectives and framework

1.1 Objectives

The fundamental objective of this thesis is the study of nanostructured materials generated by laser techniques and their application in solid state conductometric gas sensors. In particular, the study of zinc oxide (ZnO) and tungsten oxide (WO_3) nanostructured by direct laser interference patterning technique (DLIP) and by femtosecond laser subwavelength patterning for the detection of nitrogen dioxide (NO_2). This fundamental objective implies several technical objectives that will be enumerated bellow:

1. Integration of laser techniques (DLIP and femtosecond laser subwavelength patterning) into the fabrication process of a gas sensor.

2. Development of ZnO nanostructures fabricated by DLIP and study of their application as sensing layer for NO_2 detection.

   - Study of the transient temperature reached by the sample during the nanostructures formation by DLIP process through the simulation of the heat transfer equation. Determination of the theoretical annealing threshold temperature.
   - Study of the morphological, structural and compositional properties of the nanostructures on the surface and in depth.
   - Study of the sensing properties for NO_2 detection at the optimal temperature.

3. Development of ZnO laser-induced periodic structures (LIPSS) generated by femtosecond laser subwavelength patterning and their application as sensing layer for NO_2 detection.

   - Study of the morphological and structural properties of the nanostructures.
   - Study of the selectivity of the sensor devices.
   - Study of the operating temperature influence on the sensing properties for NO_2 detection.
   - Study of the long-term stability as a NO_2 sensor.

4. Development of WO_3 nanostructures processed by DLIP and their application as sensing layer for NO_2 detection.

   - Study of the morphological, structural and compositional properties of the nanostructures on the surface and in depth.

   - Study of the operating temperature influence on the sensing properties for NO_2 detection.

   - Study of the selectivity of the sensor devices.

   - Study of the NO_2 detection mechanism.

5. Study of the influence of operating conditions in the sensor properties.

   - Study of the influence of the sensor position and gas flow inside the test chamber on the final sensor performance. Comparison of experimental results with gas flow simulations.

6. Sensor implementation in a wireless platform to operate in a real environment. Comparison with laboratory measurements.

1.2 Framework

The present work has been carried out at the Transportation and Sustainable Mobility Group at Ceit-IK4 and at the "Sensor Laboratory" (SL) at the University of Ferrara (UNIFE). Funding for this work has been provided by the following projects:

- "Technological innovation in micro and nanosensors for air quality monitoring and environmental control" (TEMIN-AIR) and "Technological innovation in micro and nanosensors for air quality monitoring and environmental control" (TEMIN-AIR +). These projects were provided by the Ministry of Economy and Competitiveness (MINECO) of Spain under the "Programa Estatal de I+D+i Orientada a los Retos de la Sociedad" for the periods 2014-2017 and 2017-2019, respectively.

  The teams involved in these projects are: the Department of Micro and Nanosystems of the Micro-Electronics Institute of Barcelona (IMB-CNM CSIC), the Department of Electronics of the University of Barcelona (UB), The Institute for Physical and Information Technologies (ITEFI-CSIC), the Department of Electrical Engineering and Electronics and Automatics of the University of Extremadura (UEX) and the Department of Electrical Engineering of the Polytechnic University of Catalonia (UPC).

- "Microtechnologies as a motor of the development of advanced cyber-physical systems for smart factories" (MICRO4FAB) and "Microtechnologies as a motor of the development of advanced microsystems for smart factories. Structural monitoring and bio-chemical substance detection in production means" (μ4F). These projects were provided by the Basque Government within the framework of the ELKARTEK

program for the periods March 2016-December 2017 and June 2017-December 2018, respectively.

The teams involved in these projects are: IK4-Tekniker foundation, Donostia International Physiscs Center, Basque Center for Materials, Applications and Nanostructures (BCMaterials) foundation, Azti foundation, Gaiker foundation, Tecnalia Research & Innovation foundation, Ikerlan cooperative society, Ikor technology center SL, Mondragon Goi Eskola Politeknikoa Jose Maria Arizemendiarrieta Cooperative Society, University of Navarra and University of the Basque Country.

The four months stay at UNIFE were financed by the Navarra Government through the "Programa de ayudas predoctorales de movilidad internacional".

During the development of this thesis, there was a collaboration with the group of the researcher Lionel Presmanes at the University of Toulouse.

1.3   Document layout

The present document is organized in seven chapters and one appendix, where the developed work and obtained results are detailed and discussed.

The first chapter is the present one, where the main objectives of this thesis are exposed jointly with the framework in which it has been developed.

Chapter 2 introduces solid state gas sensors, focusing on semiconductor metal oxides. Then, a review of nanostructuring techniques for gas sensor applications is presented with a detailed description of DLIP and femtosecond laser subwavelength patterning techniques. Furthermore, theoretical aspects regarding gas detection mechanisms are approached and finally, a review of the state of the art of ZnO and WO_3 based sensors for NO_2 detection is carried out.

The three following chapters cover the fabrication, characterization and results obtained for the three different types of gas sensors studied in this thesis: ZnO based sensors nanostructured by DLIP, ZnO based sensors nanostructured with LIPSS and WO_3 based sensors nanostructured by DLIP.

In chapter 6, the influence of gas flow conditions in the detection are studied comparing experimental and simulation results and the sensor integration in a wireless platform is included.

The last chapter of this dissertation (chapter 7) concludes with a comparison between all the fabricated sensors in this thesis, a summary of the main conclusions and future work suggestions.

Lastly, Appendix A presents the scientific contributions of this work.

Chapter 2

Solid state gas sensors: semiconductor metal oxides

In order to contextualize this PhD thesis, a brief introduction to different types of solid state gas sensors is first presented. Secondly, semiconductor metal oxide gas sensor properties are briefly reported and nanostructuring techniques, especially those using laser technologies are explained with the focus on gas sensing devices.

Besides, a review of the semiconductor band model, as well as the detection mechanism in solid state conductometric gas sensor is introduced. Finally, the necessity of NO_2 detection is justified, jointly with the description of the NO_2 detection mechanism for ZnO and WO_3.

2.1 Solid state gas sensors

Sensors are devices that detect physical magnitudes from the environment (variations of light, heat, sound, pressure, etc.) through the modification of some of their properties. Specifically, solid state gas sensors are based on materials able to change their electrical properties depending on the chemical environment. This particular feature can be used to measure concentrations of different gas species [1]. There are several solid state gas sensors based on that principle, such as conductometric or chemoresistive, catalytic and solid-electrolyte sensors. All of them are used for the detection of harmful compounds such as volatile organic compounds (VOC's), nitrogen oxides (nitrogen monoxide (NO) and NO_2) and combustible gases.

Conductometric sensors are based on the reactions that take place between the surface of the material and the gases in the atmosphere, modifying the material conductivity. Usually, the adsorption of the gases on the surface of the material leads to a change on its conductivity. The most important materials with chemoresistive properties are metal oxide (MOX) semiconductors and carbon based materials.

MOX semiconductors devices are very popular in the current market of chemical sensors since there is a wide range of them with different electronic, optical and chemical characteristics [2]. While the most investigated material is tin oxide (SnO_2), other

compounds are rather getting importance such as ZnO, WO$_3$, indium oxide (In$_2$O$_3$) or copper oxide (CuO) [3]. Detailed characteristics of MOX semiconductor gas sensors will be explained in the following section.

Since the detection of individual gas molecules adsorbed on graphene was reported [4], carbon based materials have also been widely studied as promising materials to, for example, lower the working temperature of the common MOX [5, 6]. In spite of that, this specific branch of the conductometric gas sensors field is still far from the commercial exploitation.

Catalytic sensors or pellistors are based on catalytic materials and are mainly used to detect combustible gases. Combustible gases burn when they reach an ignition temperature. However, in the presence of catalytic materials, the ignition temperature can be lowered, what is known as a catalytic combustion. When the gas is burned over the catalytic material, the catalytic material releases heat, modifying its resistance.

The catalytic sensors consist of two platinum (Pt) coils, each embedded in a ceramic bead. The Pt coils have two functions; they act as a heater as well as being a resistive temperature sensor. One of the beads is the sensitive element, which is activated with a suitable catalyst and the other is the compensator element, which is inert and has no catalyst on its surface. The beads are mounted in a Wheatstone bridge circuit to facilitate the comparison of the coil resistances as illustrated in Fig. 2.1. A voltage supply heats up both coils, so the beads are raised to high temperatures, in the range between 300 °C and 500 °C depending on the target gas. In the presence of the combustible gas, the temperature of the activated bead increases, which results in a change in the electrical resistance of the activated coil. This creates an imbalance in the Wheatstone bridge circuit, which constitutes the sensor signal [7].
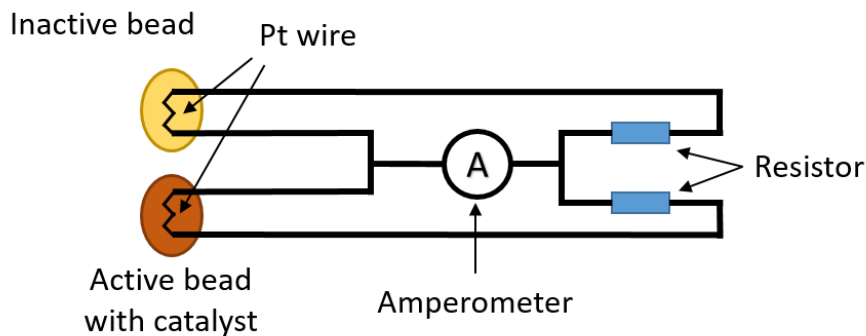
Figure 2.1 – Wheatstone bridge circuit connecting the active and inactive beads in a pellistor. Adapted from [7].

Moreover, catalytic materials can also be combined with MOX semiconductor materials as conductometric gas sensors in order to accelerate specific surface reactions with the atmosphere, increasing the selectivity. Nobel metals such as palladium (Pd), Pt or gold (Au) are the favourites for this purpose [8–10].

Solid-electrolyte sensors are based on the conduction of ions, instead of electrons. The basic configuration is the potentiometric one and consists of a solid electrolyte located between two conducting electrodes. Typically, one of the electrodes is in contact with a

reference gas, while the working or sensing electrode is in presence of the testing gas. Due to the reduction or oxidation reaction that happens in the sensing electrode, ion conductivity is produced through the electrolyte. By measuring the potential difference between the electrodes, one can determine the concentration of the chemical species in contact with the sensing electrode [1]. A planar configuration of a potentiometric solid-electrolyte gas sensor is shown in Fig. 2.2 (a), but other sensing configurations such as amperimetric or mixed potential sensors have also been employed for solid-electrolyte sensors [11].
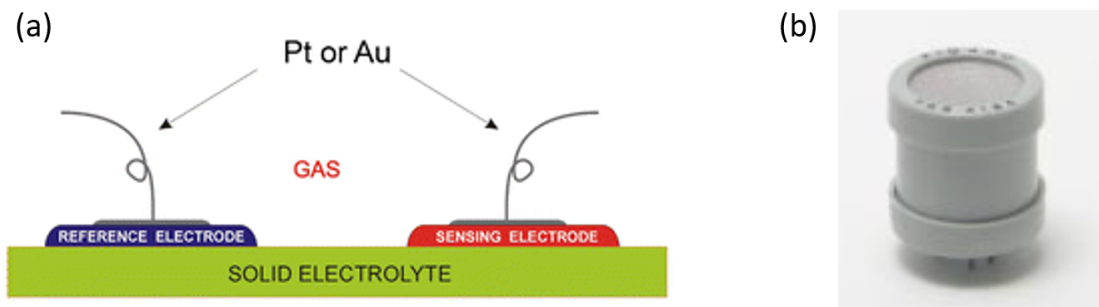
Figure 2.2 – (a) Planar potentiometric configuration and (b) commercial CO_2 potentiometric sensor (TGS 4160) from Figaro Company. Adapted from [12].

In Fig. 2.2 (b), a commercial carbon dioxide (CO_2) potentiometric solid-electrolyte detector from Figaro company is presented. The device is able to detect from 350 to 50.000 part per million (ppm) of CO_2 and it has an adsorbent (zeolite) at the top of the sensor cap to reduce the influence of interference gases. As oxygen detector, yttria-stabilized zirconia (YSZ) is the most used electrolyte in automotive applications employed in Lambda sensors [13].

Among all the solid state sensors described above, electrochemical sensors are the most used for gas detection such as carbon monoxide (CO) and nitrogen oxides, because MOX semiconductors present several challenges regarding stability, reproducibility and selectivity. Nevertheless, due to the inexpensiveness and easy miniaturization of MOX devices, they can be adequate for many applications that do not require a high selectivity, reason why they are increasing their presence in the market for air quality applications and VOC's detection. Moreover, selectivity can also be improved by the algorithms used in the electronic noses, made up of MOX sensor arrays [14].

2.2   Semiconductor metal oxide gas sensors

After the demonstration of germanium (Ge) conductivity change under atmosphere variation [15], in the early 60's, T. Seiyama reported the gas sensing properties of ZnO thin films [16] for the first time. About ten years later, N. Taguchi patented the first chemoresistive gas sensor device based on a SnO_2 film [17], which is nowadays the most available material in the market due to its high sensitivity to a large number of gas species at relatively low operating temperatures.

2.2.1   Sensor configuration

On semiconductor MOX, the reactions that occur on the material surface are temperature dependent. For this reason, a heater is implemented in the sensor device, in order to achieve the desired temperatures. Moreover, in order to measure the MOX conductivity as a function of the atmosphere, electrodes are needed.

With these three key elements (heater, electrodes and MOX sensing layer) different sensor configurations have been designed and fabricated as shown in Fig. 2.3. In Fig. 2.3 (a), the structure of the first sensors is presented: a sintered block with two metal electrodes, where one of them was used as a heater. Later, a thin alumina tube covered by a heavy coating was used with a pair of electrodes welded to the tube and the heater inside of it (Fig. 2.3 (b)). The configuration shown in Fig. 2.3 (c) is one of the most used nowadays. The sensing layer is fabricated on a planar alumina substrate over the electrodes and the heater is printed on the other side of the substrate. The sensing layer can vary from thin and thick films to nanostructures.
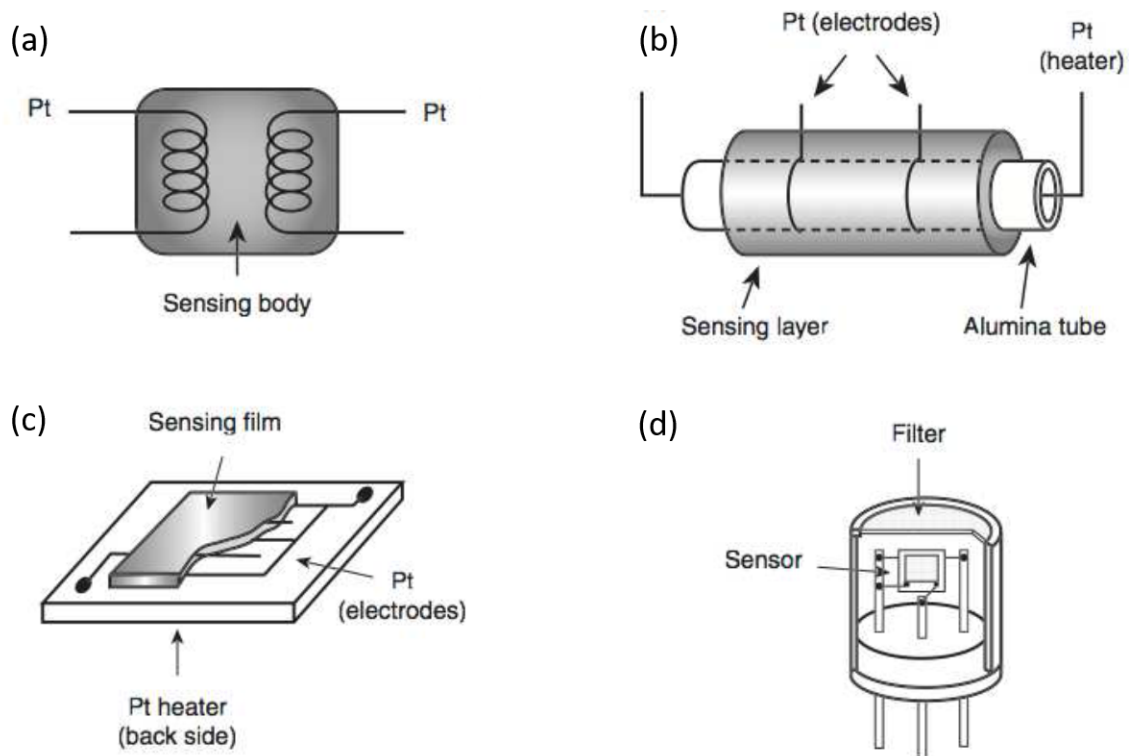
Figure 2.3 – Device configurations: (a) Sintered block, (b) thin alumina tube-coated layer, (c) thin film or screen printed thick film and (d) practical sensor element assembling sensor device, metal cap and filter. Adapted from [11].

From the early 80's, silicon micromachining became considerably important, what was used to generate microsensor devices with low power consumption (Fig. 2.3 (d)). As shown in Fig. 2.4 (a) thermally insulated heating elements suspended on a dielectric membrane was used to support the metal electrodes with the sensitive layer on top [11]. In Fig. 2.4 (b), a micromachined sensor fabricated in the Micro-Electronics Institute of

Barcelona (CNM) is shown: the sensor substrate consists on a four-element integrated micro-hotplate array on standard transistor outline (TO)-8 constructed using microsystem technology.
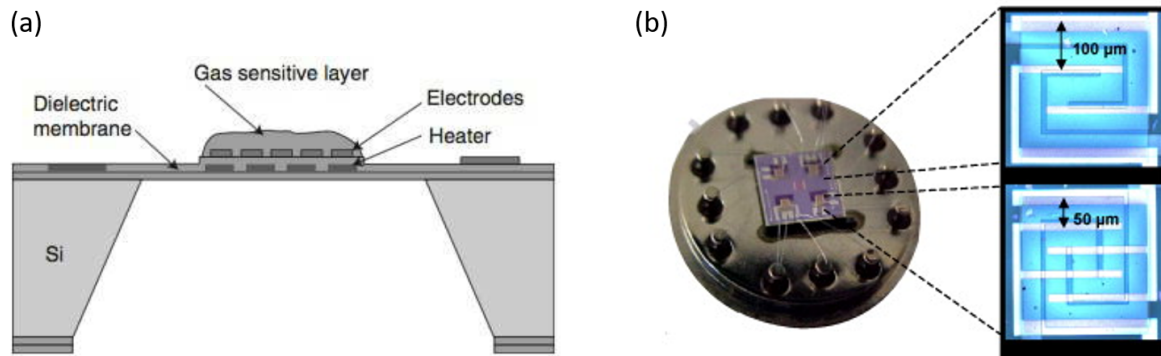
Figure 2.4 – (a) Cross-sectional diagram of a micromachined MOX gas sensor and (b) view of a micro-array of four sensors mounted on standard (TO)-8 and the detailed views of the micromachined sensor membranes with interdigitated electrodes with two different gaps (100 and 50 μm). Adapted from [11] and [18].

The influence of the electrode material, as well as the geometry, have been proved to be significantly important for the gas sensing mechanism [19, 20]. Besides, different heating strategies have been studied to improve the sensor efficiency, from self [21] and dynamic [22] heating to even a combination of both [23]. Despite that, the continuous heating is still the most commonly used strategy.

2.2.2 Operating principle

As mentioned before, semiconductor MOX gas sensors need to work at high temperatures in order to detect gas concentrations in air (usually between 200 °C and 400 °C), so the first step during the gas detection is heating the sensor to the desired temperature (Fig. 2.5 (a)). At high temperatures, oxygen molecules dissociate and are adsorbed on the semiconductor surface, getting electrons from the material. Once the oxygen adsorption has reached an equilibrium stage, the conductance (G) of the semiconductor gets constant (Fig. 2.5 (b)). When the target gas is in contact with the semiconductor, interaction between the molecules, the oxygen species adsorbed at the surface and the MOX occurs, modifying the conductance of the sensitive layer (Fig. 2.5 (c)) until a new conductance value gets stable (Fig. 2.5 (d)). Finally, when the sensor is exposed again to air, the previous value of the conductance is reached (Fig. 2.5 (e)).

Depending on the nature of the semiconductor material (n-type or p-type) and the kind of gas to be detected (reducing or oxidizing), the conductance will increase or decrease in the presence of the gas. Four different situations could take place, as it is shown in Table 2.1.
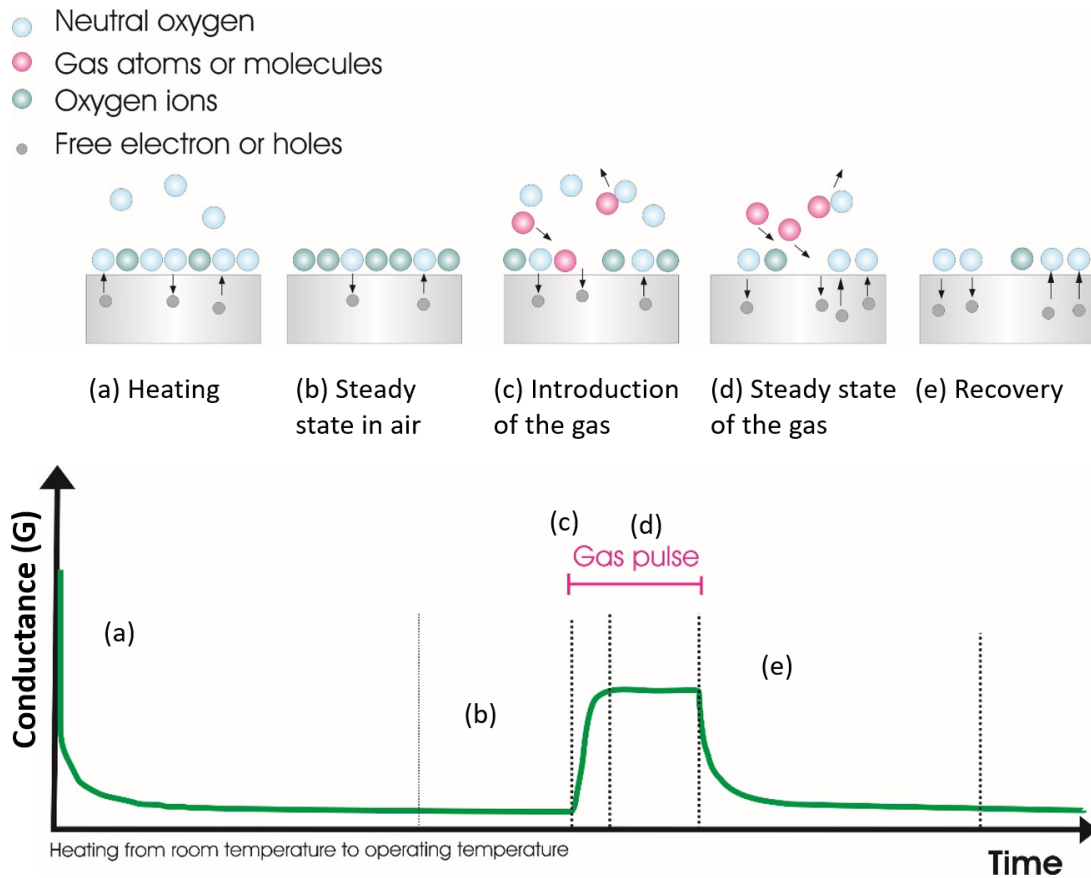
Figure 2.5 – Steps followed during the gas detection. (a) Heating of the sensing device, (b) steady state in air, (c) introduction of the gas, (d) stabilization in the presence of the gas and (e) recovery of the conductance in the presence of clean air.

Type of semiconductor	Type of gas	Conductance variation $(\triangle G)$[a]
n	Oxidizing	-
n	Reducing	+
p	Oxidizing	+
p	Reducing	-

Table 2.1 – Conductance variation for n and p-type semiconductors under reducing or oxidizing atmospheres.

---

[a]$\triangle G = G_{gas}$ - G_{air}, where G_{gas} and G_{air} are the conductance in the presence of gas (reducing or oxidizing) and air, respectively.

2.2.3   Influencing parameters

In this section, some of the most important parameters affecting the final response of a sensor device will be described. Two of them are related to the fabrication process (fabrication technique and annealing treatment), while the rest depend on the detection conditions (working temperature, chamber shape, sensor position inside the chamber, gas

flow and data acquisition procedure).

- **Fabrication process**

  Regarding the microstructure and stoichiometry, the fabrication process plays a key role. On one hand, the **fabrication technique** will determine the morphology, thickness and nanostructure characteristics, among others. And on the other hand, the **post-annealing treatment** will affect the final crystal structure and also the grain size.

  For thin film fabrication techniques, there exists a morphology transformation with the thickness because the grain size increases when the material becomes thicker. By contrast, in the case of thick films, where a higher porosity is obtained, thickness does not affect the grain size. Consequently, the conduction mechanism for thin films will depend on the thickness, while for the thick films will be strongly influenced by the porosity of the film [24].

  Since the gas detection is performed at elevated temperatures, high annealing treatments are applied to the sensing materials to stabilize morphological and structural properties. Thus, temperatures higher than the optimal working temperature are required. Materials will usually crystallize in different crystal structures depending on the annealing [25]. Several studies have reported the influence of annealing temperature on the final characteristics of gas sensor devices [26, 27], due to the modification in grain size, effective surface area and stoichiometry.

- **Gas detection conditions**

  As will be studied in this thesis and especially in chapter 6, the detection conditions chosen when the gas detection is taking place influence the final response of a sensor device. The **working temperature** of the device is one of the most studied parameters because the gas detection mechanism is strongly modified by the temperature, as it will be shown in the following sections. Nevertheless, the magnitude of **gas flow** and the **chamber shape** also affect the dynamics of the response signal. This is shown in the work of F. Annanouch [28], where experimental results contrasted with gas flow simulations are discussed for two different chambers (cross- and a boat-shape). As a result, the boat-shape chamber presents higher homogeneous gas concentration inside the chamber, leading to a faster and higher response of the sensor.

N. Yamazoe wrote one of the most important publications discussing how to improve the MOX sensing performance in 1991 [29]. It was established that the crystallite size of the semiconductor MOX is one of the key issues on the sensor performance. Henceforth, researchers have been focusing on new strategies to control the crystallite size of the materials, increasing the interest on the nanostructured materials.

2.3   Nanostructuring techniques

Nanostructured and nano-patterned semiconductor surfaces are of great importance in nanotechnology, since they can modify material characteristics such as wettability,

adhesion [30], electrical and optical properties [31]. Nanopatterning has also been widely used as a template to grow ordered nanostructures [32] and can be implemented in a large amount of applications, from optoelectronics [33] and solar cells [34] to microsensor devices [35].

In the recent years special attention has been paid to nanostructured materials for gas sensors since they open a window of distinctive physical properties for a wide range of materials [36] and the physics behind is based on surface reactions [37, 38]. The group of E. Comini published the first chemical sensor based on nanobelts in 2002 [39] and since then many other nanostructures have been employed to improve the performance of gas sensing devices [40–43].

As mentioned in the previous section, structural and morphological characteristics of the nanostructures can be tuned depending on the preparation method. Consequently, there is a need to deeply understand the key effects of each nanostructuring technique, because this would lead to a controlled modification of MOX semiconductors properties for gas sensing purposes.

Nanostructuring techniques can be divided into two main approaches: bottom-up and top-down.

- **Bottom-up** approaches consist of the self-assembly process of the atoms or molecules, leading to the formation of the nanostructures. Therefore, the crystallization of the material can be controlled. During self-assembly, the physical forces operating at the nanoscale are used to combine basic units into larger stable structures.

  From vapor phase, nanostructures can be grown via vapor-liquid-solid mechanism (VLS) using a metal catalyst nanoparticle to continuously feed the one-dimensional growth [44] (see Fig. 2.6). Gold is commonly used as a metal catalyst since it does not react with the gas carriers such as nitrogen, oxygen and hydrogen. The source material is evaporated and transported by the carrier gas to the nucleation site provided by metal seeds. The liquid droplet is supersaturated by the source material, so the precipitation occurs and the nanostructure starts growing. Several MOX have been grown by this mechanism and characterized as gas sensing devices like SnO_2 [45] and niquel oxide (NiO) [46].

  Another growth method from a vapor phase source is via vapor-solid (VS) mechanism. This method has the advantage that is catalyst-free. The source material is evaporated near its melting point, transported and then direct condensation is produced on the substrate, which is maintained at lower temperature. The first seed crystals deposited act as nucleation sites for the subsequent atoms, so directional growth is obtained. Examples of this growth mechanism for sensing applications are SnO_2 in [47] and ZnO in [48].

  Other group of techniques use liquid sources to grow nanostructures. Solution phase growth is performed at room temperature, so less expensive equipment is needed. The growth can be carried out assisted by a template or not.

  Hydrothermal methods and electrospinning are nanostructuring techniques used for sensing applications using a solution source phase without the need of a template. The result are arrays of nanowires with poor vertical alignment.
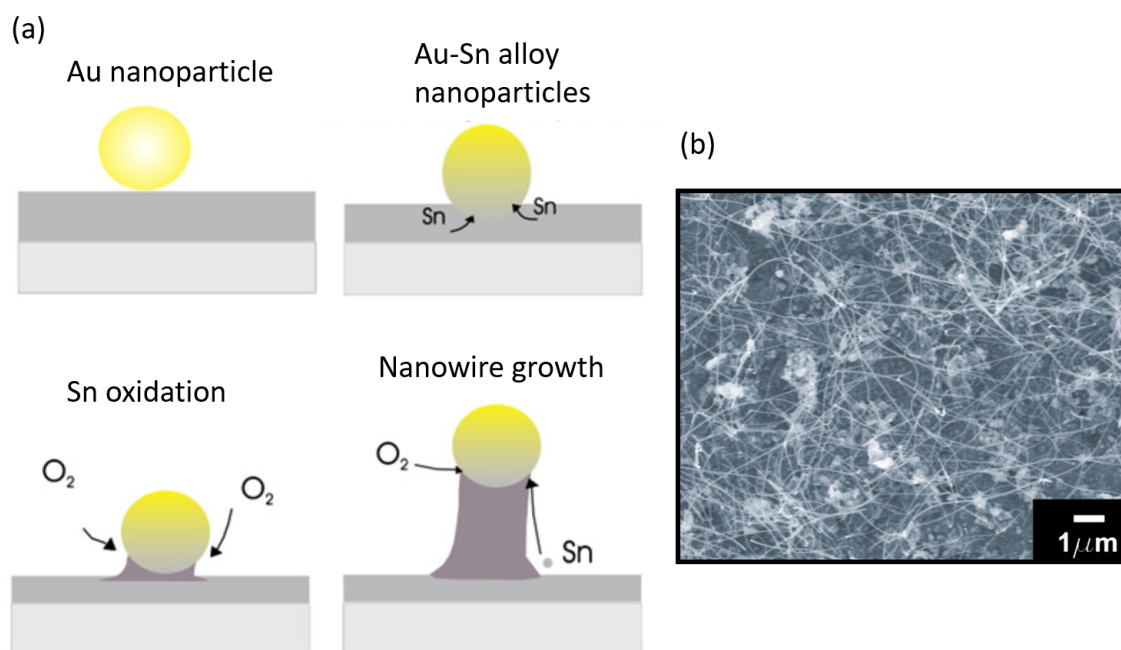
Figure 2.6 – (a) VLS mechanism of SnO_2 nanowire growth and (b) scanning electron microscopy (SEM) image of the SnO_2 nanowires grown by VLS. Adapted from [45].

Hydrothermal processes can grow single crystals from an aqueous solution placed in an autoclave at high temperatures (between 100 °C and 300 °C) and under relatively high pressure (higher than 1 atm) conditions. By contrast, electrospinning uses an electrical charge to force the formation of a matrix of fine fibers (see Fig. 2.7). A solid fiber is produced as the electrified jet is continuously stretched due to the electrostatic repulsions between the surface charges and the evaporation solvent [11]. In this case, the nanostructures produced are usually polycristalline. A great number of oxides have been synthesized by hydrothermal methods [43, 49, 50] and electrospinning [51, 52] to fabricate chemical sensors.

Solution phase template assisted methods are normally not employed for gas sensing applications, so they are beyond the scope of this review.

- **Top-down** approaches are based on a combination of photolithography, thin film deposition techniques, and etching steps. Projection lithography techniques are able to generate nanostructures with dimensions roughly equal to the wavelength of the exposure source (for example, 248 nm if using a krypton fluoride (KrF) excimer laser) [53]. In order to decrease the size of the resulting features, different lithographic techniques have been developed: extreme ultraviolet photolithography (EUV), electron beam lithography (EBL), ion beam lithography (IBL), nanoimprint lithography (NIL), scanning probe lithography (SPL) and laser interference lithography (LIL).

  Among them, EBL is used for gas sensing applications. An electron beam is addressed to the material surface, which is covered by an electron sensitive resist. The patterns drawn on the resist can be afterwards transferred into the material
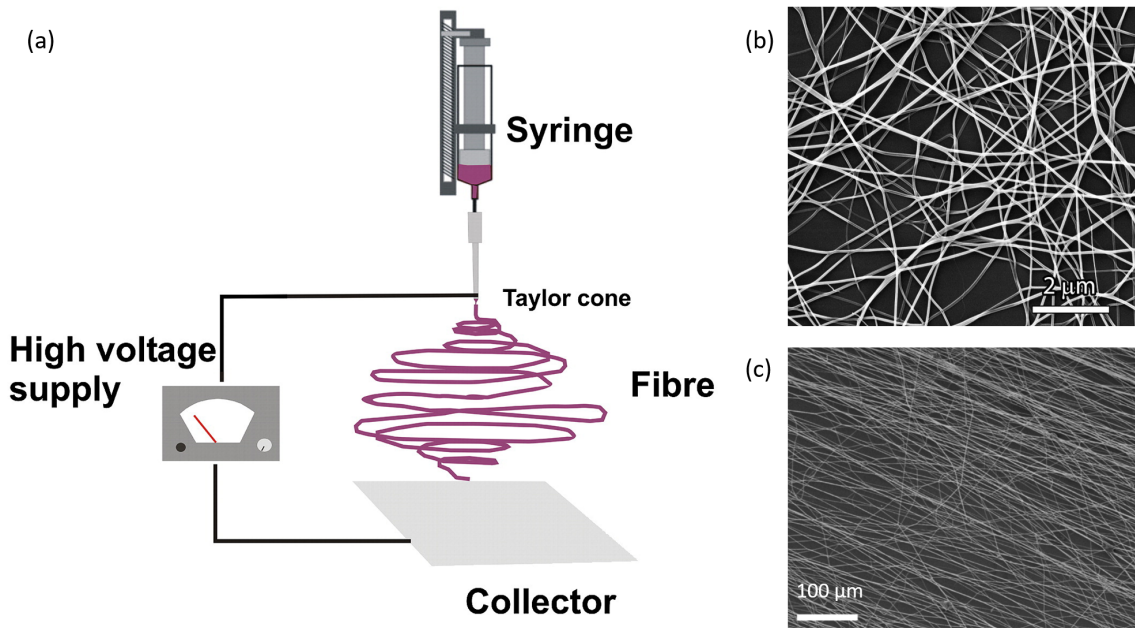
Figure 2.7 – (a) Schematic drawing of the electrospinning set-up. (b) SEM images of WO_3 [52] and (c) SnO_2 nanofibers [51] deposited by this technique.

by lift-off or etching techniques. The resolution of the technique is defined by the electron beam spot size and as higher energy is applied (in the range between 1 to 1200 keV), smaller minimum features are reached (sub-100 nm). The group of P. Candeloro compared SnO_2 wires fabricated by high-resolution EBL with thin film SnO_2, showing an improved performance as a gas sensor [54].

Nevertheless, lithographic techniques are generally slow and require a complex and expensive equipment. By contrast, there exist other top-down techniques that are fast, inexpensive and automatable and that have been rarely used for gas sensing applications. Direct laser interference patterning (DLIP) [55] and femtosecond laser subwavelength patterning [56] use laser technology and both rely on very simple open-air approaches for surface nanostructuring. On the one hand, they present an important advantage for gas sensing applications since the nanostructures can be patterned directly on the sensing device (in-situ), without the need to transfer them, as it is the case of most bottom-up techniques (ex-situ). On the other hand, both techniques present fast sensor processing, which is not the case usually of lithographic top-down techniques, such as EBL, IBL or SPL.

2.3.1   Direct laser interference patterning

DLIP is a non-contact technique that uses the interference patterns generated by two or more coherent laser beams to directly structure different materials. A beam splitter divides the laser source into several beams and then, thanks to mirrors, the beams are addressed right on the surface of the sample. An example of the two-beam configuration is shown in Fig. 2.8 and more beams configurations can be found in the work performed

by A. Lasagni [57] and A. Rodriguez [58].
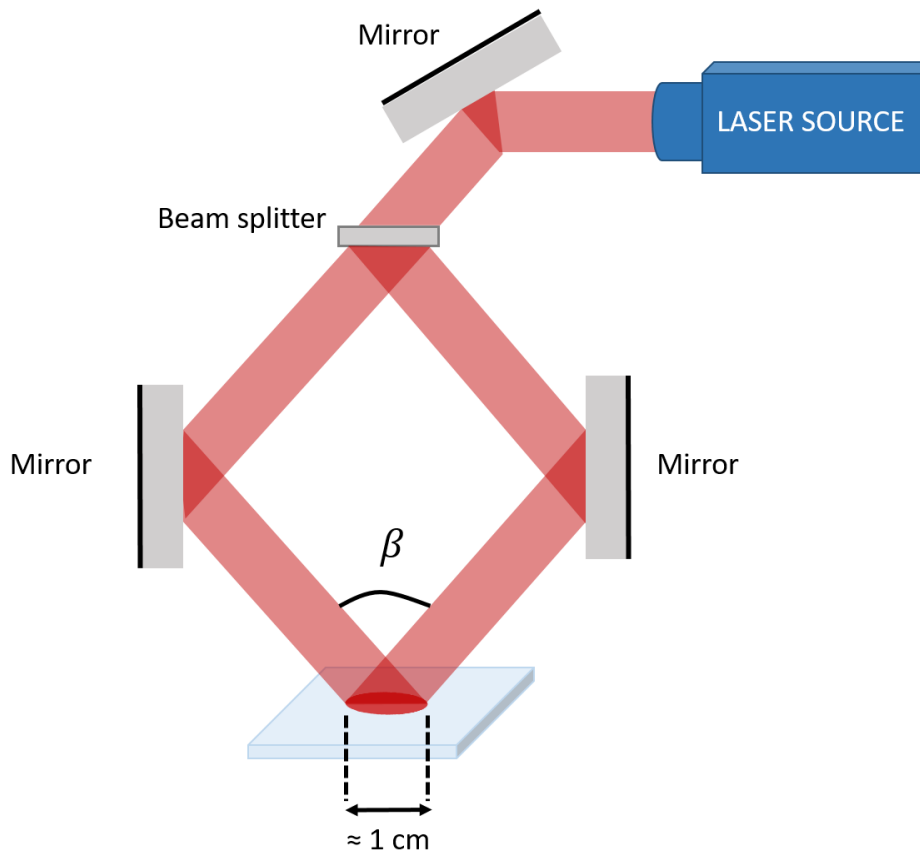
Figure 2.8 – Schematic set-up of DLIP for two-beam configuration.

The interference patterns are distributions of maximum and minimum intensity peaks that lead to nanostructures down to a fraction of the laser wavelength. The resolution of the features depend on the wavelength of the laser source and on the refractive index of the medium. The areas of the material exposed to higher intensities than its ablation or annealing threshold are morphologically and structurally modified, getting melted or even removed, while areas exposed to lower intensities than these thresholds remain unaffected.

LIL technique is based on the same principle but using a photoresist sensitive to electromagnetic waves, where the pattern will be processed. The structure will be revealed on the resist and transferred into the material by for example reactive etching [59], non-reactive etching [60] or wet etching [61]. The main advantage of DLIP is its fast velocity: in less than a second, it is able to nanostructure about 1 cm^2 (depending on the laser spot size) without the need of a mask. Besides, DLIP is compatible with industrial processes as it is explained in [58].

Depending on the number of beams, the fluence (energy per surface area) of each beam, the angle between them, the number of shots and the laser characteristics, the interference patterns are modified and can be tuned for specific applications. In Fig. 2.9 different number of beams configurations are shown. When two beams are used (Fig. 2.9 (a)), a series of minimum and maximum are obtained with a sinusoidal form, generating one-

dimensional (1D) periodic intensity distribution. Instead, for the three beam-configuration, different two-dimensional (2D) interference patterns can be obtained, as the one shown in the simulation of Fig. 2.9 (b).

(a) Two-beam configuration

(b) Three-beam configuration

1D interference pattern

2D interference pattern
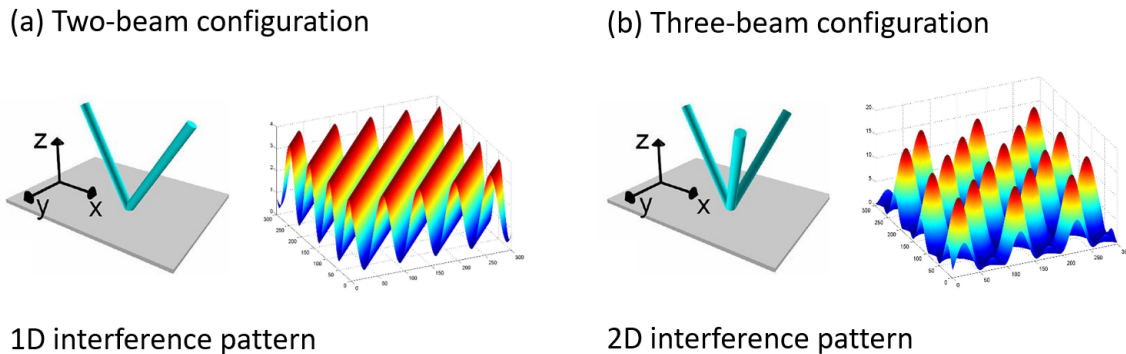
Figure 2.9 – (a) DLIP two-beam configuration and a simulated interference pattern generated by two beams and (b) DLIP three-beam configuration and a simulated interference pattern generated by three beams.

The period (P) of the different patterns is ruled by the following equations [62]:

$$P = \frac{\lambda}{2nsin\frac{\beta}{2}} \qquad \text{Two-beam configuration} \qquad (2.1)$$

$$P = \frac{\lambda}{\sqrt{3}nsin\frac{\beta}{2}} \qquad \text{Three-beam configuration} \qquad (2.2)$$

where λ is the laser wavelength, n is the diffraction index of the medium (air in most of the cases), and $\beta/2$ is the angle between one of the beams and the axis between the beams. Consequently, increasing the angle between the beams and the axis, the period of the patterns can be decreased, as it is shown in Fig. 2.10.

DLIP technique has been used in transparent conductive oxides (TCO) [63], metals [64] and polymers [65] (see Fig. 2.11 (a)), enhancing their properties for specific applications like doped ZnO for solar cells [66, 67], carbon films for tribological applications [68] and graphene oxide for humidity and NO_2 sensors [69, 70] (see Fig. 2.11 (b)). Nevertheless, it has not been used on the sensing field to modify the surface properties of MOX semiconductors and enhance their sensitivity to specific gases.

2.3.2   Femtosecond laser subwavelength patterning

In 1965, laser-induced periodic structures (LIPSS) in Ge were discovered by Birnbaum [71] and since then, the research community has been trying to understand their origin and generation mechanism [72]. LIPSS or ripples are (quasi-) periodic line structures with a period strongly related to the irradiation wavelength. They occur when
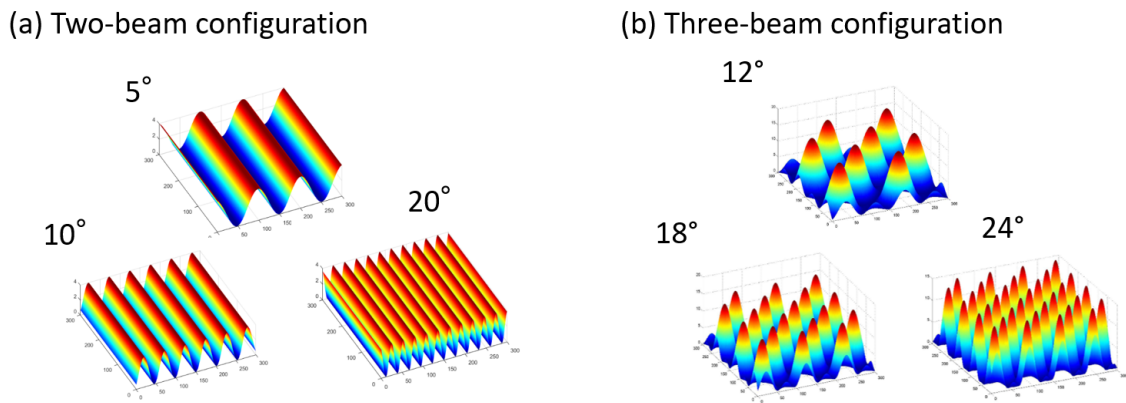
Figure 2.10 – Simulations of intensity distribution for (a) two-beam and (b) three-beam configuration DLIP for different angles.
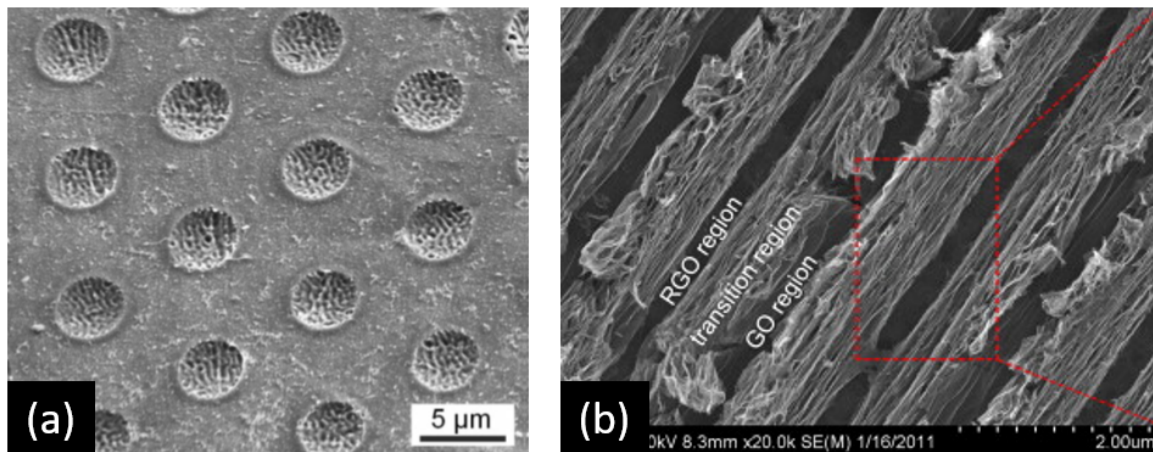
Figure 2.11 – (a) SEM images of a polymer DLIP-processed by a three-beam configuration with a period of 7.2 μm and (b) reduced graphene oxide hierarchical nanostructures DLIP-processed by a two-beam configuration with a period of 2 μm. Adapted from [65] and [69].

linearly polarized radiation interacts with a solid (metal, semiconductor or dielectric). LIPSS can be generated by different types of laser sources, from continuous wave irradiation [73] down to pulses in the femtosecond range [74].

In this thesis, LIPSS will be generated by a femtosecond laser and in Fig. 2.12, a layout of the typical femtosecond laser subwavelength patterning processing LIPSS on a sample is presented. The main difference with the DLIP technique is the processing area, while in DLIP one shot is enough to process around 1 cm^2, to be able to generate LIPSS the laser needs to be focused and as a consequence only few μm^2 are processed. For this reason, to process a reasonable area with LIPSS, the laser has to scan the surface of the material as it is shown in Fig. 2.12. Nevertheless, scanning speed can be greatly increased by using high repetition rate lasers. A scanning velocity of 10 μm/s with a standard Ti:Sapphire laser at a 1 kHz repetition rate could generate LIPSS on thin film ZnO (as shown in this thesis), but the velocity could be increased to 5 mm/s for a Ytterbium fiber laser with a repetition rate of 500 kHz.
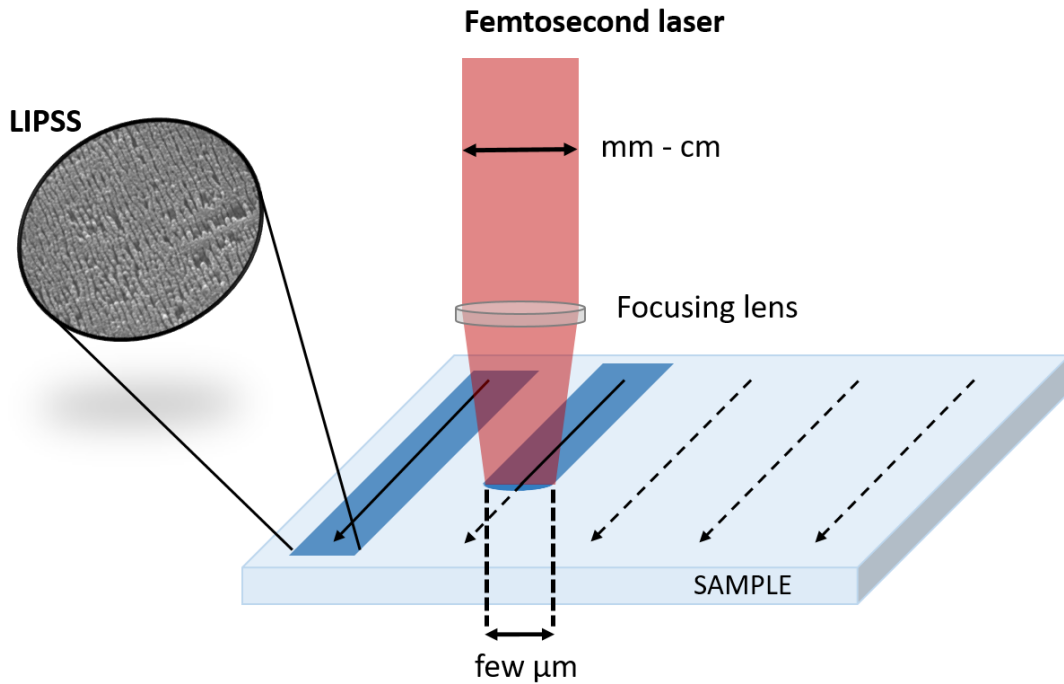
Figure 2.12 – Schematic set-up of femtosecond laser subwavelength patterning processing LIPSS. Continuous arrows represent processed area with LIPSS and discontinuous arrows represent the future scanned areas.

There are two different types of LIPSS nanostructures depending on the laser properties as well as on the characteristics of the material that is being processed. Low spatial frequency LIPSS (LSFL) (see Fig. 2.13 (a)) are generated on strongly absorbing materials usually with an orientation perpendicular to the beam polarization and a period slightly smaller than the beam laser wavelength. It is widely accepted that the generation of LSLF comes from the interaction of the irradiation laser beam with an electromagnetic wave scattered at the rough surface, although it may involve the excitation of surface plasmon polaritons (SPP) [75].

High spatial frequency LIPSS (HSFL) (see Fig. 2.13 (b)) present periods smaller than half of the irradiation laser wavelength and are generated commonly for femtosecond or picosecond pulse duration. Their formation mechanism is nowadays controversially discussed. Several theories have been proposed based on e.g.: self-organization [77], second harmonic generation [78] or different plasmonic effects [79].

Even though the fundamental aspects of the LIPSS formation are challenging nowadays, their interest relies in their simple approach. The nanostructures can be fabricates in a single step able to control mechanical or chemical surface properties. Consequently, LIPSS structures have been widely used in many kinds of applications: controlling cell growth direction [80], modifying the hydrophobic/hydrophilic properties of materials [81] or using the fact that the LIPSS act as diffractive gratings, generating structural color [82]. Nevertheless, to the best of our knowledge, LIPSS have never been studied for gas sensing applications. Due to the changes on the surface structure, defects could be introduced, what could enhance the sensitivity for specific gases.
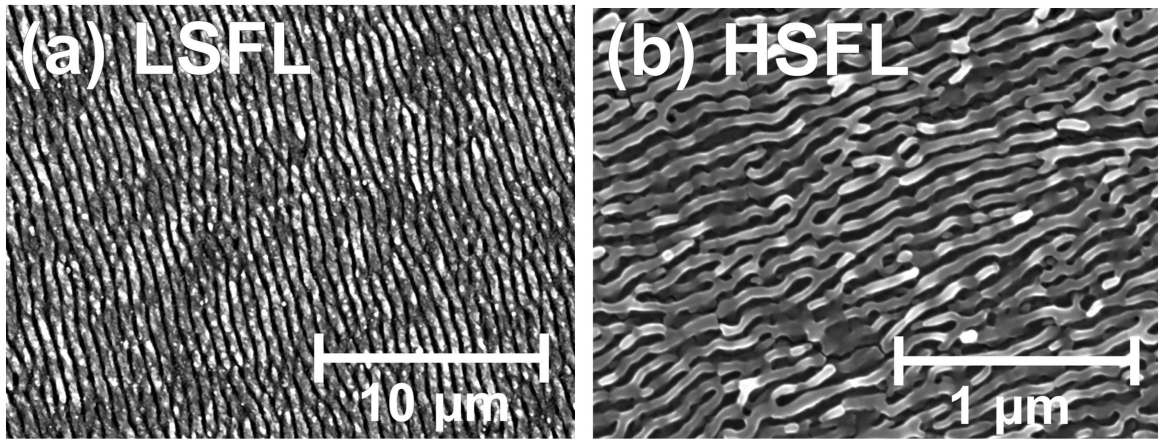
Figure 2.13 – (a) SEM images of LSFL LIPSS and (b) HSFL LIPSS formed on titanium alloy (Ti6A14V) surfaces after irradiation with femtosecond laser pulses (30 fs, 800 nm, 1 kHz). Adapted from [76].

2.4   Basics of chemoresistive gas sensors

The detection mechanism whereby the sensor senses the gas molecule is based on the changes of the electronic properties of the semiconductor due to gas adsorption, the influence of the microstructure and the consumption of the target gas in the film.

Quantum mechanics establishes that the energy of electrons can only take on certain discrete values. When atoms are arranged in a perfect crystal, some of the allowed energy levels are so close to each other that they can be considered bands of energy [1].

In the specific case of semiconductors, detailed energy bands are very complex, depending on the crystal structure. Nevertheless, they can usually be simplified, since the electronic properties mainly depend on two different bands: valance band (VB) and conduction band (CB); separated by a forbidden energy region called band gap, as shown in 2.14 (right).

In a theoretical perfect crystal, at zero temperature, the VB should be completely filled with electrons and the CB completely empty. However, crystals always present impurities and defects, therefore there are missing electrons in the VB that are present in the CB.

The electrons energy distribution at thermal equilibrium is described by the Fermi function (Fig. 2.14 (left)):

$$f = \frac{1}{1 + e^{\frac{(E - E_F)}{kT}}} \tag{2.3}$$

where k is the Boltzmann constant and T is the absolute temperature. The Fermi energy E_F is the energy level that has $1/2$ of possibilities to be occupied by electrons. Depending on the position of the E_F, different semiconductors can be considered:

- **Intrinsic semiconductor:** the Fermi energy is located very close to the center of the band gap, therefore, in the CB there are almost the same number of carriers as
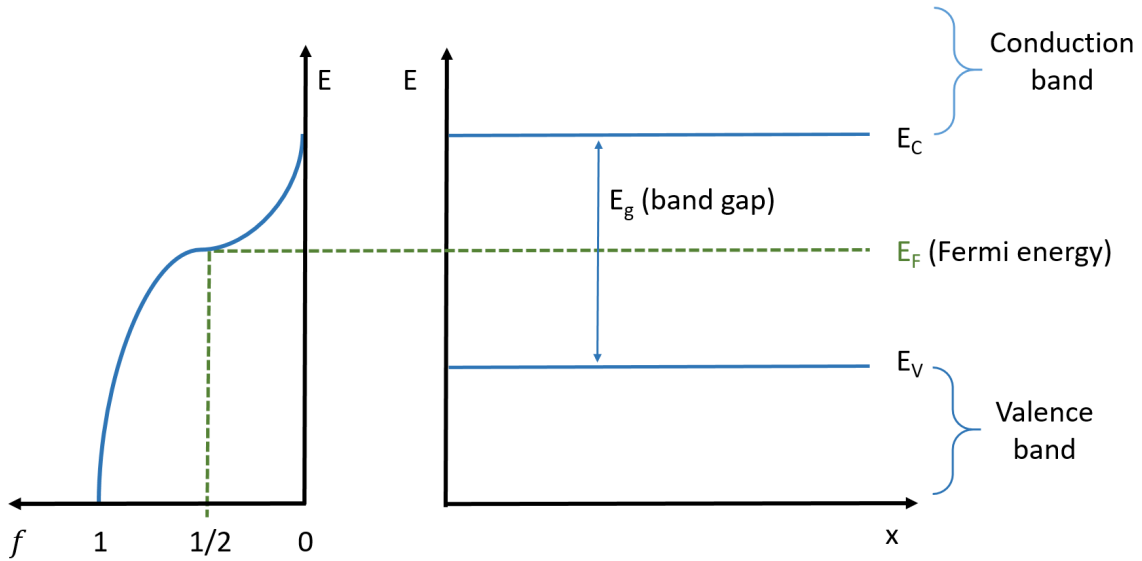
Figure 2.14 – Left: Fermi function as a function of the energy. Right: band diagram for an intrinsic semiconductor (energy (E) as a function of the distance to the surface of the semiconductor (x)).

in the VB.

- **Extrinsic semiconductor:** imperfections such as vacancies or interstitial atoms are introduced in a crystal and dominate the electrical properties. Consequently, the E_F is shifted closer to the VB or CB.

  (i) n-type semiconductor: donor impurities are dominating in the crystal, E_F is close to the CB and the majority charge carriers are electrons (Fig. 2.14).

  (ii) p-type semiconductor: acceptor impurities are dominating in the crystal, E_F is close to the VB and the majority charge carriers are holes.

Most of the semiconductors used for chemical sensing are n-type, as in the case of ZnO and WO_3 [83, 84], although an effort has also been performed to study p-type materials, such as NiO [27].

2.4.1   Surface states, depletion layer and Poisson equation

The surface of a crystal breaks the periodicity of the lattice structure, leading to a rearrangement of the atoms at the surface and increasing their reactivity. Consequently, localized energy states (surface states) are formed, usually inside the band gap region. These energy states can capture or give up electrons (acting as acceptors or donors). For the case of highly ionic semiconductors, as most metal oxides, it is accepted that surface oxygen ions act as a donors, giving up electrons and surface metal ions (such as Zn^{2+} for the case of ZnO) act as acceptors, capturing electrons (Fig. 2.15 (a)).
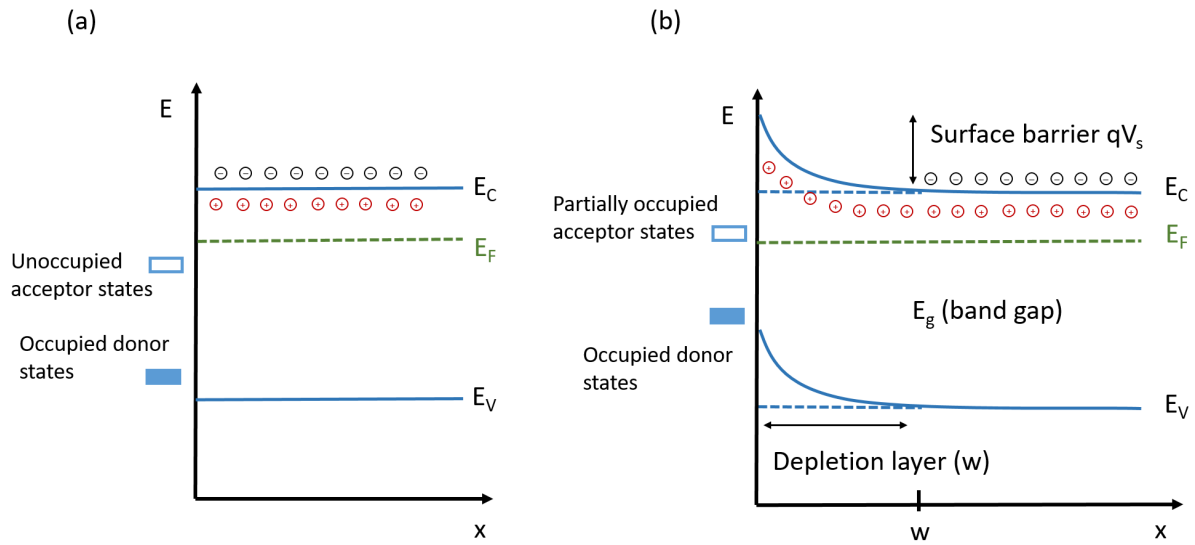
Figure 2.15 – Band diagram of an n-type semiconductor (a) including a surface with neutral surface states (flat-band) and (b) with depletion layer.

The situation shown in Fig. 2.15 (a) is far from equilibrium and surface states cause an exchange of electrons inside the crystal structure, thus generating a depletion layer close to the surface Fig. 2.15 (b). The depletion layer is where electrons coming from the CB are captured by the surface states. In order to balance the negatively charged surface, there are positively charged donors near the surface.

To estimate the width of the depletion layer or space charge region (w) and the curvature of the energy band, the Poisson equation is used:

$$\frac{d^2V}{dx^2} = \frac{qN_i(x-w)}{\varepsilon\varepsilon_0} \tag{2.4}$$

where V is defined as the difference between the bulk potential of the semiconductor (ϕ_b) and the potential of the semiconductor depending on the distance from the surface x ($\phi(x)$). N_i is the ion density in the space charge layer, q is the electron charge, ε is the dielectric constant of the semiconductor and ε_0 is the dielectric constant in vacuum.

To integrate the Poisson equation the boundary conditions 2.5 and 2.6 have been used, indicating that the semiconductor is uncharged for $x \geq w$ and defining $V = 0$ when $x = w$.

$$\frac{dV(x=w)}{dx} = 0 \tag{2.5}$$

$$V(x=w) = 0 \tag{2.6}$$

As a result, the electrical potential can be obtained as a function of the distance to

the surface of the material:

$$V = \frac{qN_i(x-w)^2}{2\varepsilon\varepsilon_0} \tag{2.7}$$

For $x = 0$, the Schottky relation can be obtained, indicating that the energy qV_s, where V_s is the surface barrier, is the energy that electrons have to overcome to move to surface states.

$$V(x=0) = V_s = \frac{qN_iw^2}{2\varepsilon\varepsilon_0} \tag{2.8}$$

For n-type materials N$_i w$ is the number of electrons per unit area extracted from the space charge region that should be equal to the number of electrons per unit area moved to the surface, therefore N$_i w$ = N$_s$, where N$_s$ is the density of charge surface states. Finally, the potential difference between the surface and the bulk can be obtained as a function of the amount of charge N$_s$ on the surface, independently of the surface charge region width:

$$V_s = \frac{qN_s^2}{2\varepsilon\varepsilon_0 N_i} \tag{2.9}$$

It is important to notice that the performed derivation has taken into account surface states coming from the surface without adsorbed species. Nevertheless, the same considerations could be done for surface states generated by adsorbed oxygen species.

2.4.2 Solid/gas interface

In order to understand what is happening when a chemoresistive MOX detects gas, adsorption process at the surface of the semiconductor is crucial. The adsorption species will control the density of charge surface states and the conductivity will be modified. There are two main adsorption mechanisms involved on gas detection: physisorption and chemisorption [85].

Physisorption: is the weak adsorption process, where the solid-gas interaction is produced by Van der Waals forces. The electronic structure of the atoms is barely altered and in principle, the atoms do not move from their lattice position. Temperatures where usually physisorption is produced are below 300 K.

Chemisorption: is a strong chemical bonding, where the electronic structure of the solid is strongly perturbed. Chemisorption requires higher temperatures, between 300 K and 600 K.

The density of physisorbed species will represent the density of empty surface states, but once the electrons are captured by the physisorbed surface states, they will be transformed into chemisorbed surface states [86]. The ionosorption (chemisorption of ions) will be the most important adsorption process for gas sensors, particularly the ionosorption of oxygen species. As chemical sensors work in air conditions, oxygen species will be strongly adsorbed at the surface of the semiconductor and contribute to the negative charge of surface states, providing the surface charge qN$_s$.

Oxygen can dissociate in several forms for temperatures between 100 °C and 500 °C: O_2^- (in molecular form) and O^- or O^{2-} (in atomic form). It is proved that for temperatures lower than 150 °C-200 °C, the molecule form dominates, while O^- expected to be stable between 100 °C and 300 °C and O^{2-} above 300 °C [87]. It is accepted that oxygen species will be adsorbed following the next reactions [88]:

$$O_{2(g)} \Longleftrightarrow O_{2(ads)} \tag{2.10}$$

$$O_{2(ads)} + e^- \Longleftrightarrow O_{2(ads)}^- \tag{2.11}$$

$$O_{2(ads)}^- + e^- \Longleftrightarrow 2O_{(ads)}^- \tag{2.12}$$

$$O_{(ads)}^- + e^- \Longleftrightarrow O_{(ads)}^{2-} \tag{2.13}$$

The oxygen species chemisorbed at the surface of the grains capture electrons from the material and generate negative surface charges that will be compensated by space charge near the surface, resulting in a depletion layer as is it shown in Fig. 2.16. Therefore, conductivity will be dominated by the electrons with energy enough to overcome the Schottky barrier qV_s and flow from one grain to another.

In n-type semiconductors, the chemisorption of an acceptor like oxygen species will produce an electron transfer from the semiconductor to the oxygen, leading to a decrease in conductivity. When a different gas is introduced in the atmosphere, the concentration of oxygen in the air will vary and the gas molecules will be able to interact with the adsorbed oxygen species or directly with the semiconductor surface leading to a change in the conductivity.

2.4.3   Conduction mechanism of semiconductor films

Thick films are considered porous materials and in principle, gas molecules can interact inside the volume of the layer, increasing substantially the active surface. Different conducting models have been developed depending on the porosity of the layer. As a function of the overlapping between different depletion layers of neighbouring grains, three different situations can be described: open neck (depleted regions are formed on both sides of the grain junction), close neck (depleted regions of both grains are superposed) and double Schottky barrier (at the point of contact between grains a Shottky barrier is formed) [24].

Instead, thin films are compact layers, where the interaction with the gas mainly takes place at the surface of the semiconductor itself. In polycrystalline thin films, grain boundaries contain a great number of surface states, generating depletion layers on the energy bands. Therefore, the total conductivity of a semiconductor is based on grain boundaries and therefore on the morphology. Depending on parameters such as the den-
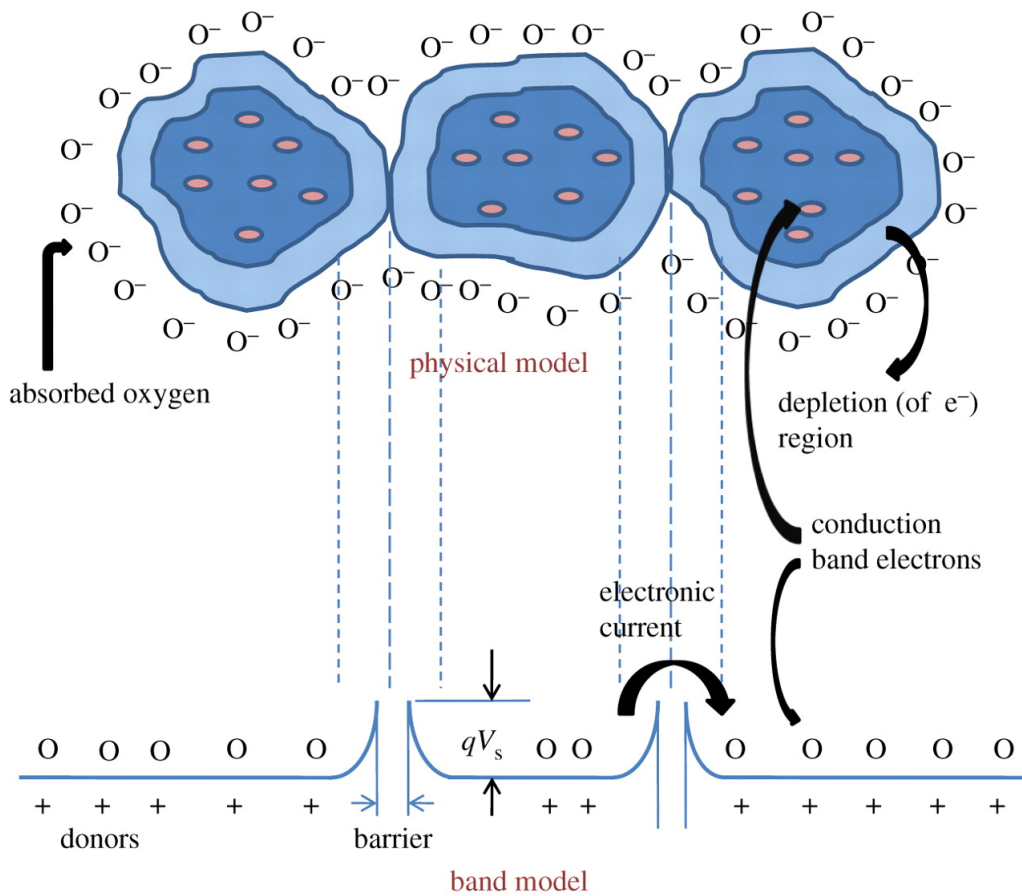
Figure 2.16 – Band model (bottom) and physical model (top) of three consecutive grains when oxygen ions are chemisorbed [89].

sity of surface states (n_t), concentration of free electrons in the bulk (N_0), grain size (L_c) and Debye length (L_D)[1], three different situations can be found [24]:

(i) When $n_t \leq N_0 L_c$, the depletion layer occurs to be very thin, because the charge carriers in the surface charge region are less than the bulk carriers. Therefore, there exist less active sites for oxygen adsorption and the height of the potential barrier is almost constant with the variation of the atmosphere. In Fig. 2.17, the band model and the physical model of this situation is shown.

(ii) When $n_t \simeq N_0 L_c$ and $L_D < L_c/2$, the number of charge carriers in the surface charge region is comparable with that in the bulk and the Debye length is smaller than the grain radius. The band diagram in this case is shown in Fig. 2.18, where grains are partially depleted and the mobility of the electrons limited by the barrier.

In this case, there exists a greater carrier depletion in the presence of air, so when reducing agents are present in the atmosphere an oxidation reaction takes place and electrons are released towards the volume of the grain. Consequently, the potential barrier height decreases or disappears.

---

[1]Debye length is defined as: $L_D = \sqrt{\dfrac{\varepsilon kT}{N_0 q^2}}$.
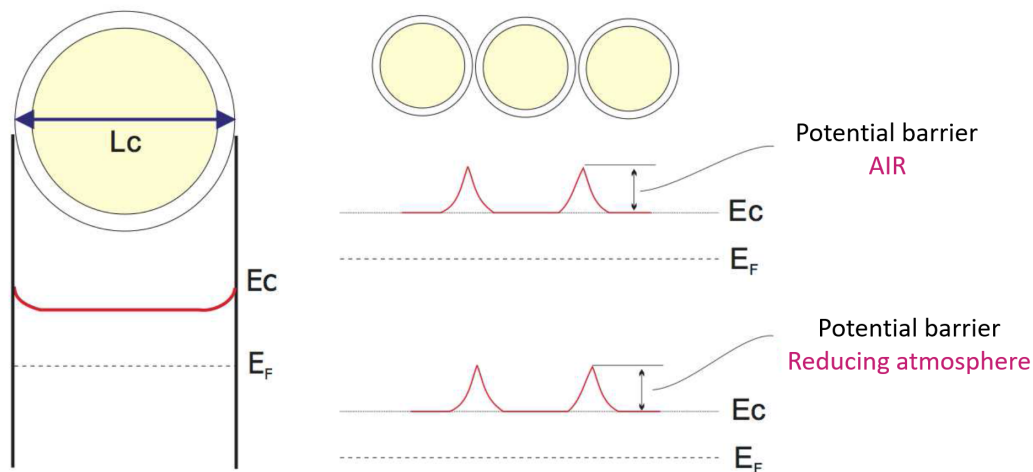
Figure 2.17 – Characteristic band model and grain boundary behaviour when $n_t \leq N_0 L_c$.
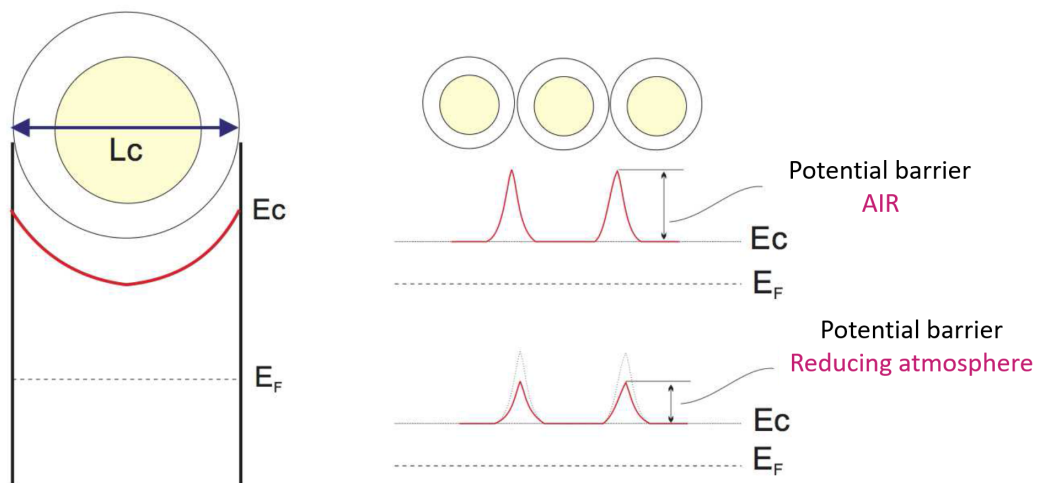
Figure 2.18 – Characteristic band model and grain boundary behaviour when $n_t \simeq N_0 L_c$ and $L_D < L_c/2$.

(iii) When $n_t \simeq N_0 L_c$ and $L_D > L_c/2$, the number of charge carriers in the surface charge region are also in the same order of magnitude as in the bulk, but in this case the Debye length is greater than the grain radius. This leads to quasi-fully depleted grains, where there is no barrier for the electrons to flow.

As shown in Fig. 2.19, when a reducing atmosphere exists the potential barrier decreases in the entire grain and not only between the grains, as in the previous case. This leads to a conductivity independent of the grain boundary potential but limited by the grain size.
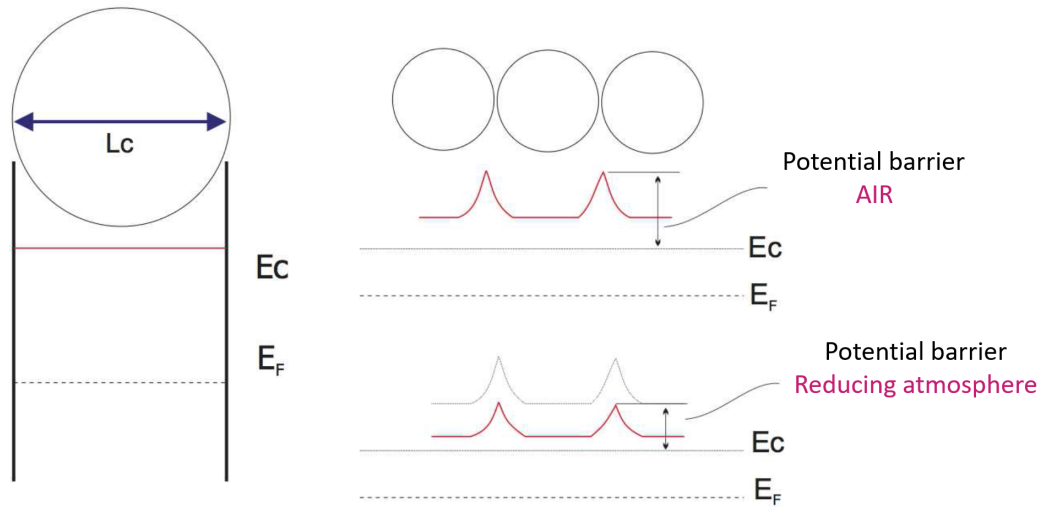
Figure 2.19 – Characteristic band model and grain boundary behaviour when $n_t \simeq N_0 L_c$ and $L_D > L_c/2$.

2.5 ZnO and WO$_3$ for gas detection

As it has been mentioned, different type of MOX semiconductors have been tested for gas sensing applications: from the typical SnO$_2$, to MOX that have been rarely used for gas detection, such as cobalt oxide (Co$_3$O$_4$) [90] or vanadium oxide (V$_2$O$_5$) [91]. Nevertheless, as the objective in this thesis is to study the effects of the different laser treatments into materials used for gas sensing applications, two already well studied materials have been chosen for this purpose: ZnO and WO$_3$.

2.5.1 Material properties

ZnO

ZnO has been selected as one of the target materials because it has been well studied since 1935 [92] and it presents attractive features for device fabrication such a non-toxicity and low cost. It has been used in different applications, from medical devices [93] to solar cells [94] and has also a long trajectory as a sensing material in chemoresistive gas sensors, both activated by temperature [95] and electromagnetic waves [96, 97]. Besides, it has been demonstrated its good selectivity to NO$_2$ [98–100].

ZnO presents a direct wide band gap (3.37 eV) at room temperature [101]. From the crystallographic point of view, it can be grown in many different structural forms, but wurtzite (hexagonal) structure is the thermodynamically preferred form in ambient conditions (Fig. 2.20) [102]. The hexagonal unit cell presents lattice constant parameters a = 0.325 nm and c = 0.52066 nm. As shown in Fig. 2.20, the zinc (Zn) atoms are surrounded by oxygen atoms in a nearly tetrahedral configuration [103].

Defects present an important issue concerning ZnO conductivity and therefore regarding gas sensitivity [104], especially oxygen vacancies defects [105]. Besides, grain size
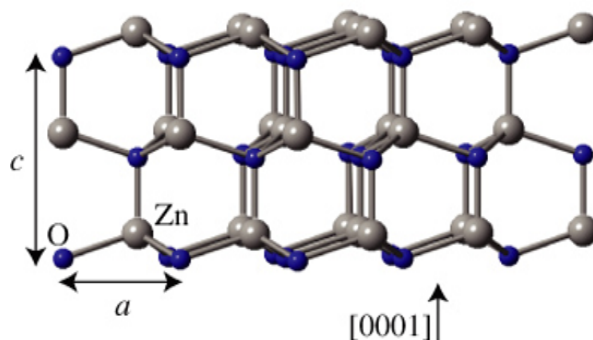
Figure 2.20 – ZnO wurtzite structure [101].

and morphology also play an important role [106].

WO$_3$

WO$_3$ is a transition metal oxide that presents interesting electrochromic [107], thermochromic [108] and gasochromic [109] properties so it has been used in different applications such as solar cells [110] and gas sensors [111].

Bulk WO$_3$ presents a band gap between 2.6 eV and 3.25 eV depending on the crystal phase [111]. Many polymorphic structures have been identified in WO$_3$ as a function of the temperature [112–116], as shown in Fig. 2.21, what strongly affects its electrochromic characteristics. Not all the transitions are reversible and the lattice constants of each crystal structure can be found in [111].
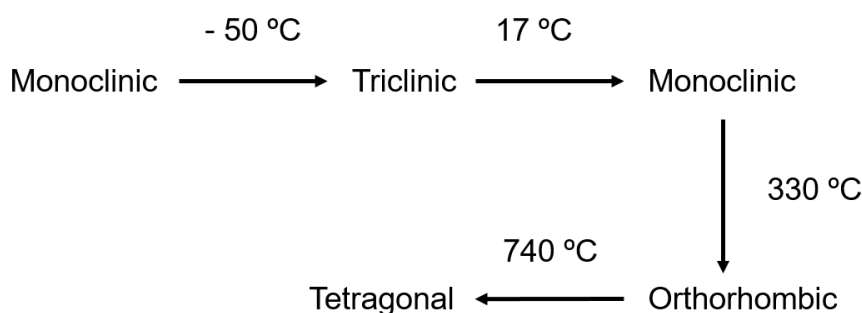
Figure 2.21 – Crystal structure transitions of WO$_3$ as a function of temperature.

In addition, the sensing performance is expected to be affected by the crystal structure as shown by I. M. Szilàgyi, who found that monoclinic WO$_3$ shows good selectivity to H$_2$S, while hexagonal WO$_3$ sensors present lower sensitivity but much faster response [117].

2.5.2 NO$_2$ detection mechanism

NO$_2$ is a reddish brown molecule at ambient temperatures with an irritating odour. It is one of the most harmful air pollutants because it can cause eye irritation and se-

vere respiratory effects on human health [118, 119]. Outdoor sources are mainly coming from automotive emissions, but furthermore, NO_2 is an intermediate in the industrial synthesis of nitric acid (used in fertilizers production), and it is present in the acid rain. Home sources are gas-fueled heating and gas-fueled stoves and therefore winter indoor values of NO_2 can be twice the outdoor levels. Different acceptable levels of exposure have been introduced depending on the governmental agencies and private organizations. In particular, in Europe, the recommendation from the Scientific Committee on Occupational Exposure Limits (SCOEL) for Nitrogen Dioxide of the European Commission are summarized in Table 2.2 [120]. As the document states, the recommendation is based on compilations by WHO[2] (1997), DECOS[3] (2004), US EPA[4] (2008), DFG[5] (2005 and 2010), ACGIH[6] (2012) and National Research Council of the National Academies (2012). Therefore, the emission control of NO_2 is crucial to reduce its dangerous effects on environment and human beings.

Description	NO_2 concentration
8-hour TWA[a]	0.5 ppm
STEL[b] (15-min)	1 ppm

Table 2.2 – NO_2 exposure limits

[a]TWA is the employee's average airborne exposure in any 8-hour work shift of a 40-hour work week which shall not be exceeded.

[b]Short Term Exposure Level.

The main difference between the detection of reducing and oxidizing gases is that while reducing molecules (such as CO) react with the adsorbed oxygen species; oxidizing molecules (such as NO_2) mainly adsorb directly into the semiconductor surface, competing for adsorbing sites with the oxygen [11].

Deep studies related to NO_2 detection mechanism are mainly based on SnO_2 [88, 121, 122], since it is the most characterized material for gas sensors. Despite that, some investigations are also focused on ZnO [123–125] and WO_3 [126–128].

It is generally accepted that, for low temperatures, NO_2 undergoes adsorption as the reaction 2.14 states [88, 123, 126]. In the absence of oxygen, NO_2 adsorption could be treated the same way as oxygen adsorption, but in air conditions, oxygen and NO_2 molecules compete for the electrons from the CB [129]. When a NO_2 molecule is adsorbed on the semiconductor surface, the depletion layer width increases and so does the potential barrier height. The adsorbed molecules will trap electrons from the CB of the semiconductor, thus leading to a decrease of the conductivity.

$$NO_2 + e^- \Longrightarrow NO_{2(ads)}^- \tag{2.14}$$
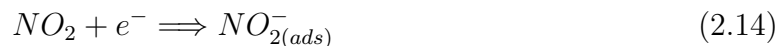
[2]World Health Organization.

[3]Dutch Expert Committee on Occupational Standards.

[4]United States Environmental Protection Agency.

[5]German Research Foundation.

[6]Association Advancing Occupational and Environmental Health.

Reactions 2.15 and 2.16 are also reported in some articles as a part of the NO$_2$ detection mechanism. The first one is expected for higher temperatures (> 250 °C) [88, 123, 126] and the second one represents the NO$_2$ adsorbed interaction with oxygen species, generating doubly charged oxygen adsorption and NO molecules [49, 130].

$$NO_2 + e^- \implies NO_{(g)} + O_{(ads)}^- \tag{2.15}$$

$$NO_{2(ads)}^- + O_{(ads)}^- + 2e^- \implies NO_{(g)} + 2O_{(ads)}^{2-} \tag{2.16}$$
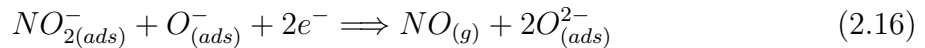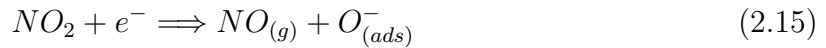
Regarding the NO$_2$ detection mechanism for ZnO, defects seem to play an important role. In ZnO nanoparticles, defects detected by photoluminescence (PL) have been identified to contribute to the NO$_2$ detection mechanism [131]. More specifically, some groups also reported PL analysis to show the importance of the oxygen vacancies in ZnO nanowires [132]. Density functional theory (DFT) studies have demonstrated that NO$_2$ molecules present three more times adsorption energy on vacancy sites than in perfect sites [133]. Other group highlighted the effect of donor defects as well as surface oxygen species (O_2^- and O^{2-}) [42, 125] through in-situ diffuse reflectance infrared fourier transform spectroscopy (DRIFTS) technique.

In table 2.3, a summary of different sensors based on ZnO sensing NO$_2$ under thermal excitation or at room temperature are presented. The crystal structure in all the references presented is hexagonal ZnO. Among them, nanowires grown by thermal oxidation exhibit a good performance at 200 °C showing high reproducibility and stability, important features for large-scale production [134].

Since WO$_3$ is a n-type semiconductor like ZnO, comparable results regarding NO$_2$ detection have been found in the bibliography. In [127], DFT studies have been performed to study the NO$_2$ adsorption in different vacancy positions with oxygen deficient WO$_3$ nanowires, indicating that oxygen vacancies benefit the adsorption of NO$_2$ molecules. They concluded that the sensitivity of WO$_3$ nanowires could be significantly enhanced by introducing oxygen vacancies. Besides, grain size dependence has also been studied for WO$_3$ based sensors under NO$_2$ atmospheres [141]. For concentrations of NO$_2$ between 10 and 20 ppm, responses are independent of grain diameter, for diameters higher than the double of the space charge layer thickness. By contrast, for smaller grain diameters, responses increase abruptly with the decrease of the grain size.

In table 2.4, a review of updated results comparing different WO$_3$ based sensors under NO$_2$ atmospheres are shown. As can be seen, different crystal structures have been studied, although monoclinic structure prevails among the others. It is worth mentioning that relatively low temperatures (75 °C < T < 200 °C) are used as an optimal temperature for NO$_2$ detection in WO$_3$ based sensors, as it is also the case in this thesis. Among the reviewed studies, monoclinic WO$_3$ nanofibers fabricated by electrospinning are sensitive at 75 °C to only 0.4 ppm of NO$_2$, although long recovery times are shown [52]. Besides, tripled-shell yolk-shell spheres prepared by ultrasonic spray pyrolysis [142] presented high sensitivities to very low concentrations of NO$_2$. These results were attributed to the high accessibility of the yolk-shell morphology to the target gas. Nevertheless, it is commonly agreed that a drawback of drop casting techniques is their low reproducibility.

Nanostructure	Method	Anneal. (°C)	$T_{opt.}$ (°C)[a]	Conc.	$\dfrac{R_g}{R_{air}}$[b]	Ref.
Nanoneedles	Liquid-solid	650	195	1 ppm	0.37	[98]
Nanostructures	Hydrothermal	200	200	1 ppm	3.57	[135]
Nanostructured thin film	SILAR[c]	300	150	10 ppm	2.4	[136]
Hierarchical	MES-CHSM[d]	200	200	1 ppm	~ 3.5	[137]
Nanofibers	Electrospinning	400	350	1 ppm	~ 1.04	[123]
Nanoparticles	SNAS method[e]	400	290	40 ppm	220	[131]
Nanowires	Thermal oxidation	400	200	1 ppm	~ 10.5	[134]
Nanorods with nanovoids	Hydrothermal	500	250	1 ppm	5.68	[138]
Branched nanowires	Thermal evaporation	950	300	5 ppm	2.06	[139]
Nanopyramids	Spin-coating	400	200	1.25 ppm	~ 3.33	[140]

Table 2.3 – Comparative results of devices based on ZnO sensing NO_2.

[a]Optimal temperature of the sensors.

[b]R_g is the resistance in NO_2 presence and R_{air} is the resistance in air.

[c]Successive ion layer adsorption and reaction.

[d]Mechano-electrospinning-assisted continuous hydrothermal synthesis method.

[e]Separate nucleation and aging steps.

Nanostructure	Method	Anneal. (°C)	Crystal structure	T$_{opt.}$ (°C)[a]	Conc.	$\frac{R_g}{R_{air}}$ [b]	Ref.
Nanoplates	Hydrothermal	100	Orthorhombic	100	1 ppm	~ 5	[50]
Tripled-shell yolk-shell spheres	Ultrasonic spray pyrolysis	900	Monoclinic	200	0.05 ppm	49	[142]
Villi-like nanostructures	RF sputtering with GAD mode[c]	550	Monoclinic	200	1 ppm	~ 145	[143]
Nanofibers	Electrospinning	450	Monoclinic	75	0.4 ppm	18.42	[52]
Hierarchical flower-like nanostructures	Hydrothermal + acid tratment	500	Monoclinic	90	0.08 ppm	~ 140	[144]
Coating	Atmospheric-plasma-spayed	700	Monoclinic	130	0.45 ppm	80	[126]
Noanorod assembled microspheres	Hydrothermal	350	Hexagonal	200	1 ppm	~ 29	[43]
Hierarchical dendrites	Solvothermal	500	Hexagonal	140	0.5 ppm	~ 4.25	[145]
Hierarchical carpet-like microflowers	Hydrothermal	350	Triclinic	200	1 ppm	~ 60	[146]
Microspheres	Hydrothermal	400	Hexagonal	100	1 ppm	7	[83]

Table 2.4 – Comparative results of devices based on WO$_3$ sensing NO$_2$.

[a]Optimal temperature of the sensors.
[b]R_g is the resistance in NO$_2$ presence and R_{air} is the resistance in air.
[c]Radio frequency sputtering with glancing angle deposition.

Chapter 3

ZnO based sensors nanostructured by direct laser interference patterning

A deep understanding of the morphological and structural material properties is needed in order to comprehend the behaviour of materials in sensing devices. Surface properties of the materials are especially relevant in gas conductometric sensors based on metal oxide thin films. For this reason, in the three following chapters, the influence of the laser techniques in the physical properties of the thin films has been researched, as well as their sensing characteristics.

In particular, in this chapter, ZnO based sensors on alumina substrate processed by a two-beam DLIP set-up are studied. On one hand, a simulation of the heat transfer equation of structures with 730 nm of period and two different fluences is carried out with the purpose of finding out the transient temperature as a function of depth inside the ZnO thin film during the laser exposure. On the other hand, the samples are fabricated and experimentally characterized in order to investigate the laser influence both on the thin film surface and in depth from the structural and composition point of view. This is relevant in order to study the interaction of the material at the thin film/substrate interface under the laser effect, what is crucial for materials undergoing laser processes on substrates sensitive to high temperatures. The gas sensing performance under NO_2 is also investigated and the sensing mechanism discussed. Moreover, ZnO based sensors annealed at three different temperatures (600 °C, 700 °C and 800 °C) are also fabricated and compared with the sensors processed by DLIP.

Nomenclature

$C_p(T)$	Heat capacity (J/(m·s))	***Greek symbols***
I	Intensity distribution of the laser (J/(m^2· s))	Λ — Duty cycle
$I_t(t)$	Temporal Gaussian distribution (s^{-1})	β — Angle between the interfering beams (°)
K	Thermal conductivity (W/(m · K))	$\Phi(x)$ — Energy intensity distribution (J/m^2)
P	Period of the interference pattern (m)	Φ_0 — Fluence of each interference beam (J/m^2)
$Q(x,z,t)$	Heat source (J/m^2)	α — Absorption coefficient (m^{-1})
R	Reflectivity	λ — Wavelength (m)
T	Temperature (K)	ρ — Density (kg/m^3)
T_{th}	Thermal annealing threshold temperature (K)	σ — Standard deviation (s)
$T_{trans.}$	Transmittance	τ_p — Full width at half maximum of the laser pulse (s)
$g(x,z,t)$	Heat flux (W/m^2)	
k	Wave number (m^{-1})	
m_x	Molar mass (kg/mol)	
t	Time (s)	
t_0	Pulse arrival time (s)	
x, y and z	Position coordinates (m)	

3.1 Experimental

3.1.1 Sensor fabrication

The fabrication steps of the ZnO sensing device are summarized in Fig. 3.1. The sensor was fabricated on a 1 x 2 cm^2 polished alumina substrate, where a Pt heater was patterned at the back side by photolithography followed by DC sputtering in an Edwards ESM 100 system (the thickness of the Pt thin film is 200 nm approximately). The lift-off process was carried out with acetone. 1 mm^2 of ZnO sensing layer was deposited on the top side of the alumina substrate by photolithography followed by RF sputtering in an argon (Ar) atmosphere (ZnO target 99.99 % purity) under $5 \cdot 10^3$ mbar of gas pressure in a Pfeiffer-Iontech system(Fig. 3.1 (c)). The ZnO sputtering time was 1 h, the deposition temperature was between 21 °C and 23 °C and as for the Pt, acetone was used for the lift-off process. Subsequently, some ZnO thin films were thermally stabilized in a quartz oven at different temperatures: 600 °C, 700 °C and 800 °C during 4 h in synthetic air in order to analyse the temperature annealing effect (the samples will be named TT600C, TT700C and TT800C, respectively. Fig. 3.1 (d$_1$)). Other samples were processed by two-beam DLIP set-up with a frequency tripled Q-switched Nd:YAG laser source provided by Thales, the Saga HP model (with a wavelength of 355 nm, a pulse duration of 8 ns, a maximum energy of 600 mJ per pulse and a flat-top energy distribution) to obtain 1D interference patterns on the surface (Fig. 3.1 (d$_2$)).
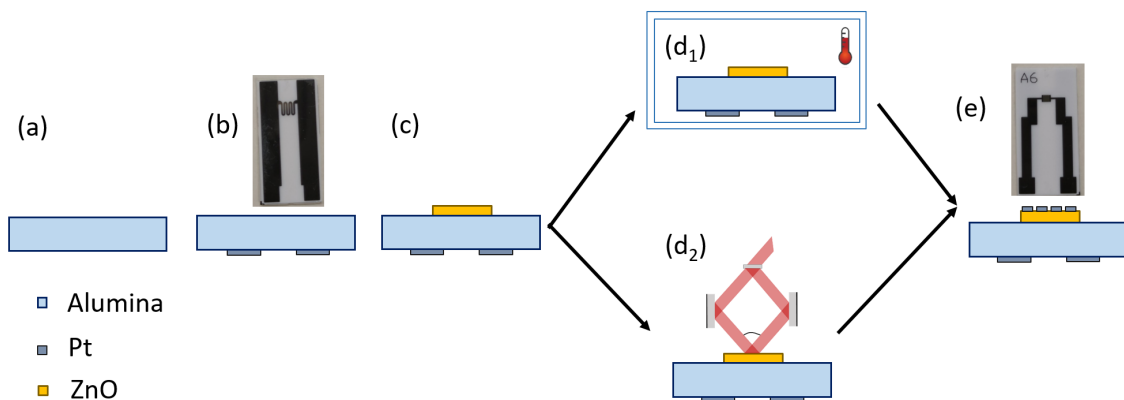
Figure 3.1 – Sensor fabrication steps: (a) polished alumina substrate, (b) DC sputtering Pt heater deposited on the back side of the alumina substrate, (c) RF sputtering of ZnO thin film layer deposited on top of the alumina, (d$_1$) thermal treatment, (d$_2$) DLIP process and (e) DC sputtering of Pt IDT electrodes deposited on top of the ZnO layer.

On the detailed DLIP set-up (Fig. 3.2 (a)), an optical beam splitter divides the laser source into two different beams, afterwards they are reflected in mirrors and finally addressed towards the sample surface with the same incident angle. An example of a typical energy distribution of two-beam configuration DLIP is also shown.

For the two-beam configuration DLIP, the period of the interference structure (P) is defined by the angle between the two laser beams (β) and the wavelength (λ), as it was shown in equation 2.1. In this case, the medium is air (n = 1) and in order to achieve lines with a theoretical period of 730 nm, an angle of 28.1 degrees was set-up.
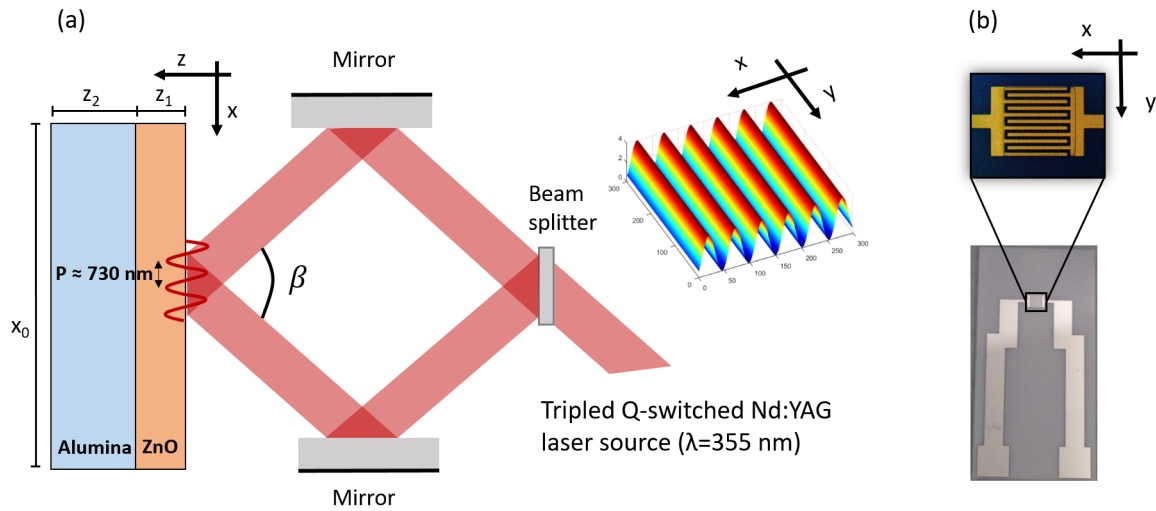
Figure 3.2 – (a) Schematic two-beam DLIP set-up, energy distribution simulation of 1D pattern and (b) detailed image of the IDT electrodes with the coordinates.

To study the influence of the laser fluence, the samples were processed at 85 mJ/cm^2 and 165 mJ/cm^2 and a single shot was used in all the processes. The samples will be named DLIP85 and DLIP165, respectively.

Finally, the last fabrication step of the sensor device consists on depositing Pt IDT electrodes on top of the ZnO thin film with the same fabrication steps used to deposit the heater (Fig. 3.1 (e)). In order to improve the adhesion of the metal to the substrate, a 25 nm-thick chromium (Cr) layer was deposited for the subsequent 200 nm-thick Pt sputtering, both in the heater and in the IDT electrodes. The IDT electrodes have a separation and width of 50 μm, a length of 0.9 mm and cover an area of 1 mm^2. They were deposited on top of the ZnO layer (they are usually beneath) to avoid the possible damage of the Pt IDT electrodes when the DLIP process was performed. The maximum and minimum of interference are perpendicular to the IDT electrodes, as indicated by the coordinates in Fig. 3.2 (b).

3.1.2   Film characterization

For the ZnO film characterization, samples with a size of 6 x 7 mm^2 were fabricated following the same sputtering recipe described in 3.1.1. Afterwards, some of them were annealed and others were processed by DLIP, as explained in the previous section.

For morphological characterization, JPK Nanowizard 3 atomic force microscope (AFM) was used. Tapping mode images were obtained using silicon Tap300-G cantilevers with a resonance frequency around 300 kHz. The tip radius is smaller than 10 nm and the half-cone angle is around 25 °.

The film thickness was precisely determined from the cross-section analysis performed by a SEM Quanta 3D Field Emission Gun (FEG) from FEI Company. The same equipment was used to obtain surface images.

The crystal structure of the ZnO thin films was characterized by grazing incident X-ray diffraction (GIXRD) at 2° of incident angle by means of a PANalytical X'PERT PRO MRD diffractometer (Cu Kα1, λ = 1.5406 Å and Cu Kα2, λ = 1.5444 Å) and a parallel plate collimator (0.27° of aperture). The scan angle was chosen between 20° and 100° with a scan step of 0.02°. To calculate the average dimension of crystallites using the Scherrer method [147], a narrower plate collimator was used (0.09° of aperture) between 32° and 39° of scan angle. In this case, also a lanthanum hexaboride (LaB$_6$) powder, standard reference material 660c from the National Institute of Standards & Technology (NIST), was measured with the same experimental conditions in order to determine the instrumental broadening.

In order to simulate the transient temperature of the irradiated samples, optical properties such as reflectance (R) and transmittance ($T_{trans.}$) have been measured for ZnO as-grown on alumina in the 300-1100 nm wavelength range using a Bentham PVE300 UV/Visible/IR integrated spectrophotometer.

X-ray photoelectron spectroscopy (XPS) was recorded by a K-Alpha Thermo Fisher Scientific spectrometer in order to obtain the non-stoichiometry of the samples and the different zinc-oxygen bonds at the surface. The area analysed was 400 μm^2 and the source was a monochromatic radiation Al Kα at 1486.68 eV operating at 12 kV. A charge compensation was carried out through a Flood Gun. All the measurements are referenced to the C1s core level peak at 285.0 eV.

The composition depth profile of different ions was measured using a time of flight secondary ion mass spectrometer (TOF-SIMS 5, ION TOF) in order to see the laser interference influence on the ZnO depth. The mass spectrum was obtained by measuring the time-of-flight distribution of the positive ions coming from the sample surface into the detector. The primary ions source was Bi$^+$ operating at 25 keV and the spot size for the depth profile was 26 μm x 26 μm. Sputtering was done using 1 keV oxygen beam over a 250 μm x 250 μm of raster size area.

3.1.3 Electrical characterization

The electrical measurements were performed inside a cylindrical sealed stainless steel chamber with a volume of 0.86 l (see Fig. 3.3 (a)). The sensor was introduced into a connector provided by Digy-Key Electronics (ECC04DKWN-S1723), as shown in Fig. 3.3 (b) and thanks to the contact pressure, no bonding was needed[1]. The connector and the sensor were supported in a stainless steel piece, as shown in Fig. 3.3 (c) to ensure that the sensor was kept at the center of the chamber.

A schematic layout of the set-up is shown in Fig. 3.4. The feedthrough connections in the chamber were used to control the heater temperature and to measure the conductivity of the sensor. A constant voltage of 3 V was applied between the IDT electrodes, so intensity measurements were achieved through a Keithley 2000 Multimeter connected via General Purpose Interface Bus (GPIB) to the computer where a Labview$^©$ program is acquiring the data. The power consumption of the Pt heating element was doubly

---

[1]This connector will be used in all the following chapters.
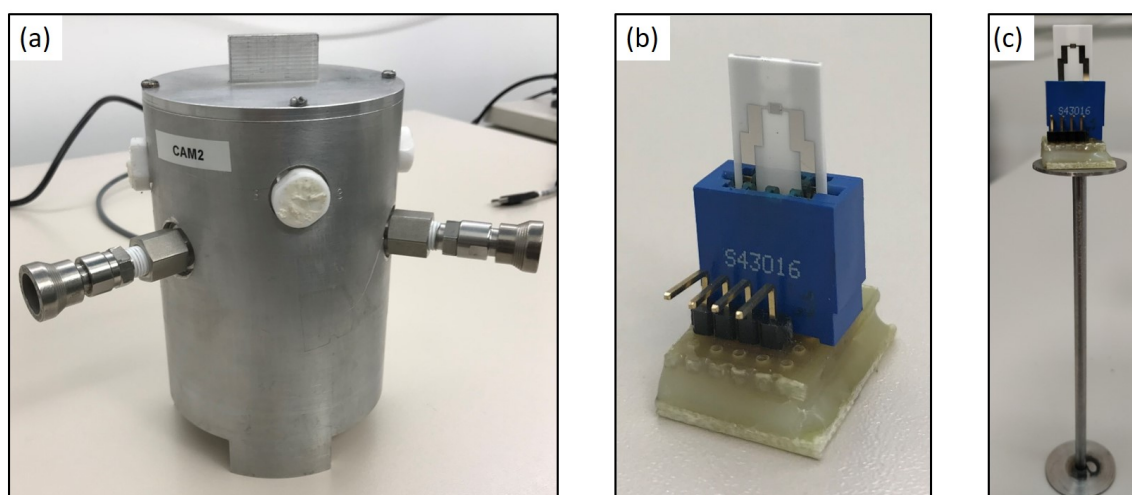
Figure 3.3 – (a) Cylindrical sealed stainless steel chamber with a volume of 0.86 l, (b) connector for the sensor contacts and (c) connector supported in a stainless steel piece.

calibrated with a thermographic camera and a Pt100 resistor, so the heater is power controlled by a programmable voltage source (AMREL PPS-1326).
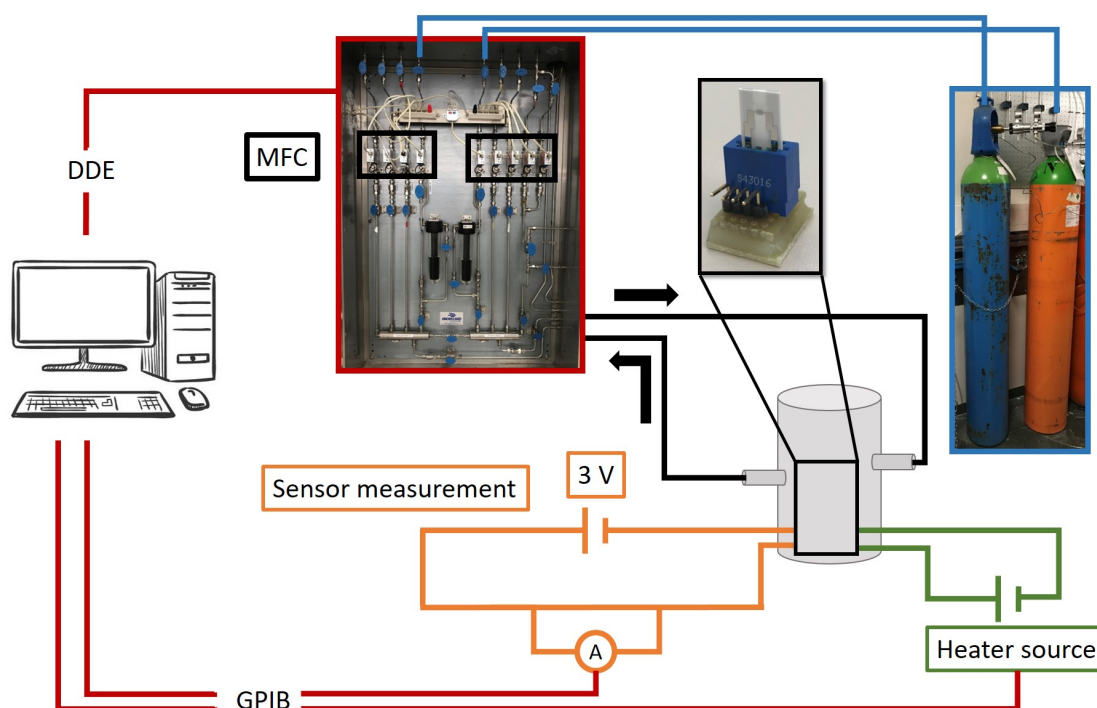
Figure 3.4 – Schematic layout of the set-up used for the electrical measurements.

The atmosphere inside the chamber was controlled by means of mass flow controllers (MFCs)[2] from Bronkhorst Hi-Tech, which were monitored through a dynamic data exchange (DDE) communication via Labview©. The NO_2 gas was taken from certified bottle

---

[2]MFCs are devices used to measure and control the flow of liquids and gases. The MFCs setpoint can be changed from 0 to 100 % and depending on this value the device will set the rate of flow to the given

(Air Liquide) of 50 ppm mixed with synthetic air. In all the experiments, a total flux of 400 standard cubic centimetres per minute (sccm) was used.

In this chapter, the response of the devices, SR, to the oxidizing gas NO_2, is defined as:

$$SR = R_{gas}/R_{air} = G_{air}/G_{gas} \tag{3.1}$$

where R_{air} is the resistance of the sensor in air, and R_{gas} represents the sensor resistance after 30 min of gas exposure. The conductivity (G) is defined as the inverse of the resistance. For all the following chapters, the response time (t_{90}) will be defined as the time required for the sensor to reach the 90% of the maximum response after 30 min and the recovery time (t_{10}) as the time elapsed until the 10% of the initial baseline resistance is reached after the gas extraction.

3.2 Results and discussion

3.2.1 Morphological and structural characterization

The AFM morphology studies reveal a homogeneous grained surface for as-grown and thermal treated samples with a slight increase in the grain size when annealing temperature increases (Fig. 3.5). These results present good agreement with several studies of ZnO thin film grown by RF magnetron sputtering [148–150].

By contrast, on the samples treated by DLIP at 85 mJ/cm^2 (Fig. 3.6) a line structure can be observed with an average period of 730 nm. Two different phases of the material have appeared: at the maximum intensity of the interference, a smooth surface is shown with small cracks (Fig. 3.6 (e)) and at the minimum of the interference the grain structure has remained intact (red rectangle) in Fig. 3.6 (d). A profile of the topography is shown in Fig. 3.6 (f), where the rugosity modification can be noticed. The duty cycle parameter (3.2) obtained goes from 0.58 to 0.23, indicating that the processed part is usually half of the period or less.

$$\Lambda = \frac{Processed\,part}{Period} \tag{3.2}$$

For the samples treated at 165 mJ/cm^2, as it can be seen in Fig. 3.7, all the surface is processed ($\Lambda = 1$) and smooth, but also a periodic line structure with the same period can be appreciated. In this case, the energy absorbed by the sample has been higher, removing some part of the material as it can be proven by the small dispersed spheres shown in Fig. 3.7 (c) and (d). At some small areas of the sample (not shown here) the duty cycle has decreased down to 0.88. The spread result of the duty cycle at both laser fluences is a consequence of the inhomogeneous distribution of the laser spot. The changes in morphology shown because of the fluence modification can be explained as an increase of the molten material at the surface when the fluence is higher. This mechanism has

---

setpoint. The flow rate is specified as a percentage of its calibrated full scale flow and is supplied to the MFCs as a voltage signal trough Labview$^{©}$.
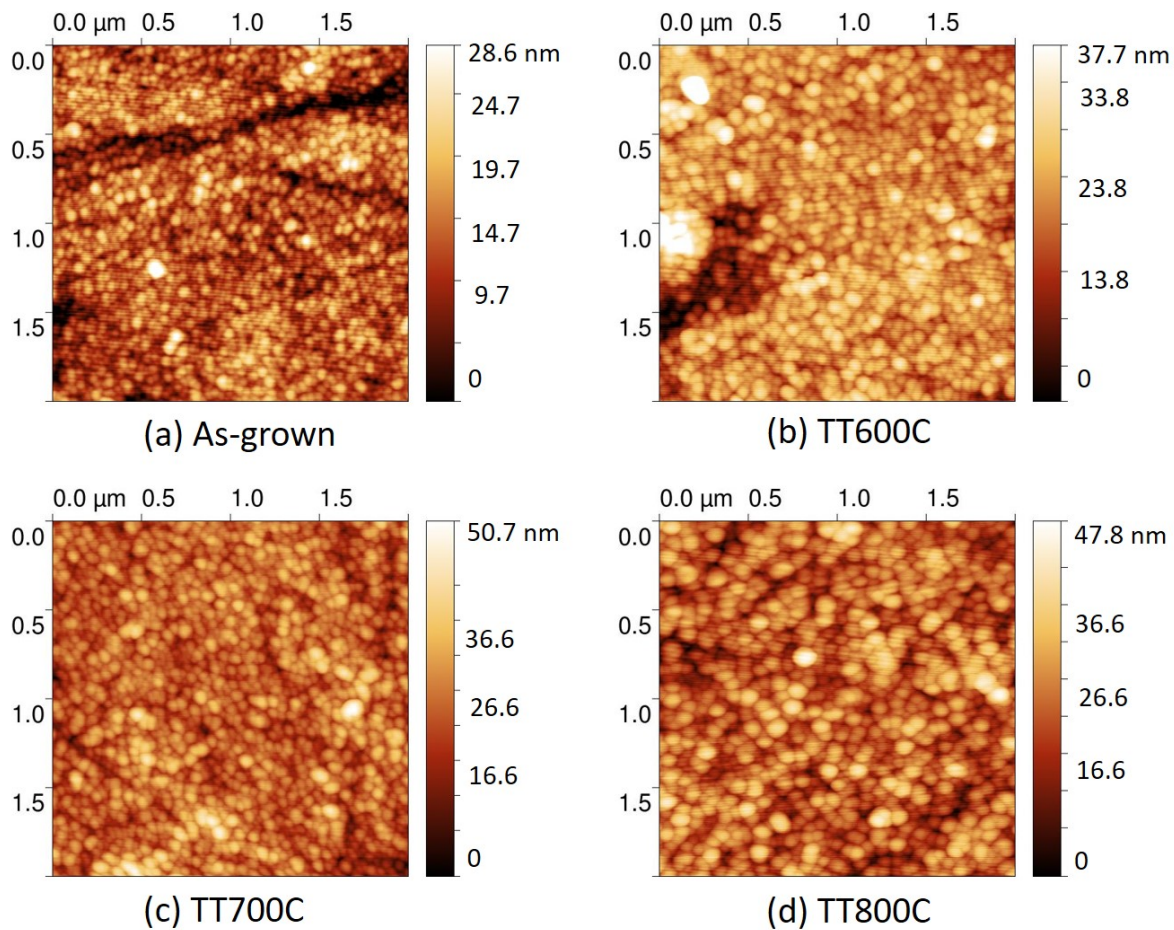
Figure 3.5 – 2 μm^2 AFM tapping mode images of ZnO on alumina: (a) As-grown, (b) thermally treated at 600 °C, (c) 700 °C and (d) 800 °C.

been already studied on TCO [151] and metallic surfaces [152] and it is called Marangoni convection [153].

From the cross-section of the sample processed at 85 mJ/cm^2 (see Fig. 3.8), the grained (red arrows) and the smooth (blue arrows) parts can be appreciated, indicating that the laser processing at the interference maximum has changed the grain structure at the surface as it was shown in the AFM images. The thickness of the ZnO thin film is calculated taking into account the tilt correction and as all samples were made in the same ZnO RF sputtering deposition process, an average thickness of 179.5 nm is considered for all of them.

Through the GIXRD measurement from 20° to 100° in 2θ using a 0.27° plate collimator, the peaks of the wurtzite ZnO structure have been identified (ICDD PDF card #00-036-1451). A preferred orientation in the (002) direction is noticed in all the samples and the second most intense peak corresponds to the (103) orientation (Fig. 3.9).

As shown in Fig. 3.9, the sample treated by DLIP at 165 mJ/cm^2 presents better crystallinity than the processed by the lower fluence, what could be associated to the higher temperature reached by the sample. This behaviour could indicate that the laser
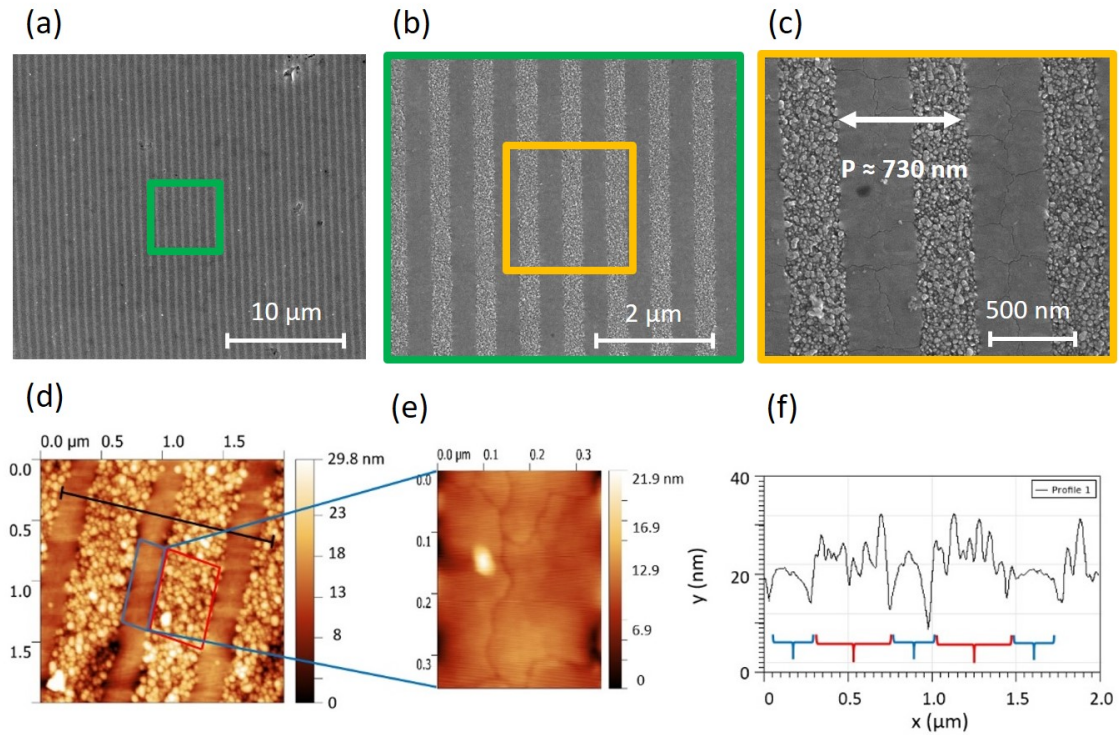
Figure 3.6 – (a), (b) and (c): SEM images with different magnifications of DLIP85. (d) 2 μm^2 AFM tapping mode image of DLIP85, (e) zoomed image of the processed part with cracks and (f) section profile of the line pointed out on (a).

treatment is acting similarly to the annealing process from the crystallographic point of view, since it improves the crystal structure with the temperature. In the sample processed with the low fluence, 85 mJ/cm², both parts (as-grown and laser processed regions) contribute to the spectrum, showing a wider (002) and (103) peaks. These peaks could be deconvoluted in two different contributions: one centred at lower angles corresponding to the as-grown region and the other one and more intense, coming from the laser radiated regions with a maximum around 34.4° and 62.9° for the (002) and (103) peaks, respectively.

In order to obtain more accuracy to calculate the average crystallite size (D), a GIXRD measurement from 32° to 39° in 2θ using a 0.09° plate collimator was performed. D was calculated using the Scherrer equation:

$$D = \frac{k\lambda}{wcos(\theta)} \tag{3.3}$$

where k is constant that depends on the unit cell geometry, in this case 0.94, λ is the wavelength of the radiation (1.5406 Å) and θ is the peak positions. w is the full width at half maximum (FWHM) of the ZnO (002) peak, taking into account the instrumental broadening.

As shown in Table 3.1, the average value of the crystallite size for the DLIP85 sample is in between the values calculated for the as-grown and the DLIP165 samples, because it
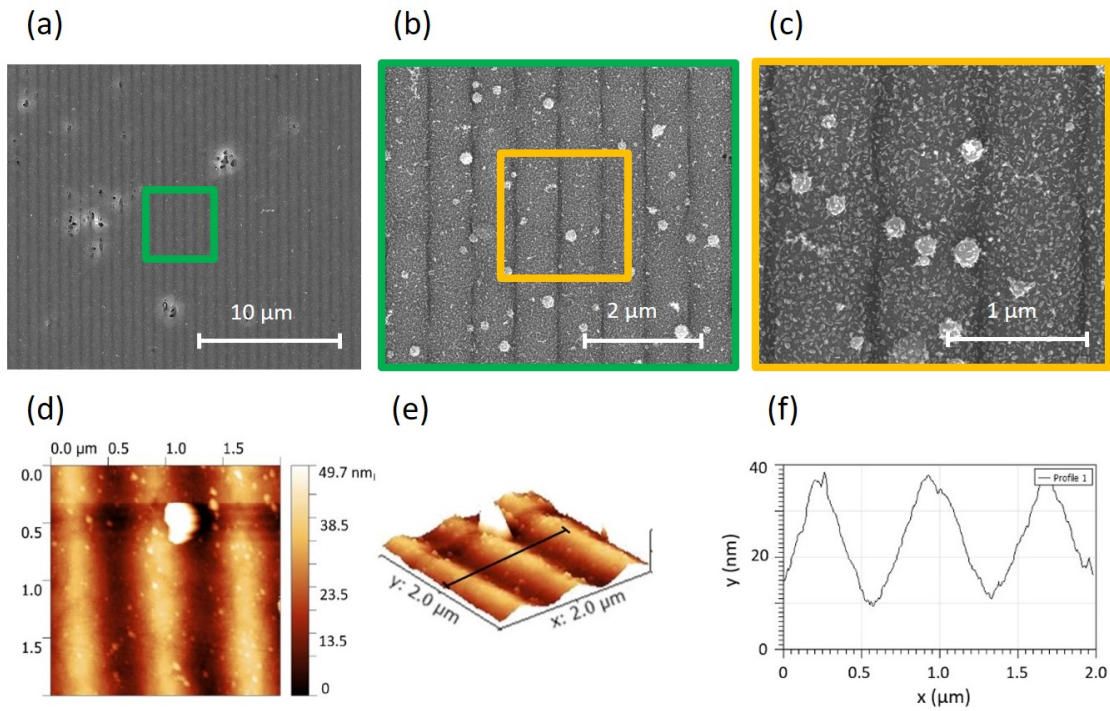
Figure 3.7 – (a), (b) and (c): SEM images with different magnifications of DLIP165. (d) 2 μm^2 AFM tapping mode image of DLIP165, (e) 3D image of the topography and (f) section profile of the line point out on the 3D image.
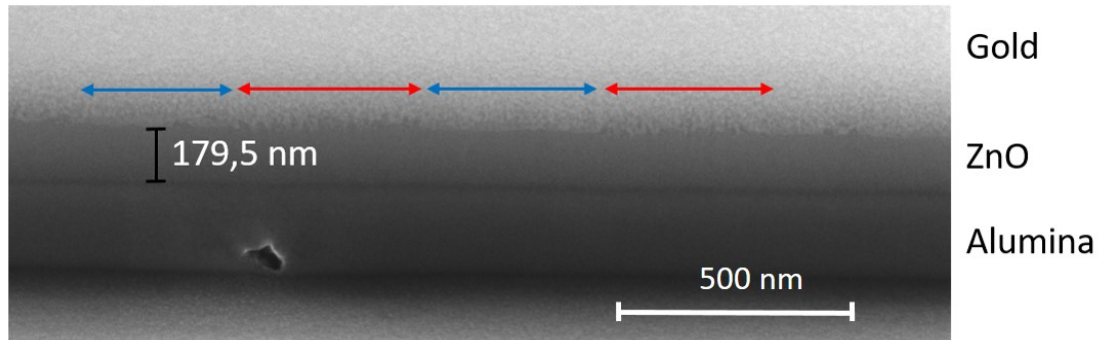
Figure 3.8 – SEM image of a cross-section of the sample processed by DLIP at 85 mJ/cm^2.

must be considered as a combination between the processed and non-processed areas. For the annealing samples, the average crystallite size increases as a function of the annealing temperature, what is in agreement with the AFM images.

The lattice parameters of the hexagonal structure have been calculated through the following formula:

$$\frac{1}{d^2_{(hkl)}} = \frac{4}{3}\left(\frac{h^2 + hk + k^2}{a^2}\right) + \frac{l^2}{c^2} \tag{3.4}$$

The parameters a = b were calculated using the (103) peak and the c lattice parameter was determined using the (002) direction (Table 3.1). The interplanar distance (d) on
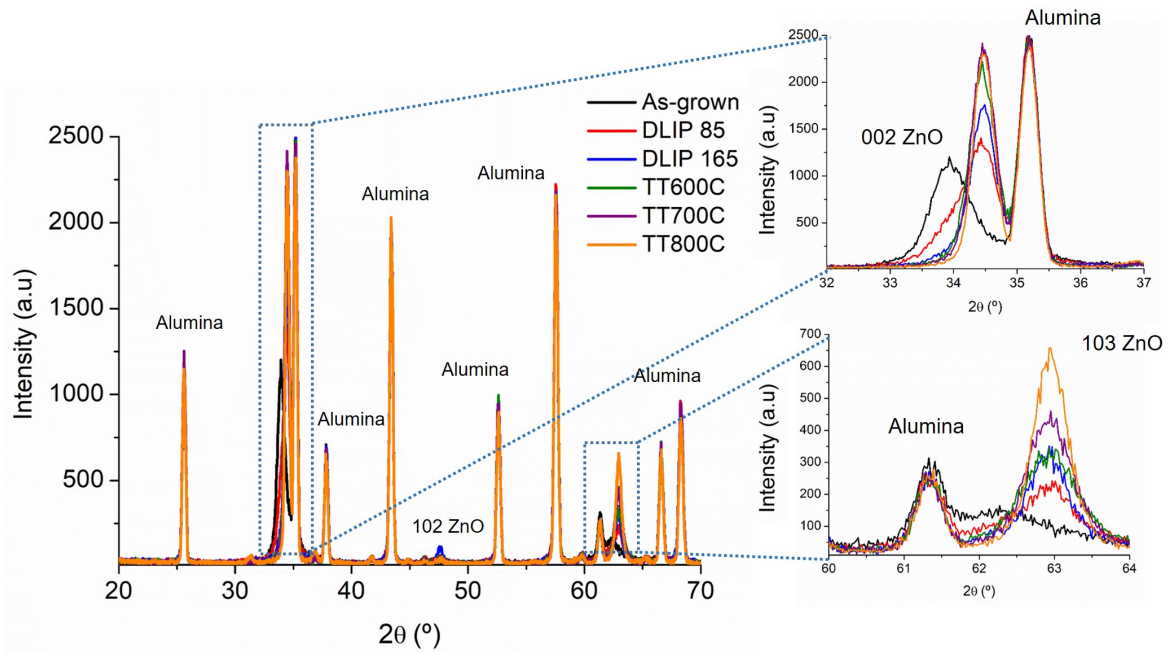
Figure 3.9 – GIXRD measurements with 0.27° plate collimator of the ZnO as-grown, ZnO treated with DLIP at 85 mJ/cm^2 and 165 mJ/cm^2 and ZnO thermally treated at 600 °C, 700 °C and 800 °C.

Samples	D (nm)	d (002) (Å)	a (Å)	c (Å)	σ_f on (002) (MPa)
Bulk ZnO	–	2.602	3.249	5.205	–
As-grown	13.0 ± 0.6	2.63 ± 0.04	3.0 ± 0.1	5.27 ± 0.09	$-3.05\cdot10^3$
DLIP85	15.0 ± 0.6	2.60 ± 0.04	3.2 ± 0.2	5.21 ± 0.08	$-9.53\cdot10^1$
DLIP165	31.1 ± 0.6	2.59 ± 0.04	3.3 ± 0.2	5.21 ± 0.08	$+2.50\cdot10^2$
TT600C	23.5 ± 0.3	2.60 ± 0.04	3.2 ± 0.2	5.20 ± 0.08	$+1.91\cdot10^2$
TT700C	31.2 ± 0.3	2.59 ± 0.04	3.2 ± 0.2	5.20 ± 0.08	$+2.49\cdot10^2$
TT800C	44.4 ± 0.5	2.59 ± 0.04	3.2 ± 0.2	5.20 ± 0.08	$+2.83\cdot10^2$

Table 3.1 – Average crystallite size (D), interplanar distance (d) on the (002) direction, lattice parameters and stress on (002) for the different investigated samples and compared with ZnO bulk data (ICDD PDF card #00-036-1451).

(002) is determined using the Bragg's Law and the stress on that direction is calculated through the next equation for the ZnO, taking into account the biaxial strain model [154,

155]:

$$\sigma_f = -233 \cdot 10^9 \frac{(c - c_0)}{c_0} Pa \tag{3.5}$$

Comparing GIXRD results obtained for ZnO as-grown and DLIP85, it can be assumed that the processed/smooth part of the DLIP85 has recrystallized into a better crystal structure, leading to an average decrease of the compressive stress. For the sample treated at higher energy distribution of the laser (DLIP165) and for the annealed samples, the stress becomes tensile and increases with temperature until $2.83 \cdot 10^2$ MPa for TT800C.

3.2.2   Theoretical temperature simulations

After observing the different morphologies and textures shown on the AFM and SEM characterization, it is expected to find a threshold temperature, above which the material experiences structural and topological modifications. In order to investigate the transient temperature of the system, the 2D heat transfer equation (3.6) of a ZnO thin film on top of alumina has been simulated for a DLIP laser shot.

$$\rho C_p(T)\frac{\partial T}{\partial t} - \nabla(K\nabla T) = Q(x, z, t) \tag{3.6}$$

Where ρ, $C_p(T)$ and K are the density, the heat capacity and the coefficient of thermal conductivity of each material respectively, T and t are the temperature and time and Q is the heat source. The horizontal and vertical coordinates, x and z are expressed in Fig. 3.2.

$Q(x, z, t)$ is the heat source (3.7) coming from the laser pulse and depends on the properties of the laser source, properties of the materials and parameters of the set-up.

$$Q(x, z, t) = \alpha I(1 - R) \tag{3.7}$$

Where R and α are the optical properties of the system: reflectivity and absorption coefficient. The intensity distribution of the laser, I, can be expressed as the product of three terms: interference energy distribution in space, $\Phi(x)$, temporal Gaussian distribution, $I_t(t)$, and the absorbed attenuation term following the Beer-Lambert law:

$$I(x, z, t) = \Phi(x)I_t(t)\exp(-\alpha z) \tag{3.8}$$

The temporal distribution (3.9) is expressed as a function of the standard deviation $\left(\sigma = \frac{\tau_p}{2\sqrt{2\ln 2}}\right)$, the pulse arrival time, t_0, and the pulse duration of the laser at FWHM, τ_p:

$$I_t(t) = \frac{1}{\sigma\sqrt{2\pi}}exp\left[\frac{-(t - t_0)^2}{2\sigma^2}\right] \tag{3.9}$$

The energy intensity distribution in space of 2D interference pattern at the surface of the ZnO is considered as following:

$$\Phi(x) = 4\Phi_0 \cos^2\left[kx\sin\left(\frac{\theta}{2}\right)\right] - 4\Phi_0 \cos^2\left(\frac{\theta}{2}\right)\cos\left[2kx\sin\left(\frac{\theta}{2}\right)\right] \tag{3.10}$$

where Φ_0 is the fluence of each beam and k is the wave number at the laser wavelength ($k = 2\pi/\lambda$). The first term is due to the beam interference [152, 156] and the second one is due to the p-polarization of each interference beam.

The laser FWHM is 8 ns and the parameters concerning the properties of the materials used in the simulation for the ZnO and alumina are summarized in Table 3.2.

Material	ρ (kg/m^3)	$C_p(T)$ (J/(mol·K))	K (W/(m· K))	m_x (10^{-3} kg/mol)
ZnO	5600	$\dfrac{(47.8 + 6.1 \cdot 10^{-3}T - 7.6 \cdot \frac{10^5}{T^2})}{m_{Zn}}$	50	81.379
Alumina	3950	$\dfrac{(92.4 + 3.8 \cdot 10^{-2}T - 2.2 \cdot \frac{10^6}{T^2})}{m_{Al_2O_3}}$	16	101.961

Table 3.2 – Properties of ZnO and alumina used in the simulation of the heat transfer equation: density (ρ), heat capacity ($C_p(T)$) [157], thermal conductivity (K) and molar mass (m_x).

The thermal conductivity of the ZnO [158] and the alumina [157] have been estimated as the average in the interval 300-1300 K.

The measured reflectance and transmittance at $\lambda = 355$ nm of the as-grown ZnO thin film on alumina were $R = 0.1441$ and $T_{trans.} = 0.00875$. From R and $T_{trans.}$ and taking into account the ZnO thickness, the absorption coefficient has been calculated through the Beer-Lambert law and the result is $\alpha = 2.446 \cdot 10^7$ m^{-1}.

The heat transfer equation was solved by the finite element method [159] and the results, shown in Fig. 3.10, belong to a vertical cut section where the thickness of ZnO and alumina are $z_1 = 179.5$ nm and $z_2 = 5$ μm, respectively. The width of both materials is considered $x_0 = 1.46$ μm (double of the period). The arrows on top of Fig. 3.10 (a) and (b) indicate the minimum (dashed) and the maximum of interference where the transient temperature has been plot in Fig. 3.10 (c).

In Fig. 3.10 (a) and (b) the temperature distribution in space of the ZnO thin film and part of the alumina is shown for an interference energy distribution of 85 mJ/cm^2 and 165 mJ/cm^2 of fluence, when the temperature is the maximum in the system.

The transient temperatures simulated in Fig. 3.10 (c) present an agreement with the research done by N. Nedyalkov [160], where a maximum temperature of around 2300 K was simulated for a non-interference distribution of a laser system similar to the one presented here into 20 nm of ZnO on Tantalum at 150 mJ/cm^2. Higher temperature than in our investigation is recorded, possibly due to a longer laser pulse (15 ns instead of 8 ns) and a thinner ZnO thin film.

In Fig. 3.10 (c), the highest temperature at the maximum and minimum of the interference for both fluences are reached with 2 ns difference between them, result that
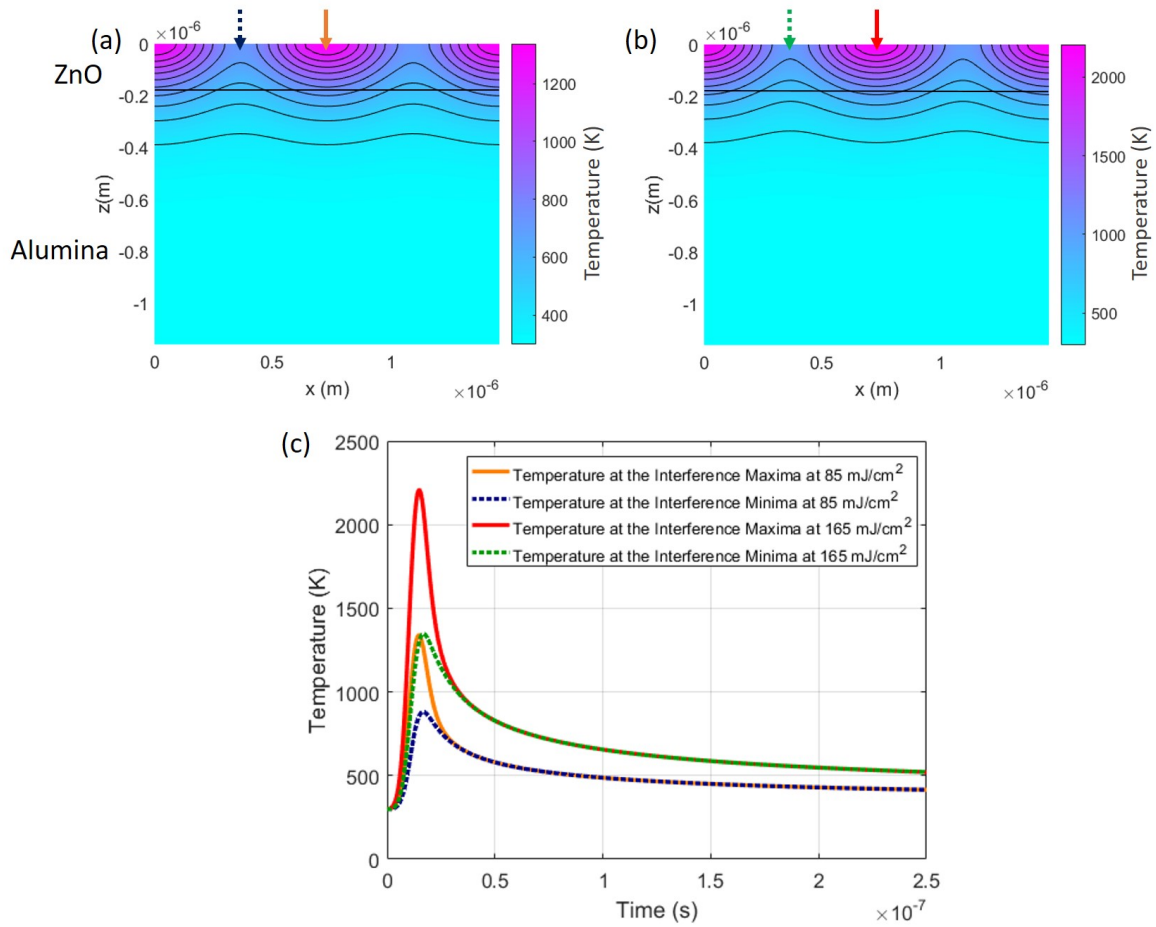
Figure 3.10 – Computer simulation of the (a) temperature distribution on the ZnO and alumina for an interference energy distribution of 85 mJ/cm^2 and (b) 165 mJ/cm^2 of fluence, when the temperature is the maximum in the system. (c) Transient temperature for the first 250 ns after the shot at the minimum and maximum of interference at 85 mJ/cm^2 and at 165 mJ/cm^2.

can be expected due to the time that the heat flux $g(x, z, t)$ flows from maxima to minima of interference. In Fig. 3.11, a schematic drawing of the heat flux diffusion in all the directions is shown, explaining the delay time between the maximum temperatures reached at the maximum and minimum of interference.

The melted or smooth areas for the sample DLIP85 achieve temperatures lower than the ZnO bulk melting point ($T_{ZnO} = 2248$ K), what could be justified by the fast pulsed heating process followed by the slow cooling-down and by the fact that as a ZnO thin film, melting temperatures may be different to the bulk ones.

Comparing the width measured with the AFM of the non-processed part of samples DLIP85 and the temperature profile obtained, one can determine an approximate annealing temperature threshold (T_{th}). The non-processed parts on the AFM image (Fig. 3.6 (a)) have an average width of 383 nm which is equal to the width obtained if we consider an annealing threshold of about 900 K (Fig. 3.12). So, it can be assumed that areas of the sample that reached temperatures higher than 900 K have been structurally modified.

Both temperatures reached at the surface by the sample processed by DLIP at
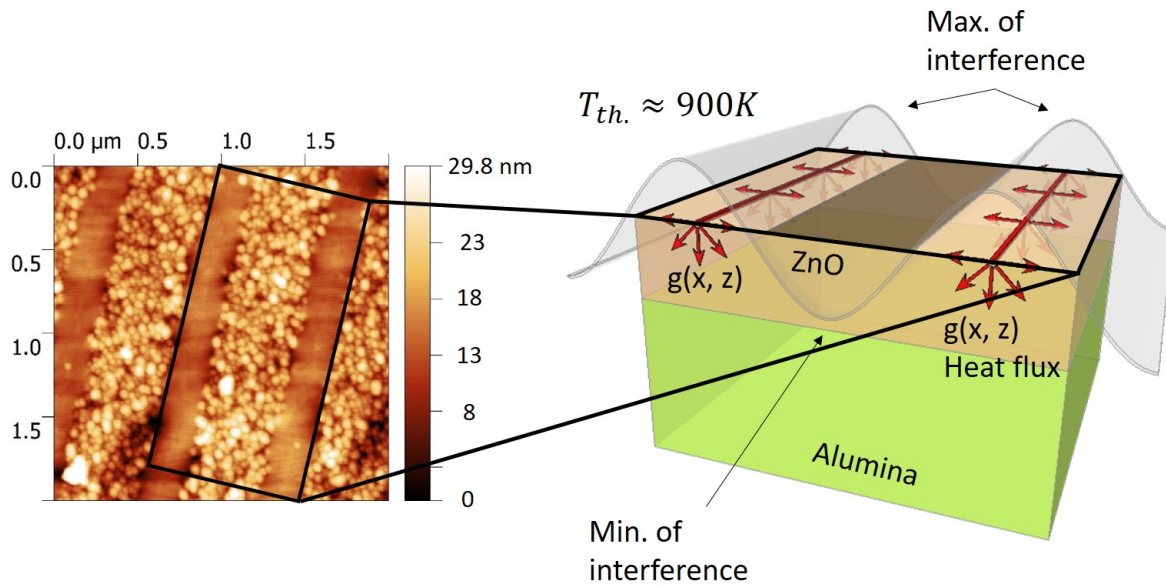
Figure 3.11 – Schematic image of the heat flux diffusion from the maximum to the minimum of interference, jointly with an AFM image of DLIP85, indicating which part of the sample it is referred to.

165 mJ/cm^2 (at the minimum and at the maximum of interference) are over the annealing threshold, what shows good agreement with the AFM images where all the surface presents a wavy behaviour but with no difference in roughness and a uniform aspect with detached spheres. On the other hand, from the holes and particles seen on Fig. 3.7 (a) an ablation threshold could have been exceeded when the higher fluence is employed, so that we could assume that it is in the range between 1400 K and 2200 K.

Nevertheless, all the temperatures simulated by the model have to be taken into account qualitatively, because small variations of the thermal and optical properties can lead to important differences on the presented temperature values.

3.2.3 XPS spectra

XPS measurements were performed to determine the non-stoichiometry of the ZnO thin film surface. In Fig. 3.13, the peak O 1s is shown for the six different samples. In all the cases, the O 1s core level can be expressed as the convolution of three different sources: the main peak with the lowest energy around 530.3 eV (OA), which is associated to O^{2-} ions in the wurtzite structure bounded to Zn^{2+} (Zn^{2+}-O^{2-}) [161, 162], the middle energy peak around 531.2 eV (OB) that is commonly related to oxygen deficient regions within the ZnO matrix [163], so it can be identified with oxygen vacancies, and the peak with the highest energy around 532.2 eV (OC) that comes from chemisorbed oxygens and hydroxyl species [164].

From the difference of binding energy between the peaks and the symmetric shape of the doublet Zn 2p spectra: Zn 2p$_{1/2}$ and Zn 2p$_{3/2}$ (see Fig. 3.14), it can be concluded
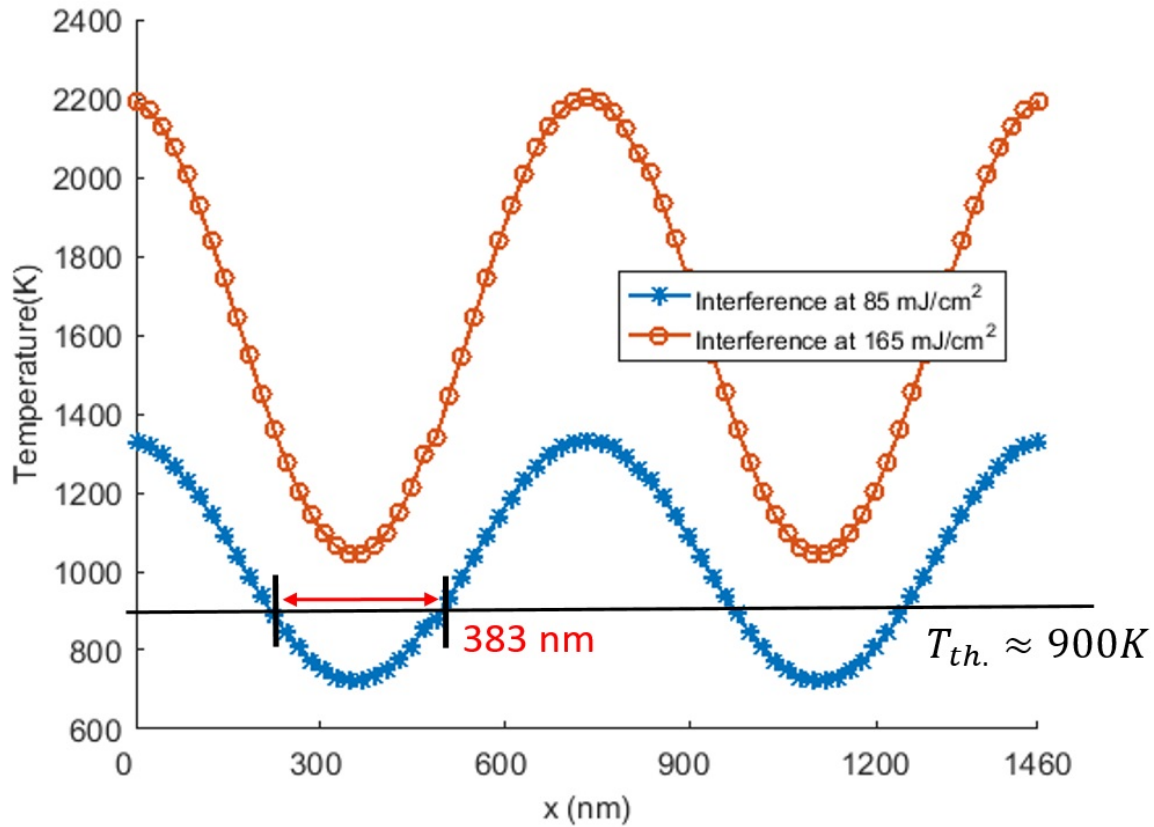
Figure 3.12 – Temperature as a function of position on the ZnO surface at two different fluences, when the temperature is the maximum in the system.

that the chemical state of the majority of Zn atoms is in the valence state Zn^{2+}[165].

In order to obtain quantitative information about the stoichiometry, the following ratios have been calculated:

$$\frac{OA}{Zn} = \frac{\frac{A_{OA}}{S_O}}{\frac{A_{Zn}}{S_{Zn}}} \tag{3.11}$$

$$\frac{(OA+OB)}{Zn} = \frac{\frac{A_{OA}+A_{OB}}{S_O}}{\frac{A_{Zn}}{S_{Zn}}} \tag{3.12}$$

where A_x is the area behind the peak x and S_O and S_{Zn} are the sensitivity factor for each element, 2.93 and 18.92 for the oxygen and Zn, respectively. In Fig. 3.15 the ratio between the area behind the OA and OB deconvolutions of the O 1s peak and the ZnO $2p_{3/2}$ (Zn) peak has been plotted for the different samples.

The difference between the two plotted curves in Fig. 3.15 suggests that the samples containing higher oxygen deficient regions are the thermal treated together with DLIP165 (OB contribution). On the other side, the as-grown ZnO shows a ratio (OA/Zn) far from the stoichiometry in the oxygen rich region, but by contrast, on the samples treated by laser or annealing, the OA/Zn ratio has diminished considerably, getting closer to 1:1
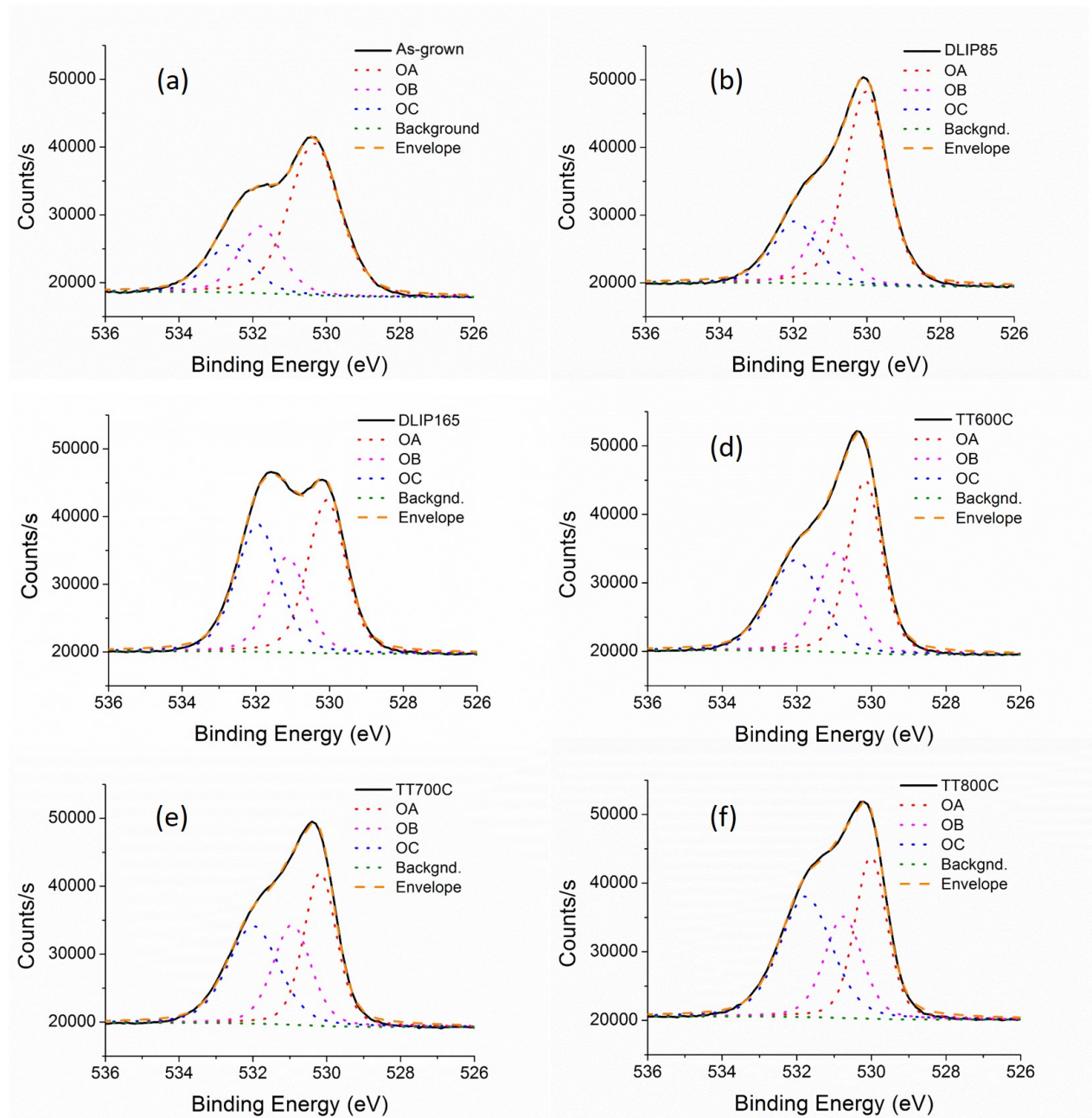
Figure 3.13 – XPS spectra of O 1s peak for the different samples and its deconvolution: (a) ZnO as-grown, (b) ZnO DLIP at 85 mJ/cm^2, (c) ZnO DLIP at 165 mJ/cm^2, (d) ZnO annealed at 600 °C, (e) ZnO annealed at 700 °C and (f) ZnO annealed at 800 °C.

ratio, especially for the cases of DLIP165 and TT800C. That could be a result of an increase of oxygen vacancies (V_0) and Zn interstitials (Zn_i).

Comparing the values obtained for the stress in Table 3.1 and the ratio $\frac{OA}{Zn}$ calculated through the XPS shown in Fig. 3.15, it can be noticed that tensile stressed samples (DLIP165, TT600C, TT700C and TT800C) present oxygen deficient ratio, while compressive stressed samples (as-grown and DLIP85) show oxygen rich ratio. This fact points out the relation between the stress and the stoichiometry, as shown on the work done
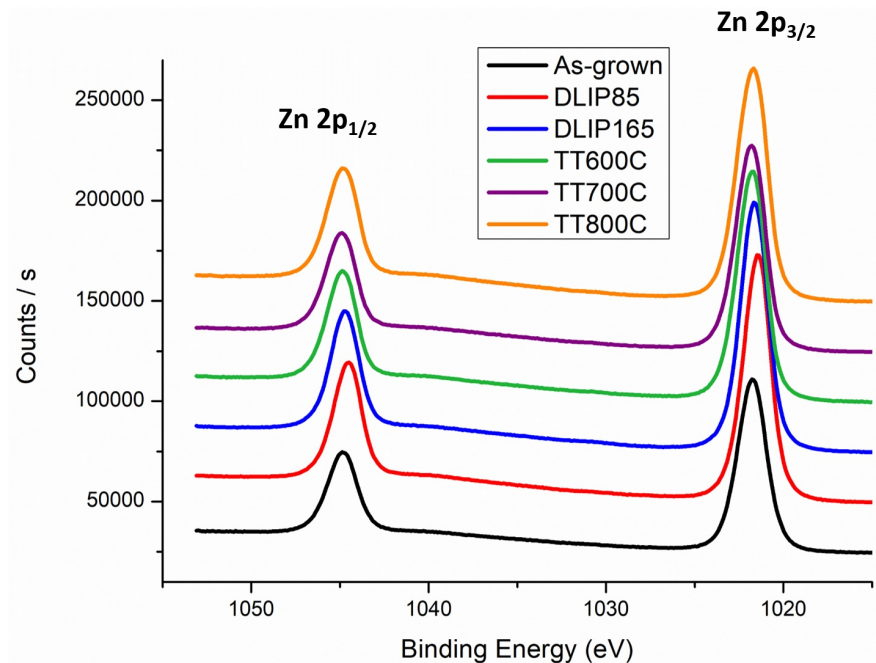
Figure 3.14 – XPS spectra of Zn $2p_{1/2}$ and Zn $2p_{3/2}$ peaks for the different samples.
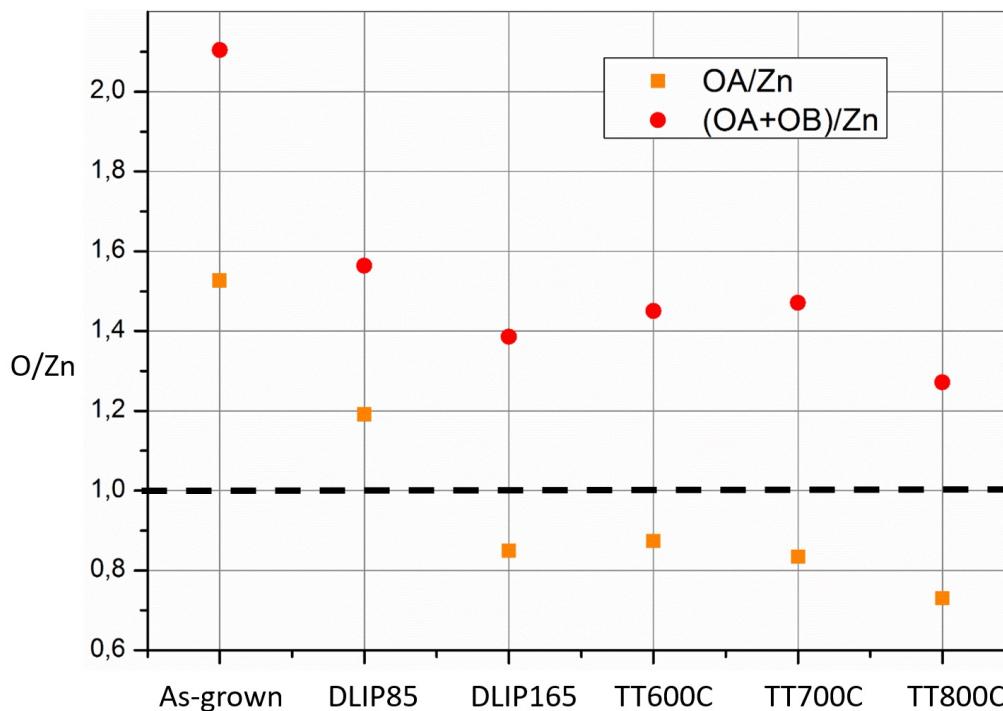
Figure 3.15 – Ratios OA/Zn and (OA+OB)/Zn for the different samples measured by XPS.

by T. Prasada Rao et al. [166] where the ZnO grown by spray pyrolysis presented an increase in oxidation state and compressive stress. On different sputtered ZnO investigations [167, 168], this behaviour is also shown, where the thin film stress decreases as the oxygen content during the growth increases in the chamber.

3.2.4 TOF-SIMS characterization

Positive TOF-SIMS in depth experiments were used to analyse the qualitative composition of the samples as a function of thickness. The ions detected related with ZnO were Zn^+, ZnO^+ and ZnO_2^+ and all of them presented a similar behaviour in depth. The alumina related ions detected were Al^+, AlO^+, Al_2^+ and AlO_2^+, which also showed a comparable behaviour among them (see Fig. 3.16). The presence of a small gradual decrease of the intensity for some of the ions in all the measurements during the first seconds of sputtering probably corresponds to the time needed to reach stationary conditions. As impurities or contamination, ions such as Na^+, Si^+, O^+, O_2^+, Ca^+, Ti^+ and CH_3^+ were measured due to the high sensitivity of the TOF-SIMS technique, but in the XPS results, with a precision of $> 0.1\%$ in concentration, only Cl and Ti impurities were measured, indicating that the rest of ions detected through TOF-SIMS could be negligible.
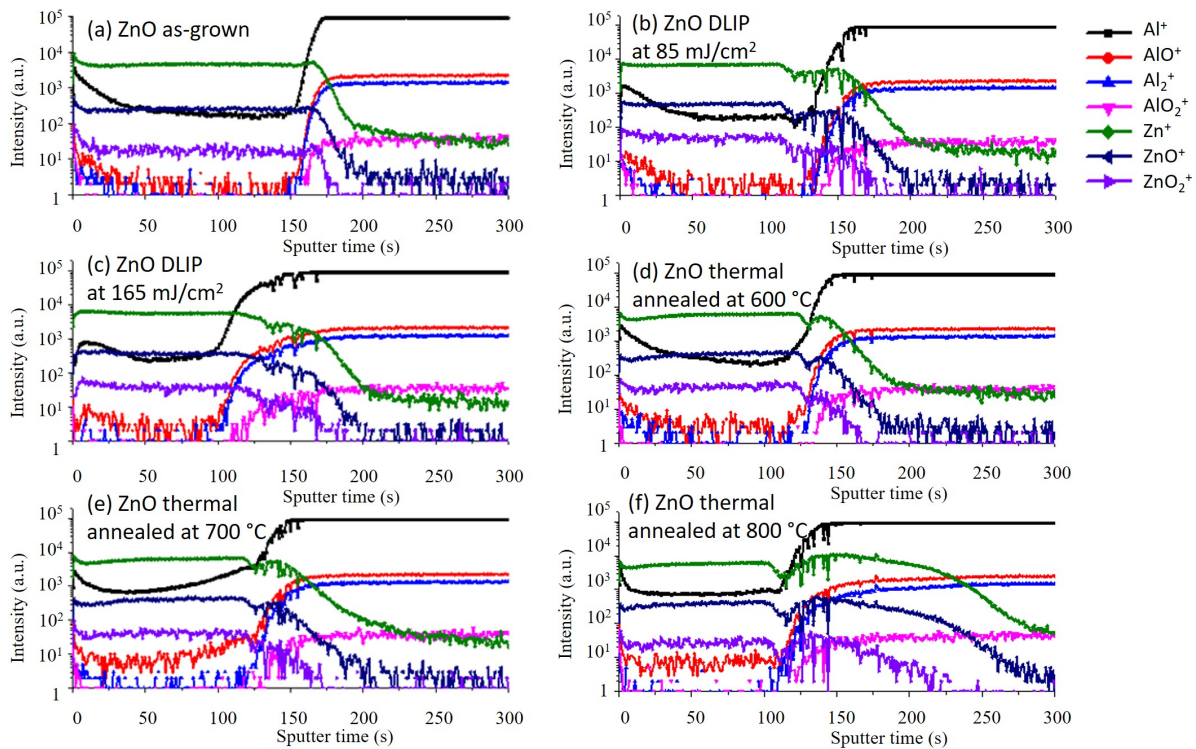
Figure 3.16 – TOF-SIMS measurements of ions containing Zn, oxygen and aluminium for the sample (a) ZnO as-grown, (b) ZnO DLIP at 85 mJ/cm^2, (c) ZnO DLIP at 165 mJ/cm^2, (d) ZnO annealed at 600 °C, (e) ZnO annealed at 700 °C and (f) ZnO annealed at 800 °C. Logarithmic scale is used for the intensity axis.

In Fig. 3.17, only ZnO^+ and Al_2^+ ions have been plotted, representing the ZnO and alumina behaviour, respectively. From the intensity increase of Al_2^+ and the decrease of ZnO^+ on the as-grown sample, Fig. 3.17 (a), the sputter rate for all the samples can be extracted. The reason why the as-grown sample has been chosen to extract the sputter rate is because after annealing and laser processing, diffusion between the ZnO and the alumina existed, so it was not possible to distinguish properly the interface limit between them. The sputter rate obtained is 1.11 nm/s.
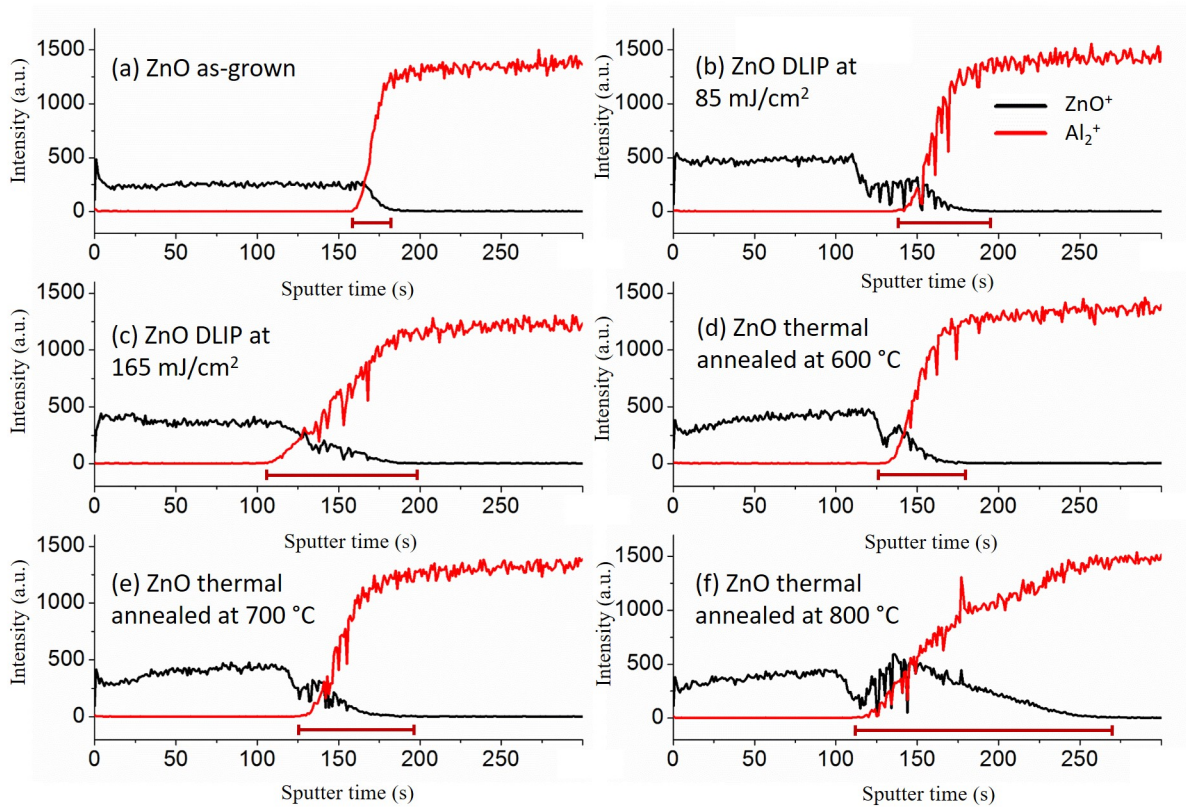
Figure 3.17 – TOF-SIMS measurements of ZnO^+ and Al_2^+ ions for the sample (a) ZnO as-grown, (b) ZnO DLIP at 85 mJ/cm², (c) ZnO DLIP at 165 mJ/cm², (d) ZnO annealed at 600 °C, (e) ZnO annealed at 700 °C and (f) ZnO annealed at 800 °C.

The interface region is indicated with a red line on each graph in Fig. 3.17, the as-grown sample presents the smaller interface region as it is expected (46.8 nm) and it goes in crescendo as a function of the annealing temperature. This is because on the samples annealed at higher temperatures, atoms received more energy/temperature, so they can diffuse and travel longer distances. For the samples processed by DLIP, a similar behaviour is presented, so an analogous argument can justify the results: samples treated at 85 mJ/cm² reached lower temperatures than the ones treated at 165 mJ/cm², as shown on the simulation results and consequently less diffusion existed (smaller interface region). The shape of the profile is different to the profile of the annealed samples because in this case, the high temperatures are in the nanosecond time scale.

For the DLIP85 (Fig. 3.17 (b)), the ZnO^+ ion starts with a slightly greater intensity compared to the as-grown sample (Fig. 3.17 (a)) until around 134 nm of ZnO sputtered (121 s of sputter), where it decreases to intensities very similar to the as-grown sample, around 250 of intensity. That peculiar behaviour could be explained by the fact that the laser effect at the fluence of 85 mJ/cm² mainly affects only the first 134 nm in depth of the ZnO, leaving the remaining 45.5 nm of ZnO unaltered from the composition point of view. This result is in concordance with the temperature simulations: in Fig. 3.10 (a), at the maximum of interference, 900 K (thermal threshold) are reached around 140 nm on ZnO depth. Moreover, this value is also in the same order of magnitude as half of the

lateral widening of the processed region observed by AFM (173.5 nm). So, it has been proved that the lateral and in depth modification of the ZnO thin film due to DLIP shot have similar values, as the heat diffusion is the same in all the directions.

For the case of DLIP165, the entire ZnO thin film is affected due to the higher temperatures reached. This fact is in agreement with the heat transfer simulation: the temperature at the minimum of interference at the interface ZnO/alumina is around 1015 K, exceeding the thermal threshold.

3.2.5   Gas sensing results

To demonstrate the sensing properties of the ZnO based sensors, the devices have been heated up to a typical detection temperature $\simeq$ 350 °C[3] under 400 sccm of dry air and stabilized during at least 24 h. In order to compare the NO_2 response of the different fabricated sensors, pulses of 30 min with several concentrations haven been carried out. The dynamic response of the sensors is shown in Fig. 3.18 for pulses of 5, 2 and 1 ppm of NO_2. While sensors processed by DLIP and annealed at 600 °C recover their resistance baseline relatively fast, the sensor annealed at 700 °C presents very slow recovery.
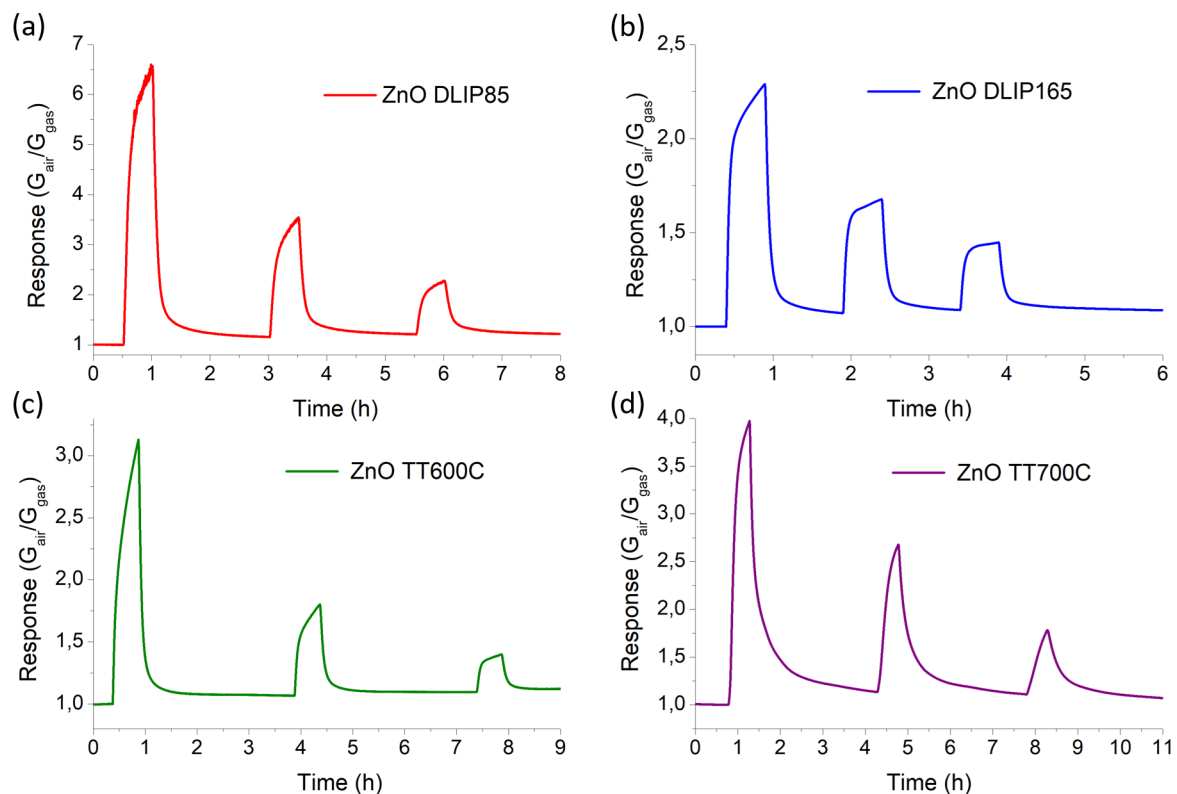
Figure 3.18 – Pulses of 5, 2 and 1 ppm of NO_2 at 350 °C for the sensor (a) processed by DLIP at 85 mJ/cm^2, (b) processed by DLIP at 165 mJ/cm^2, (c) annealed at 600 °C and (d) at 700 °C.

---

[3]The analysed temperature has been chosen taking into account the results of the following chapter, where ZnO based sensors present the optimal temperature at 350 °C.

A summary of the responses, response times and recovery times for all the concentrations are presented in Fig. 3.19. From the slope of the plots in Fig. 3.19 (a), the sensitivity of the sensors can be calculated, taking the values of 1.15 ppm^{-1}, 0.24 ppm^{-1}, 0.46 ppm^{-1}, 0.57 ppm^{-1} for DLIP85, DLIP165, TT600C and TT700C, respectively.
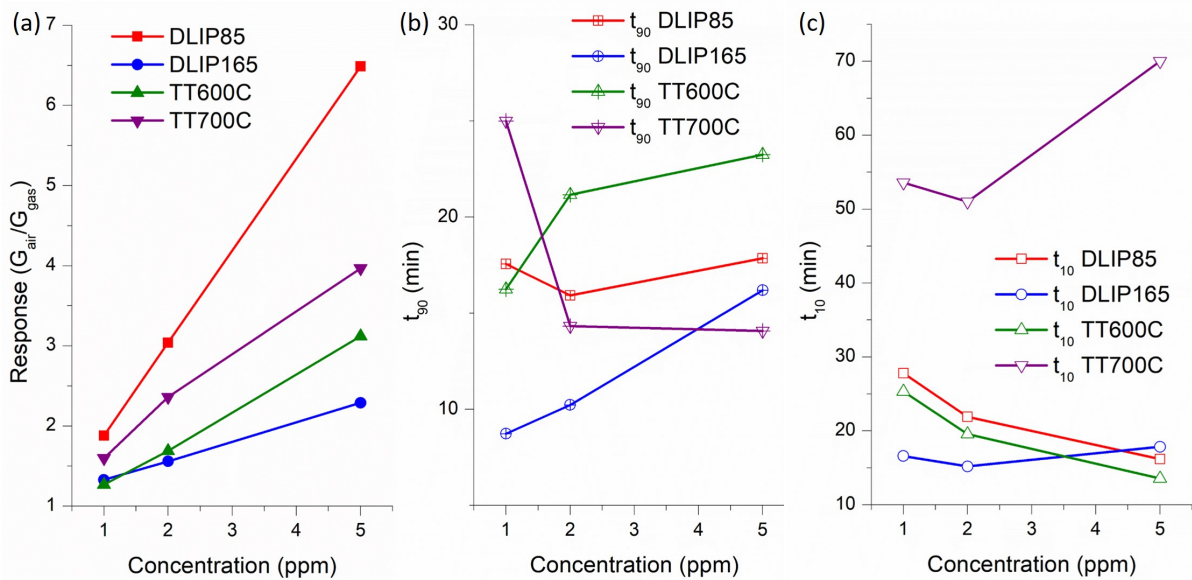
Figure 3.19 – (a) Responses versus concentrations at 350 °C, (b) response time, t_{90}, and (c) recovery time, t_{10}, for the all the tested concentrations.

The response for the two tested annealed samples increase as a function of the temperature of the thermal treatment for all the tested NO$_2$ concentrations, although the sensor annealed at 700 °C presents high recovery times, as mentioned, between 50 and 70 min. For the DLIP-processed sensors, the sensor DLIP85 has the highest sensitivity over all the sensors with a response and recovery times within the average. By contrast, the sensor processed by the DLIP at 165 mJ/cm^2 shows the lowest sensitivity, but the fastest response time for the lowest concentration (about 9 min). This result could be because the DLIP165 sample does not presents a granular surface, hindering the diffusion of the gas.

As mentioned in chapter 2, most of the proposed NO$_2$ detection mechanisms are based on the importance of the donor concentration defects, since they can give electrons to NO$_2$ molecules, decreasing the carrier density of the semiconductor. Two main possible reactions are involved in the process [88, 123]:

$$NO_{2(g)} + e^- \implies NO^-_{2\,(ads)} \qquad (3.13)$$

$$NO_{2(g)} + e^- \implies NO_{(g)} + O^-_{(ads)} \qquad (3.14)$$
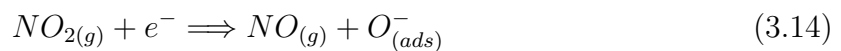
where NO$_2$ in gas form reacts directly with the semiconductor surface, generating adsorbed NO$_2$ species (3.13) or NO gas molecules and oxygen species (3.14). Aside from $NO^-_{2\,(ads)}$, other adsorbed NO$_2$ species could be generated, as it is explained in [125], always

through an electron given from a donor defect to a NO_2 molecule with a simultaneous reoxidation of an oxygen vacancy or Zn interstitial [132]. It is accepted that reaction (3.13) occurs for temperatures lower than 250 °C and reaction (3.14) for higher temperatures [88], therefore at the optimal temperature of the sensors presented here, the reaction (3.14) should take place.

3.3 Conclusions

ZnO deposited on alumina and processed by DLIP has been simulated through the heat transfer equation, contrasted with morphological, structural and compositional characterization and compared to thermally annealed samples at three different temperatures.

GIXRD measurements show that samples processed by DLIP present a crystal structure comparable to the annealed ones, with a preferred orientation towards (002) direction, especially comparing laser treated at 165 mJ/cm^2 with the thermally annealing at 600 °C.

For the samples treated by laser interference, temperatures as high as 2200 K and 1300 K have been obtained from the simulation at the maximum of interference on the surface of the ZnO for 165 mJ/cm^2 and 85 mJ/cm^2 of fluence, respectively. By contrast, temperatures decrease down to 1015 K and 680 K at the interface ZnO/alumina, for 165 mJ/cm^2 and 85 mJ/cm^2 of fluence, respectively, diminishing substrate damage, especially for DLIP85. A thermal threshold of 900 K has been calculated, so crystal modification occurs above this temperature.

Samples became richer on Zn with both thermal and laser treatment possibly through an increase of oxygen vacancies and/or Zn interstitials, what is an important issue for gas sensing applications. Moreover, the XPS experiments show a strong relationship between the stoichiometry and the stress on the samples.

The TOF-SIMS analysis reveals that the diffusion effects shown at the interface of the annealed samples are minimized for the case of DLIP165 and avoided for DLIP85. These characteristics could be very suitable when other materials in a device cannot undergo the treatment temperatures as in the case of flexible substrates or when the electrical properties of the substrate material cannot be modified, especially for the case of DLIP85 where the annealing threshold temperature does not reach the interface between the thin film and the substrate.

As a sensitive layer in a gas sensor device, the ZnO processed by DLIP detects low concentrations of NO_2 at a typical working temperature ($\simeq$ 350 °C). DLIP165 presents lower sensitivity than annealed sensors, but DLIP85 sensor increases the response compared to annealed sensors, maintaining the response and recovery times in the same order of magnitude as in TT600C samples. Hence, ZnO based sensors processed by DLIP at 85 mJ/cm^2 could be a very promising substitute of the annealed sensors, decreasing significantly the fabrication time of the device.

As a conclusion, DLIP is a much faster technique than thermal treatment and less invasive for the substrate, but with very similar structural effects. Besides, a different textured geometry can be formed at the surface what can be useful for different type of applications from optoelectronics to solar cells or as an active sensitive layer in gas sensor

devices, as presented here.

Chapter 4

Laser-induced periodic surface structures on ZnO based sensors

In this chapter, sensors based on sputtered ZnO thin film are annealed at 800 °C and processed with a femtosecond laser in order to generate LIPSS on its surface. Due to the changes on the surface structure, defects could be generated at the surface of the semiconductor and consequently a higher response could be expected for specific gases. Morphological and structural characterization of the ZnO processed with LIPSS is carried out to understand the modifications both in surface and in depth. Gas sensing performance is also studied under NO_2 atmospheres. In order to study the nanostructure effect, the characteristics are compared to only-annealed ZnO thin film sensors at 800 °C.

4.1 Experimental

4.1.1 Sensor fabrication

The fabrication steps of the ZnO sensing device are summarized in Fig. 4.1. The sensor is based on a 1 x 2 cm^2 polished alumina substrate, where a Pt heater was fabricated at the back side by photolithography followed by DC sputtering in an Edwards ESM 100 system (Fig. 4.1 (b)). The lift-off process was carried out with acetone. The same fabrication steps were used to fabricate Pt IDT electrodes on the top surface of the alumina (Fig. 4.1 (c)). The shape, dimensions and sputter recipe of the heater and the IDT electrodes are the same as in the previous chapter. 1 mm^2 of ZnO sensing layer was deposited on top of the Pt IDT electrodes by photolithography followed by RF sputtering in an Ar atmosphere (ZnO target 99.99 % purity) under $5 \cdot 10^3$ mbar of gas pressure in a Pfeiffer-Iontech system. The ZnO sputtering time was 1 h, the deposition temperature was between 21 °C and 23 °C and as for the Pt, acetone was used for the lift-off process (Fig. 4.1 (d)). Afterwards, as shown in (Fig. 4.1 (e)), the sensor device was thermally stabilized in a quartz oven at 800 °C during 4 hours in synthetic air (this sample will be named TT800C). The annealing temperature was chosen based on the results obtained in the previous chapter, where the best crystal structure was measured for the highest annealing temperature. After annealing, some sensors were processed by a femtosecond

laser for the LIPSS generation (Fig. 4.1 (f)). This sample will be labelled TT800C + LIPSS.
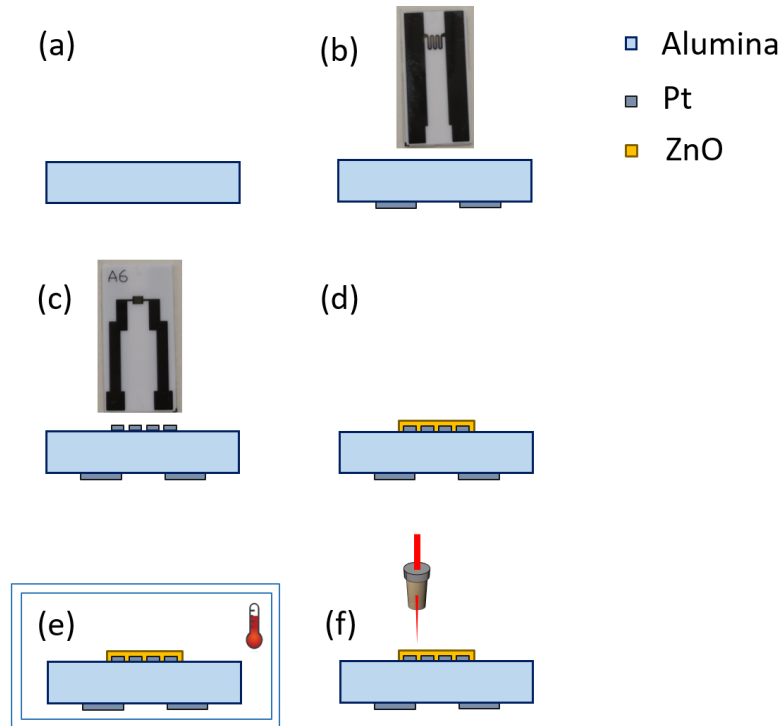
Figure 4.1 – Sensor fabrication steps: (a) polished alumina substrate, (b) DC sputtering of Pt heater deposited on the back side of the alumina substrate, (c) DC sputtering of Pt IDT electrodes deposited on top of the alumina substrate, (d) RF sputtering of ZnO thin film layer deposited on top of the electrodes, (e) thermal treatment at 800 °C and (f) femtosecond laser processing.

The laser system used to generate the LIPSS on the ZnO surface was a Ti:Sapphire mode-locked oscillator with a regenerative amplifier able to generate 130 fs pulses at a central wavelength of 800 nm with a 1 kHz repetition rate. The specific set-up is shown in Fig. 4.2. The laser spot was focused on the ZnO samples utilizing a broadband 10x microscope objective with a numerical aperture (NA) of 0.16. Then, the spot size on the samples was measured using a 50x microscope objective and a Coherent LaserCam HR-UV, yielding approximately a focused spot diameter (ω_0) of 6 μm at 800 nm. Also, in the experiments of this work, the focusing point was displaced certain distances yielding to different values of the spot diameter (ω_z) and consequently machined line width [169].

In order to obtain the optimum laser parameters for LIPSS fabrication, different values of laser scanning velocity, pulse energy and spot diameter were tested. The scanning velocity tested were 5 μm/s, 10 μm/s, 20 μm/s and 50 μm/s, the pulse energies tested were 0.1 μJ, 0.5 μJ and 1 μJ and the spot diameters were varied from 6 μm up to 40 μm by displacing the focusing point. These parameter combinations lead to the fabrication of LIPSS with different morphologies that were characterized via FEG-SEM. Among all of them, using a pulse energy of 0.5 μJ, scanning speed of 10 μm/s and the laser beam focused to a ω_0 of 7 μm approximately, allowed us to fabricate the LIPSS nanopatterns with higher homogeneity and definition.
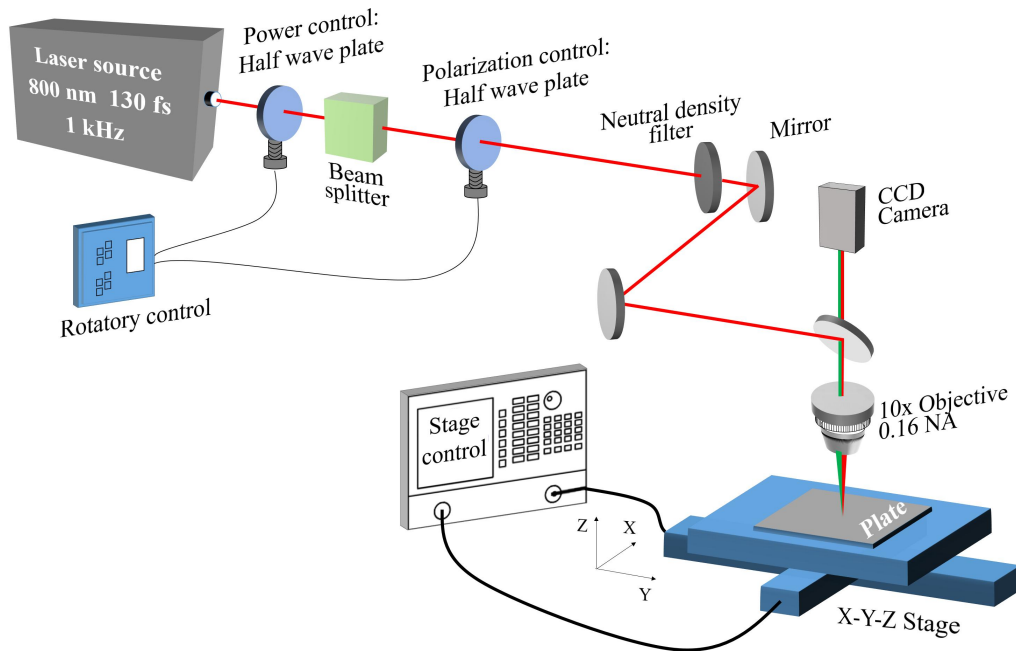
Figure 4.2 – Schematic layout of the femtosecond laser machining set-up for processing ZnO thin film at 800 nm.

On the ZnO surface, two consecutive lines of LIPSS 900 μm long and separated 8 μm were written between each IDT electrode as indicated in red in Fig. 4.3. The femtosecond laser processed only regions of ZnO thin film deposited directly over the alumina substrate and not over the Pt IDT in order to avoid alteration of the Pt/ZnO interface.

4.1.2   Film characterization

For the ZnO film characterization, samples with a size of 6 x 7 mm^2 were fabricated following the same sputtering and annealing recipe as in 3.1.1. Afterwards, several lines of LIPSS were generated, as explained in the previous section.

As in the previous chapter, an average ZnO film thickness of 179.5 nm is considered.

To study the surface topography a JPK Nanowizard 3 AFM was used. Tapping Mode images were obtained using silicon Tap300-G cantilevers with a resonance frequency around 300 kHz. The tip radius is smaller than 10 nm and the half-cone angle is around 25 °.

A SEM Quanta 3D FEG system supplied by FEI Company was used to study the LIPSS morphology surface and in depth. The LIPSS periods were analysed using the two dimensional Fast Fourier Transforms (2D-FFT) of the FEG-SEM surface images.

Raman spectra were collected under ambient conditions using Horiba Jobin Yvon LabRAM HR 800 spectrometer equipped with a fiber coupled 532 nm laser. Spectra acquisition was carried out for 300 s using a x100 objective lens and 1800 gr/mm grating.
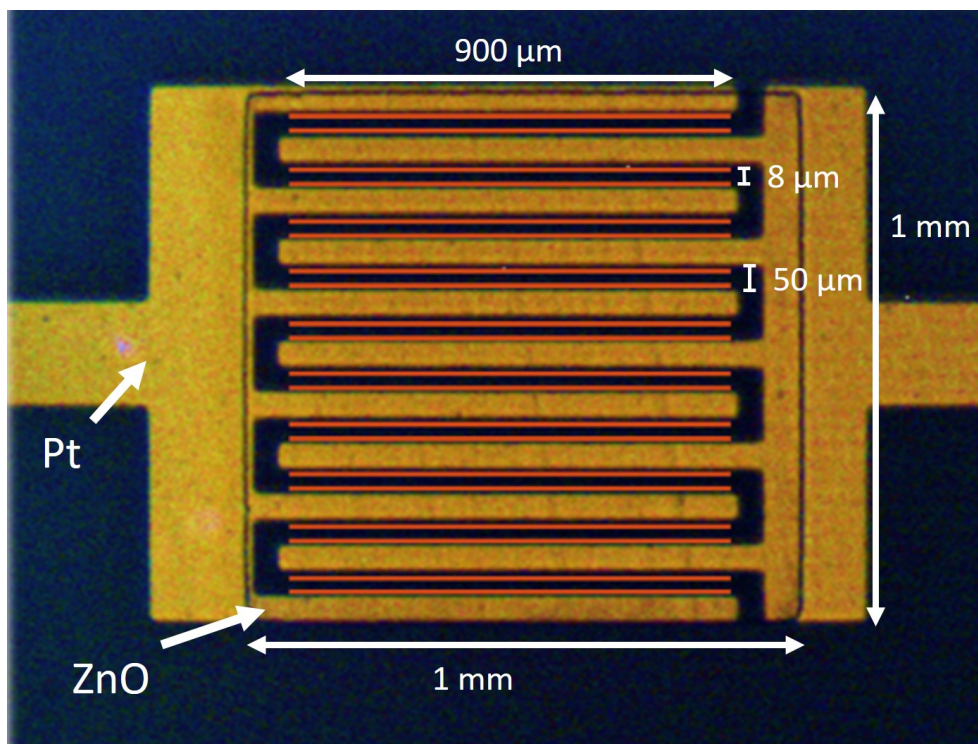
Figure 4.3 – Optical image of the IDT Pt electrodes with the ZnO thin film on top. The dimensions of the LIPSS lines are not to scale with the rest of the image.

During the measurement, the resulting laser power at the surface of the sample was adjusted to 4 mW.

4.1.3   Electrical characterization

The gas measurements were performed inside a cylindrical sealed stainless steel chamber with a volume of 0.97 l (see Fig. 4.4). The NO_2, CO, benzene (C_6H_6), vinyl chloride (C_2H_3Cl) and chlorine (Cl_2) gases were taken from certified bottles mixed with synthetic air (Air Liquide) in concentrations of 50, 100, 20, 10 and 15 ppm, respectively. In all the experiments, a total flux of 400 sccm was used. The data acquisition and the atmosphere control inside the chamber was performed using the same set-up explained in chapter 3.

The response of the sensors (SR_x, where x is the name of the gas) was calculated using the following definitions:

$$SR_x = G_{air}/G_{gas} \tag{4.1}$$

$$SR_x = G_{gas}/G_{air} \tag{4.2}$$

for oxidizing and reducing agents respectively, where G_{air} is the conductivity of the sensor in air, and G_{gas} represents the sensor conductivity after 30 min of gas exposure.
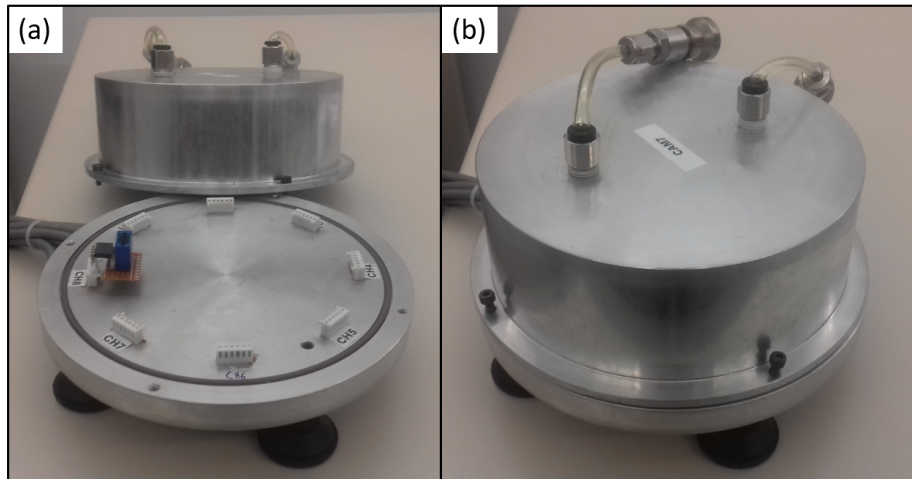
Figure 4.4 – (a) Open and (b) hermetically sealed stainless steel chamber.

4.2 Results and discussion

4.2.1 LIPSS nanostructuring characterization

From AFM and SEM images, a periodic structure can be observed in Fig. 4.5 (b) and 4.6. The average period of the LIPSS nanostructures, Λ, extracted from the 2D-FFT is 145 nm and the average width of the processed lines is around 7 μm (Fig. 4.6). From the profiles of some AFM images (Fig. 4.5 (d)) a LIPSS depth around 70-80 nm is observed, while the average depth in the SEM cross-section of the LIPSS is 140 nm. This mismatching between both measurements could be because the tip of the cantilever has a radius of curvature (r < 10 nm) and pyramidal shape, being unable to reach the bottom of the ZnO surface, implying an underestimation of the LIPSS height.

Taking into account the length and the approximate width of the lines generated with LIPSS, a 12.5% of the total ZnO thin film surface was processed.

The granular morphology is preserved under the LIPSS as can be appreciated in Fig. 4.5 (a) and (b) (it is worth noticing that the AFM scanned areas have different size in each image).

In the specific case of ZnO nanostructuring via LIPSS, the existence of HSFL and LSFL has been thoroughly analysed by Pin Feng et al. [170]. In the present work, the generation of HSFL with a periodicity of approximately 145 nm has been shown. This result is in agreement also with the observations of X. D. Guo et al. [171, 172] and M. Zamfirescu [173]. Regarding the established classification of HSFL in the work of J. Bonse [76], we suggest that the fabricated structures consist in type HSFL-1 which are mainly observed in dielectrics and semiconductors with a period smaller than half of the incident laser wavelength and a depth of a few tens of nanometres.

Raman measurements were performed in order to investigate the crystal modifications between only-annealed ZnO thin film and ZnO with LIPSS. As shown in Fig. 4.7, the Raman peaks that are common in both samples (378, 416, 430, 445, 576 and 645 cm^{-1}) are identified with the alumina substrate [174]. From the ZnO, it can be observed that
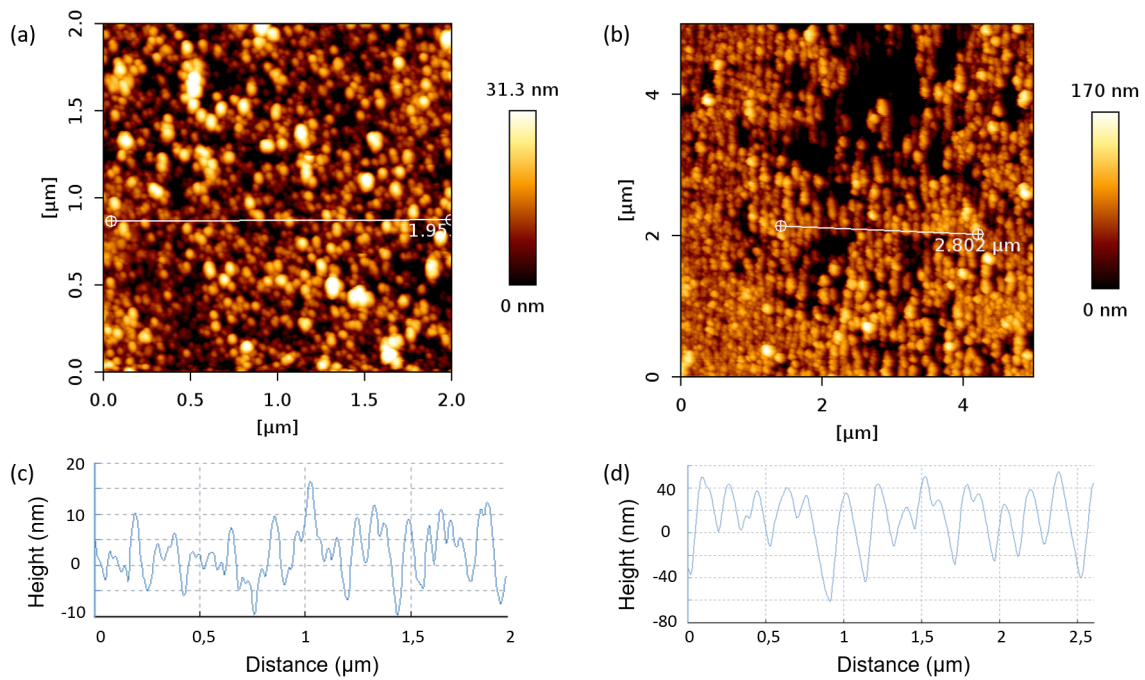
Figure 4.5 – (a) 2 μm^2 AFM tapping mode images of ZnO TT800C on alumina, (b) 5 μm^2 AFM tapping mode images of ZnO TT800C + LIPSS on alumina, (c) section profile of the ZnO TT800C grains and (d) section profile of the LIPSS.

the peak around 436 cm^{-1} vanishes for the ZnO with LIPSS. This peak is identified with the optical phonon E$_2$ mode and attributed to the wurtzite crystal structure of ZnO [175], indicating that in the LIPSS samples the wurtzite structure quality diminishes. This effect also matches the results shown by the team of X. D. Guo [171], where ZnO nanostructures have been processed with a similar set-up.

The sharp peak present in both samples at 576 cm^{-1} is related to a Raman mode of the alumina substrate, as mentioned before. However, there exists another very broad peak on the ZnO with LIPSS, between 518 cm^{-1} and 594 cm^{-1}, approximately (highlighted in blue square in Fig. 4.7). A similar wide peak is shown in the Raman spectra of the LIPSS nanostructures generated by X. D. Guo with a maximum around 570 cm^{-1} and they attribute it to ZnO A$_1$(LO) phonon mode, related to the defects of the nanostructures due to the laser irradiation. Nevertheless, in the work done by G. J. Exarhos [175] on ZnO films it is proposed that a peak around 579 cm^{-1}, identified with the E$_1$(LO) mode, could be related to defect electronic states within the band gap due to an excess of Zn content in the film. In the work of K. Saw [164], where characterization of ZnO thin films is carried out, the same peak appears wider (from 530 cm^{-1} to 620 cm^{-1}) and is also identified with the same kind of defects and contrasted with X-ray Photoelectron Spectroscopy (XPS) analysis. Besides, in the characterization of ZnO multi-layer nanosheets [176] a peak at 560 cm^{-1} is related to Zn existence due to incomplete oxidation.

In particular, in the work performed by P. Xiong [177], where 2D nanostructures on the surfaces of the ZnO crystal are generated by the interference of three femtosecond laser beams, a Raman peak at 572 cm^{-1} is attributed to A$_1$(LO) phonon. Besides, in the
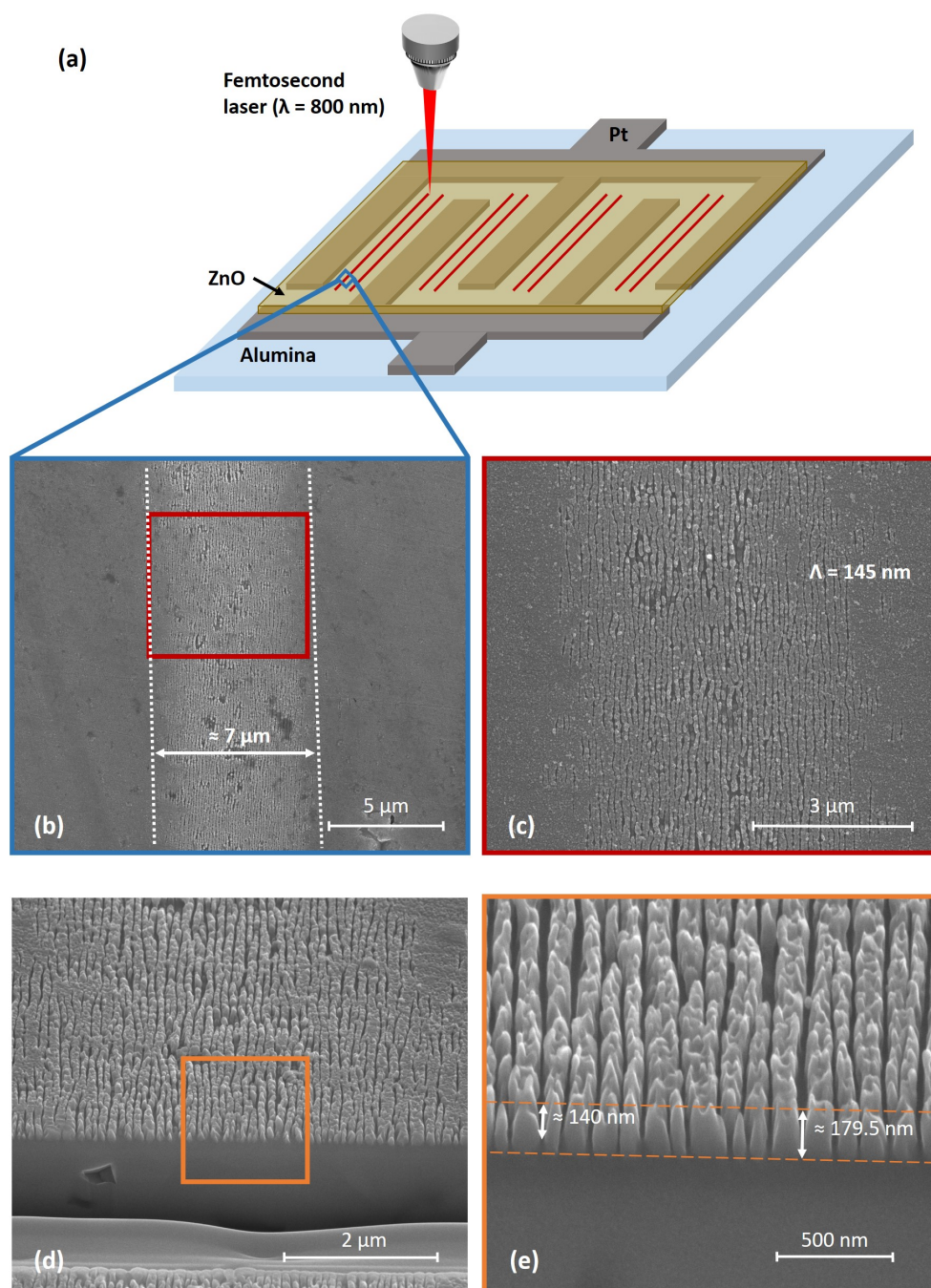
Figure 4.6 – (a) Schematic drawing of the Pt IDT electrodes with the ZnO thin film on top. The red lines represent the LIPSS structures. (b) SEM image of one LIPSS line, (c) zoomed image of (b), (d) SEM image of a cross-section of the ZnO LIPSS processed by femtosecond laser and (e) zoomed image of (d).

same samples, an enhancement of the UV emission is related to the formation of surface defect states of Zn interstitials. Therefore, it can be concluded that the wide peak that appears on the Raman spectra of the LIPSS nanostructures is related to defects, possibly related to Zn interstitials.
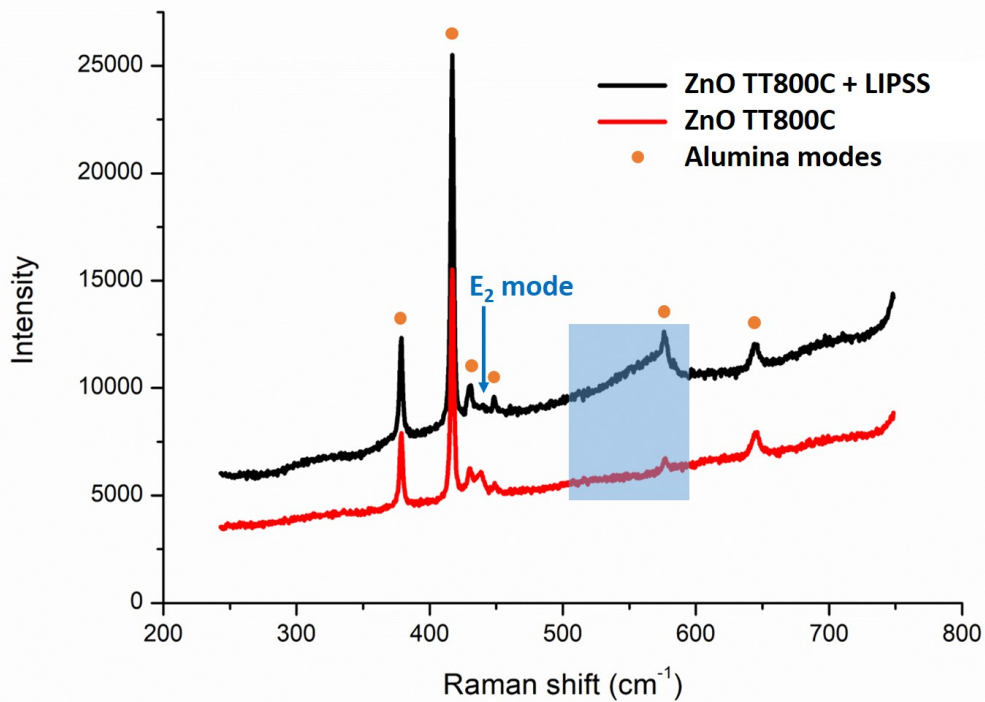
Figure 4.7 – Raman spectra of ZnO thin film annealed at 800 °C compared with ZnO thin film annealed at the same temperature with LIPSS.

4.2.2 Gas sensing results

The detection principle of chemical gas sensors is based on the rise or decrease of the sensing material conductivity when it is exposed to reducing or oxidizing atmospheres. The sensing material needs to be heated up to temperatures around 200 °C-400 °C, where oxygen in the form of negatively charged species adsorbs on the surface of the semiconductor.

To demonstrate the sensing properties of the LIPSS generated on the ZnO thin film, sensor devices with and without LIPSS were measured at a typical detection temperature (325 °C) under 5 ppm of NO_2, 50 ppm of CO, 5 ppm of C_6H_6, 10 ppm of C_2H_3Cl and 1 ppm Cl_2 mixed with air. Preliminary results showed that the only oxidizing gas tested, NO_2, presents the highest response for both type of sensors. In Table 4.1, the ratio $\frac{SR_x-1}{SR_{NO_2}-1} \cdot 100$ has been calculated to show the selectivity of the sensors towards NO_2. The -1 subtraction of the defined response and the later multiplication by 100 was done to obtain ratios between the values 0 and 100, so a number close to 0 means good selectivity to NO_2 with respect to gas x. As a result, good selectivity to NO_2 has been obtained, especially for TT800C + LIPSS sensors.

Therefore, a deep study has been carried out with NO_2. In Fig. 4.8, the response of both type of sensors at different temperatures are shown for 2 ppm of NO_2. As can be appreciated, the sensors with LIPSS present responses much higher than non-processed ZnO thin film, although the error bars are slightly bigger for all the temperatures in the case of the sensor processed by the femtosecond laser. All the error bars are calculated

	$\frac{SR_{NO_2}-1}{SR_{NO_2}-1} \cdot 100$	$\frac{SR_{CO}-1}{SR_{NO_2}-1} \cdot 100$	$\frac{SR_{C_6H_6}-1}{SR_{NO_2}-1} \cdot 100$	$\frac{SR_{C_2H_3Cl}-1}{SR_{NO_2}-1} \cdot 100$	$\frac{SR_{Cl_2}-1}{SR_{NO_2}-1} \cdot 100$
TT800C + LIPSS	100	3.9	5.0	5.0	5.6
TT800C	100	3.9	15.8	10.5	9.2

Table 4.1 – $\frac{SR_x-1}{SR_{NO_2}-1} \cdot 100$ ratios for each type of sensor.

using four different measurements. Taking into account the abrupt increase in response around 350 °C, this temperature has been considered the optimal temperature.
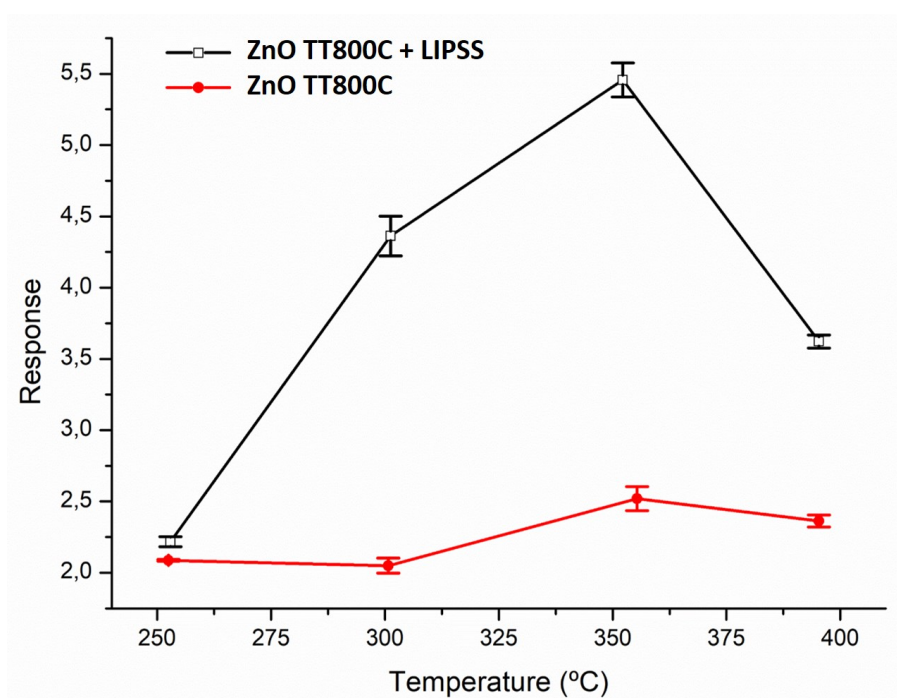
Figure 4.8 – Response (SR_{NO_2}) of the ZnO sensors with LIPSS and without as a function of temperature for 2 ppm of NO_2.

Afterwards, at the optimal temperature, the sensors were exposed to different concentrations in order to study the sensitivity of the devices (Fig. 4.9). For all tested concentrations (5, 2 and 1 ppm) of NO_2, the sensor processed with LIPSS presents a higher response than the ZnO thin film. In addition, repeatability of the response under 2 ppm is tested, showing the same response at non-consecutive pulses. In Fig. 4.9 (b), a linear sensitivity is shown for both sensors for concentrations between 5 and 1 ppm of NO_2, so it can be calculated from the slope of the straight line. The sensitivities are 1.71 and 0.76 ppm^{-1} for the sensor with LIPSS and without them, respectively. The detection limit (LOD) has been calculated using the following formula: LOD = $3\sigma/b$, where σ is the standard deviation of the baseline during 5 min and b is the calculated sensitivity. For the sensor without LIPSS the LOD is already good: 3 ppb, but for the sensor with LIPSS, the theoretical LOD goes down to 1 ppb, showing up the possibility to use it in hazardous environments.
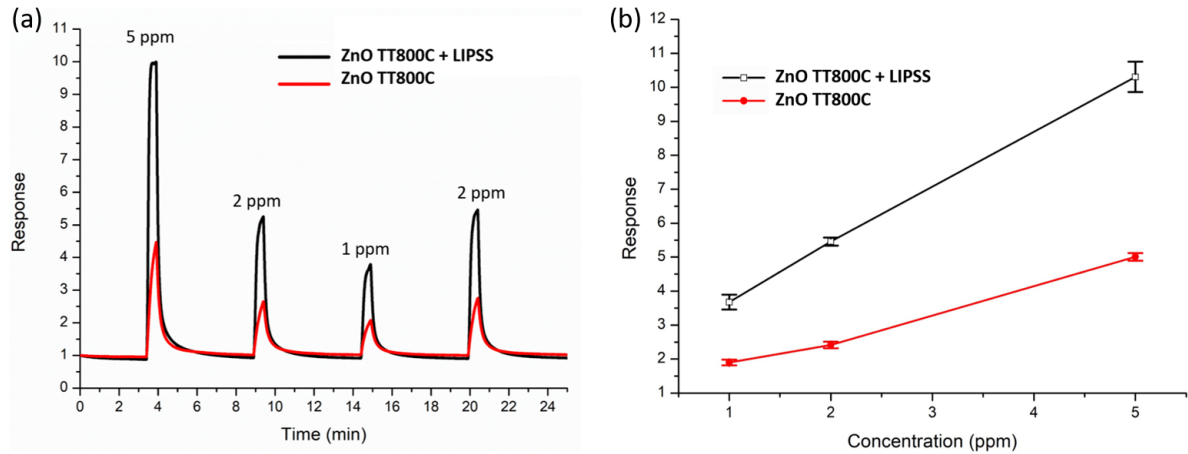
Figure 4.9 – (a) Response (SR_{NO_2}) of the ZnO sensors with LIPSS and without at the optimal temperature ($T_{opt.} \simeq 350$ °C) for 5, 2, 1 and 2 ppm of NO_2. (b) Sensitivity of the two sensors at the optimal temperature.

In order to study the repeatability of the sensors, pulses of 2 ppm of NO_2 during 30 min have been carried out every week, during 4 weeks in a row. After a month and a half with the sensors kept in the chamber open to ambient air and at the optimal temperature, the same experiment was performed and results are shown in Fig. 4.10. Both kind of sensors present a repeatable behaviour over all the tested period, with a repeatability standard deviation (S_r) of 0.21 and 0.19 for the sensor with LIPSS and without, respectively. The consequent repeatability values (r = 2.3 x S_r) are 0.48 and 0.44, respectively.

During all the gas measurements performed at the optimal temperature, the resistance baseline in the presence of air of the two type of sensors varied in the range of 20 kΩ - 80 kΩ and 3 kΩ - 18 kΩ for the sensor processed with LIPSS and for the only-annealed sensors, respectively.

The detection mechanism exposed in the previous chapter can also be assumed for the devices presented here, since both are ZnO based sensors. Besides, as explained in chapter 2, defects detected by PL in ZnO nanoparticles have been identified to contribute to the NO_2 detection mechanism [131] and the group of M. Chen highlighted the effect of donor defects as well as surface oxygen species [42, 125] through in-situ DRIFTS technique. As a result, it is proposed that the increase in response of the ZnO sensor devices with LIPSS nanostructures on it, compared with only-annealed ZnO thin film, could be a consequence of the increase of the Zn interstitials defects on the ZnO surface, as Raman measurements suggest. As explained, the sensor processed with LIPSS present always a higher resistance than the only-annealed sensor, what bears out the presence of more Zn interstitials. Therefore, with more donor defects, more electrons will be transferred from the crystal to NO_2 molecules, improving the sensitivity.
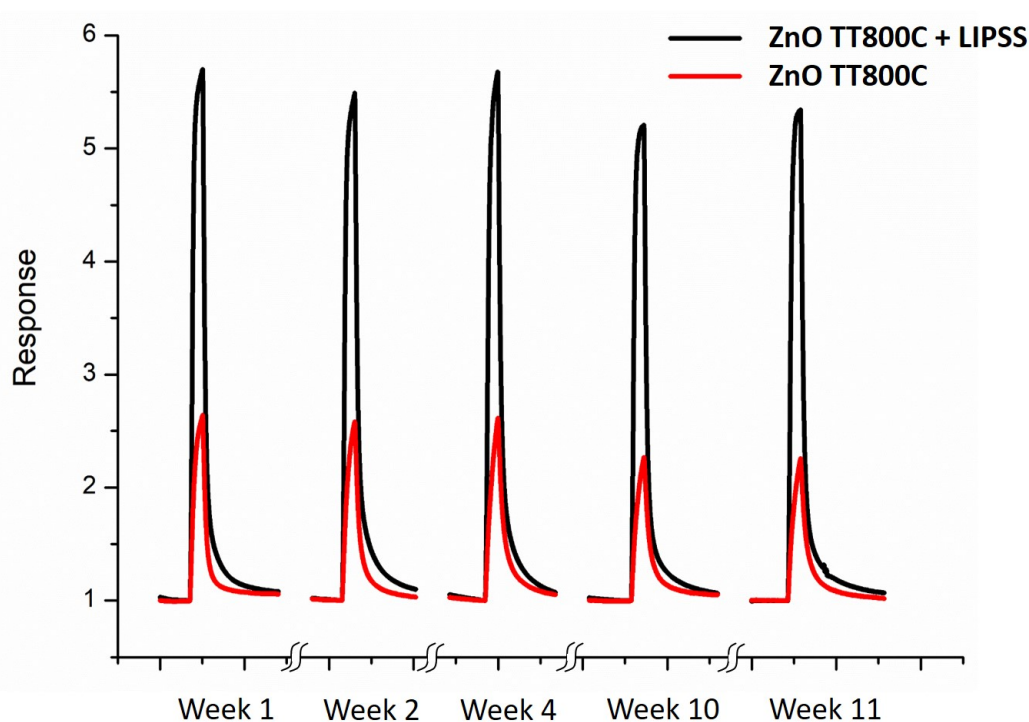
Figure 4.10 – Repeatability of the responses (SR_{NO_2}) of both sensors under exposure of 2 ppm of NO_2 measured during several weeks in a row.

4.3   Conclusions

Generating LIPSS with a femtosecond laser on the ZnO surface is an innovative technique able to modify the surface morphology and the defects at the material surface. This can be used as an advantage to improve the sensitivity of conductometric gas sensing devices.

In this work, ZnO HSFL nanostructures have been processed on sensor devices and tested under NO_2 atmospheres. With only a 12.5% of the total ZnO area processed with LIPSS, an increase of the sensor response of 50% (for 2 ppm of NO_2 at 350 °C) is found in comparison with the only-annealed ZnO thin film sensor. The LOD downs to 1 ppb for the processed sensor, 3 times higher than for the sensor without LIPSS. With a femtosecond laser with a repetition rate of 1 MHz, instead of 1 kHz, an area of 20.000 μm^2 could be processed in 0.28 s instead of 4.76 min, what could be scalable to mass production.

Raman characterization reveals a decrease of the ZnO wurtzite structure for LIPSS, with an increase of surface defects such as Zn interstitials. Donor defects contribute on the NO_2 detection mechanism, releasing electrons to the oxidizing pollutants and consequently increasing the sensitivity. Consequently, Zn interstitials are proposed as the cause of the response enhancement for the tested NO_2 concentrations.

Chapter 5

WO$_3$ based sensors nanostructured by direct laser interference patterning

In this chapter, two kind of sensors based on sputtered WO$_3$ annealed at 600 °C are studied. The first type are processed by two-beam DLIP set-up (with 500 nm of period) and the second one does not receive any additional treatment. The structural properties of the films are characterized by surface and bulk techniques in order to investigate the laser effect on the devices. Besides, NO$_2$ selectivity and sensitivity are studied and the sensing mechanisms discussed.

5.1 Experimental

5.1.1 Sensor fabrication

The fabrication steps of the WO$_3$ based sensors are summarized in Fig. 5.1. They were fabricated on 1 x 2 cm^2 polished alumina substrates (Fig. 5.1 (a)). First, a Pt heating resistor was deposited on the reverse side of the alumina substrate, shaped by photolithography and grown by DC sputtering in an Edwards ESM 100 system (Fig. 5.1 (b)). The same fabrication steps were used to grow Pt IDT electrodes for the electrical measurements (Fig. 5.1 (c)). The shape, dimensions and sputter recipe of the heater and the IDT electrodes are the same as in the last chapters. Afterwards, 1 mm^2 WO$_3$ sensing layer was deposited on top of the Pt electrodes by photolithography followed by RF reactive magnetron sputtering with a metal oxide target of 99.99 % purity. The sputtering process was performed in a Pfeiffer-Iontech system at 300 W of RF power in a mixed atmosphere of oxygen (40 %) and argon (60 %) and under $5 \cdot 10^3$ mbar of pressure. The sputtering time was 1 h, the deposition temperature was between 25 °C and 30 °C and as for the Pt, acetone was used for the lift-off process (Fig. 5.1 (d)). Finally, the sensor device was thermally stabilized in a quartz oven at 600° C during 4 h in synthetic air (Fig. 5.1 (e)). The only-annealed samples will be labelled TT600C. The annealing temperature was chosen considering previous results obtained by our research group [25].
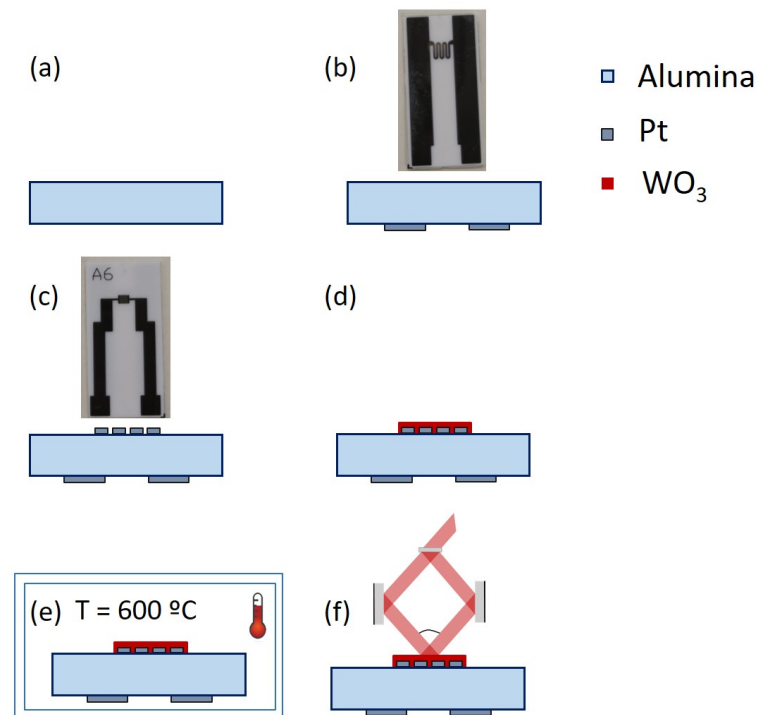
Figure 5.1 – Schema of the fabrication steps of the WO$_3$ sensor device. (a) Polished alumina substrate, (b) DC sputtering Pt heating resistor on the reverse side, (c) DC sputtering IDT electrodes, (d) RF sputtering of WO$_3$ sensing layer, (e) annealing at 600 °C and (f) DLIP processing at 50 mJ/cm^2.

After annealing, some sensors were processed by the same two-beam DLIP set-up as in chapter 3 (see Fig. 5.1 (f)). A detailed schematic drawing of the set-up is shown in Fig. 5.2: an optical beam splitter divides the laser source into two different beams; afterwards they are reflected in mirrors and finally addressed towards the sample surface with the same incident angle. The maximum and minimum of interference are indicated with a sinusoidal wave and the heat flux flowing generated by the laser is indicated with red arrows.

An angle of 41.5° was set-up to fabricate lines with a theoretical period of 500 nm. The necessary fluence to obtain 1D interference patterns on the surface of WO$_3$ thin film annealed at 600 °C was found to be optimum for a value of 50 mJ/cm^2 with a single shot. AFM images did not present any morphological modification on samples processed at lower fluences than 50 mJ/cm^2. The maximum and minimum of interference pattern are perpendicular to the IDT electrodes, as in chapter 3. The DLIP-processed samples will be labelled TT600C + DLIP50.

5.1.2   Film characterization

For the WO$_3$ film characterization, samples with a size of 6 x 7 mm^2 have been fabricated by sputtering and annealed at 600° C following the same recipe as in previous section. Some samples have also been processed by DLIP, as explained in the sensor
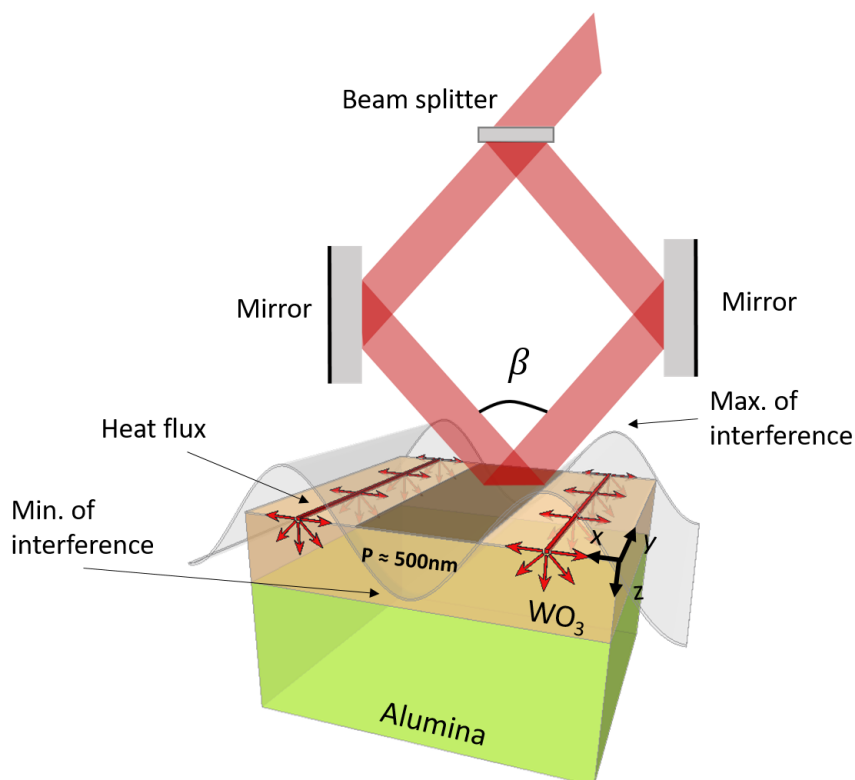
Figure 5.2 – Schematic two-beam DLIP set-up processing WO$_3$ thin film on alumina.

fabrication section.

The film thickness was determined by a KLA Tencor profilometer, resulting in an average thickness of 145 nm.

For morphological characterization, JPK Nanowizard 3 AFM was used. Tapping mode images were obtained using silicon Tap300-G cantilevers with a resonance frequency around 300 kHz. The tip radius is smaller than 10 nm and the half-cone angle is around 25 °.

A SEM Quanta 3D FEG from FEI Company was used to study the homogeneity of the DLIP process in the sample as well as for a cross-section analysis.

The X-ray diffraction analysis was performed by a Bruker D8 Advance diffractometer in grazing incident configuration (1.8 ° incident angle). The diffractometer was equipped with a copper X-ray tube operating at 40 kV and 40 mA, and with a LYNXEYE XE detector. Samples were placed on a quartz zero-background holder. Measuring conditions were 5° to 80° 2θ-range, 0.02 2θ-scan rate, and 0.8 seconds per step of counting time. The mean crystallite size, the strain of the crystallites and the cell parameters were determined by whole profile fitting Powley and Le Bail methods [178, 179] as implemented in the TOPAS v 4 program by Bruker AXS [180]. The fundamental parameters approach was used for the line-profile fitting [181–183]. In this approach, the instrumental component of peak broadening is calculated by the convolution of instrument profile functions for optics and X-ray tube emission. Thus, the sample components to peak broadening (crystallite size and strain) are the only peak shape parameters to be optimized in the profile fitting

procedure. In particular, the Double-Voigt method [184] implemented in TOPAS allowed to calculate the crystallite size and strain as volume-weighted for the mean column heights based on the sample-dependent integral breadths of peaks.

Raman spectra were collected under ambient conditions using Horiba Jobin Yvon LabRAM HR 800 spectrometer equipped with a fiber coupled 532 nm laser. Spectra acquisition was carried out using a x100 objective lens and 1800 gr/mm grating. During the measurement, the resulting laser power at the surface of the sample was adjusted to 4 mW. Exposure time ranged from 100 to 200 seconds.

The composition depth profile of different ions was measured using a TOF-SIMS 5, ION TOF. The mass spectrum was obtained by measuring the time-of-flight distribution of the positive ions coming from the sample surface into the detector. The primary ions source was Bi$^+$ operating at 25 keV and the spot size for the depth profile was 50 μm x 50 μm. Sputtering was done using 1 keV oxygen beam over a 300 μm x 300 μm of raster size area.

5.1.3   Electrical characterization

The gas tests were carried out inside a cylindrical aluminium chamber with a volume of 0.6 l (see Fig. 5.3). At the center of the chamber, there was a gas diffuser, so the gas was uniformly distributed and all the sensors receive it at the same time. The atmosphere inside the chamber was controlled by means of MFCs. The NO$_2$, CO and formaldehyde (HCHO) gases were taken from certified bottles mixed with synthetic air (Air Liquide) of 100 ppm, 100 ppm and 20 ppm, respectively. In all the experiments a total flux of 500 sccm was used. These experiments were performed at the "Sensor Laboratory" at the University of Ferrara.
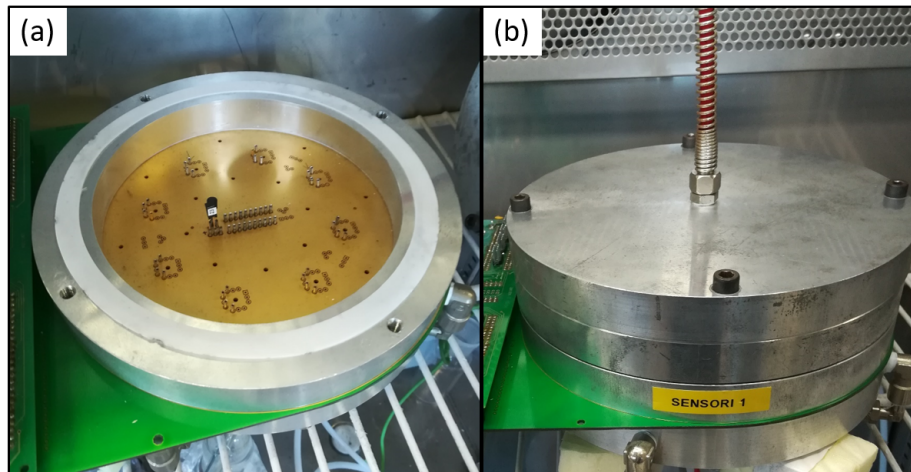
Figure 5.3 – (a) Open and (b) hermetically sealed aluminium chamber.

The circuit used to measure the sensors conductance in the presence of gas includes an inverting operational amplifier (OA) as it is shown in Fig. 5.4. R$_s$ and R$_f$ are the sensor and the reference resistance, respectively. R$_f$ can be freely modified and must be in the same order of magnitude as R$_s$. As V$_{in}$ and R$_f$ are known and constant, the

output voltage, V_{out}, is proportional to the conductance of the sensor, G, as indicated in equation 5.1:

$$V_{out} = -\frac{R_f}{R_s} \cdot V_{in} = const. \cdot G \qquad (5.1)$$
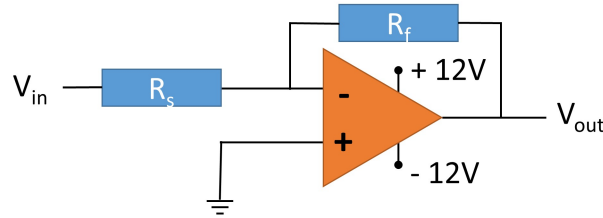
Figure 5.4 – Electrical circuit used to measure the sensor conductance.

The output voltage is measured through a Keithley 2000 Multimeter connected via GPIB to the computer, where a Labview© software is acquiring the data.

The response of the devices, SR, is defined as equation 5.2:

$$SR = G_{air}/G_{gas} \qquad (5.2)$$

where G_{air} is the conductance of the sensor in air (baseline), and G_{gas} represents the sensor conductance after 30 min of gas exposure.

In order to characterize the conductivity of the sensors at different temperatures, a smaller chamber was used (10.8 ml of volume), shown in Fig. 5.5, and the steps below were followed:

(i) In 400 sccm of air, the sensor was heated to 450 °C in less than 30 min and left at that temperature for 10 min.

(ii) The sensor was cooled down to $\sim$ 100 °C and after a minute, the temperature was increased up to $\sim$ 500 °C with steps of $\sim$ 5 °C/min, while the conductivity was measured.

(iii) The same procedure was performed in 5 ppm of NO_2.

5.2 Results and discussion

5.2.1 Morphological and structural characterization

The AFM image of Fig. 5.6 (a) shows a flat surface for the WO_3 sample annealed at 600 °C with a root-mean-square (RMS) roughness of 7 nm, while for the DLIP-processed sample (Fig. 5.6 (b) and (d)) a hole structure appears in a periodic line-pattern. The RMS roughness, as the average between the processed and non-processed regions, has increased to values between 10 and 15 nm. The profile section of the DLIP-processed

Figure 5.5 – Chamber used to measure the variation in conductivity as a function of the temperature.

sample measured from the AFM images (Fig. 5.6 (c)) indicates that the average depth of the holes is 18 nm. Nevertheless, from the cross-section images performed by FIB (Fig. 5.7), the hole structure seems to be reaching the substrate, so probably the profile sections of Fig. 5.6 (c) are underestimating the depth due to the high half-cone angle of the tip.

The line-patterned morphology indicates that the hole area corresponds to the places where higher intensity has been accumulated and consequently a higher temperature has been reached, melting material. Precisely, the highest area around the holes (Fig. 5.6 (d)) seems to be the melted WO$_3$ moved from inside the cavities, as explained by the Marangoni convection mechanism [151].

From the SEM images (see Fig. 5.8), a bigger area of the nanostructured sample can be analysed, showing a great homogeneity of the nanostructuring with the desired period.

As the IDT electrodes were deposited beneath the thin film in this chapter, the DLIP process could affect the Pt thin film and the WO$_3$/Pt contact could be damaged. In order to determine if the Pt of the IDT electrodes was processed, AFM images were taken at two different regions of the final processed sensing device (TT600C + DLIP50), as shown in Fig. 5.9.

Fig. 5.9 (b) and (c) display AFM images of DLIP-processed and non-processed Pt thin film over alumina, respectively. Both images present a very similar topography without any stripe pattern, what confirms that the Pt thin film is not affected by the DLIP-processing. This is probably because Pt material presents a higher laser damage threshold than WO$_3$ at 355 nm of wavelength. As an example, in the work performed by R. Catrin [185], 300 nm of Pt on 20 nm of titanium (Ti) are processed with a very similar DLIP set-up (two-beam, $\lambda = 355$ nm and 10 ns of pulse duration) and the laser fluence used to generate stripes (476 mJ/cm^2) is one order of magnitude higher than in this work (50 mJ/cm^2).

As expalined in chapter 2, many polymorphic structures have been identified in WO$_3$ as a function of temperature [112–116]: monoclinic (for temperatures lower than -50 °C and from 17 °C to 330 °C), triclinic (from -50 °C to 17 °C), orthorhombic (from 330 °C to 740 °C) and tetragonal (for temperatures higher than 740 °C). Besides, the sensing performance is affected by the crystal structure [117].
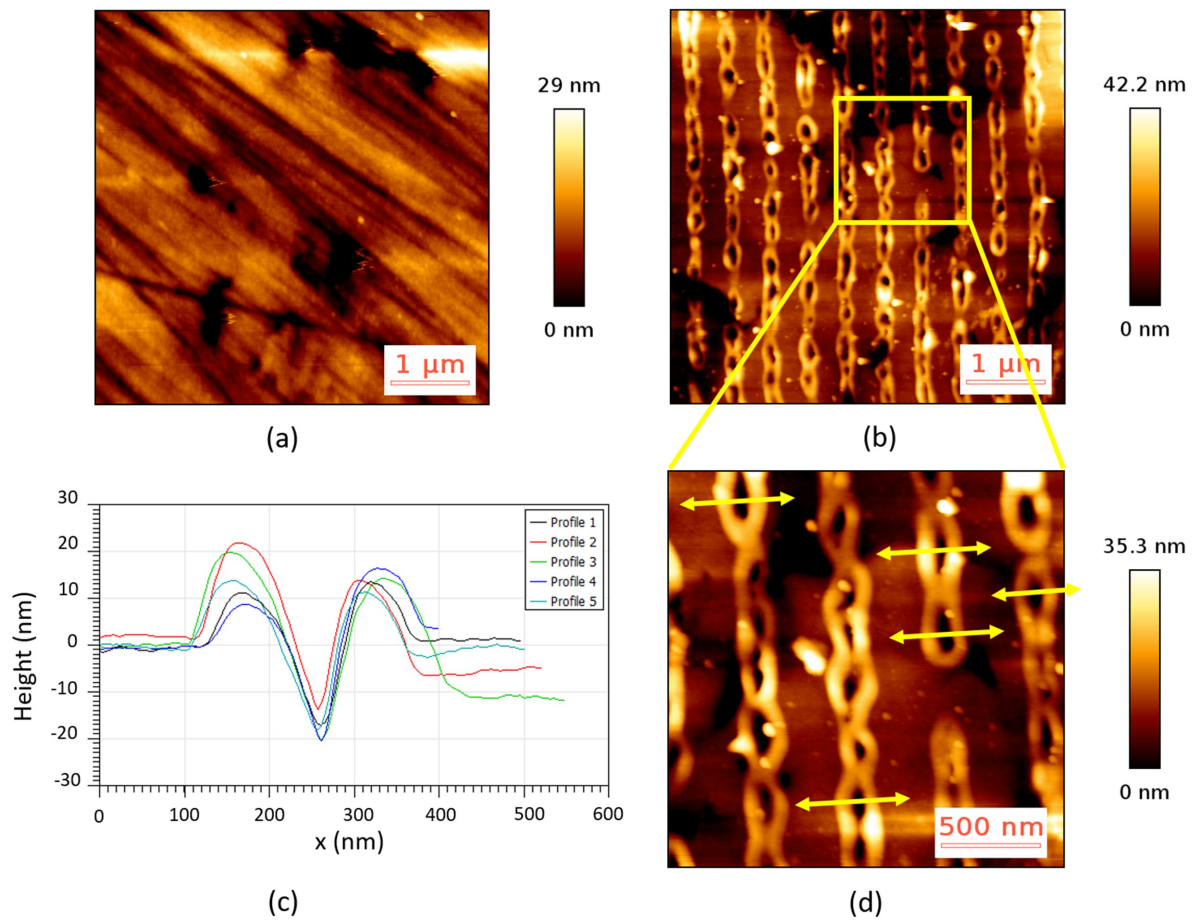
Figure 5.6 – AFM tapping mode images of WO$_3$ thin film (a) only-annealed and (b) DLIP-processed. (c) Profiles of the sections point out in (d); (d) zoomed image of the sample DLIP-processed.
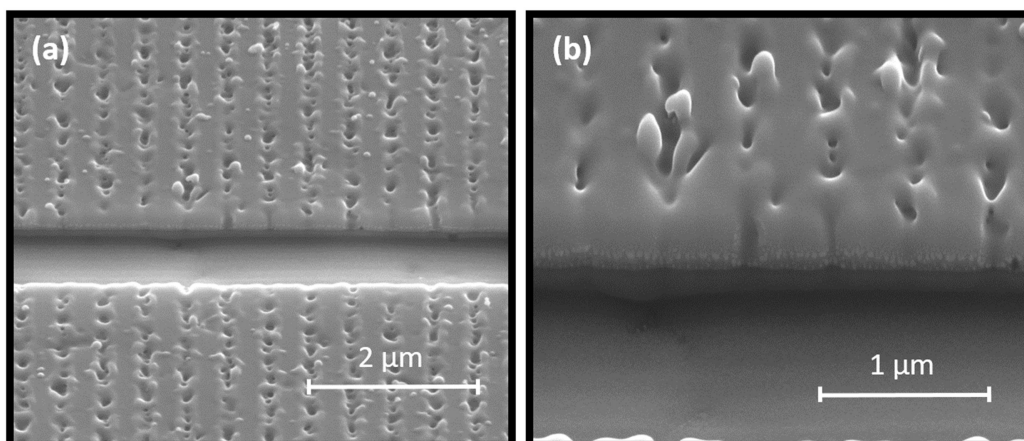
Figure 5.7 – SEM image of a cross-section of the sample DLIP-processed with different magnifications.
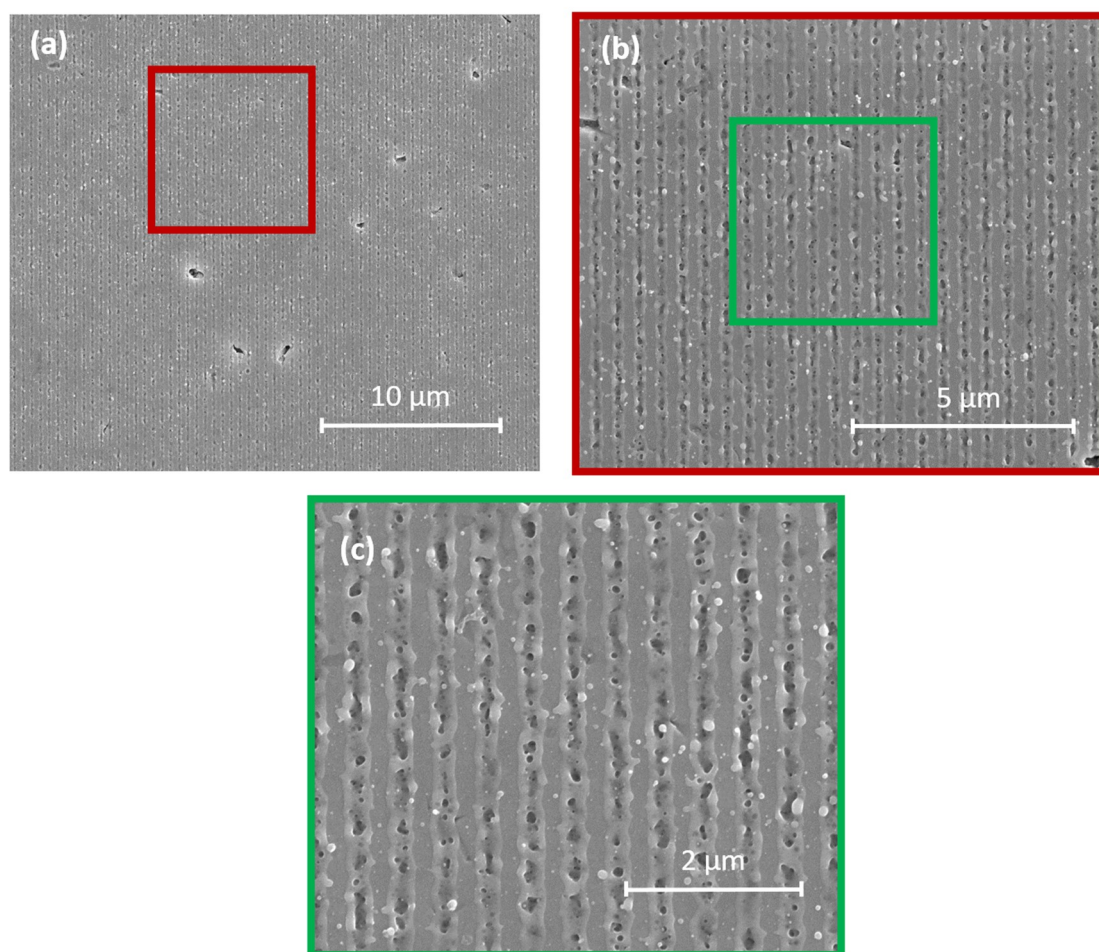
Figure 5.8 – SEM images of WO$_3$ thin film annealed at 600 °C and processed by DLIP at 50 mJ/cm^2 with different magnifications.

The GIXRD patterns of the as-grown, only-annealed (TT600C) and DLIP-processed (TT600C + DLIP50) samples are reported in Fig. 5.10. All patterns show peaks corresponding to the alumina substrate (space group R$\bar{3}$c, PDF 010-0173). The as-grown sample does not show peaks attributable to any WO$_3$ crystal structure, while the only-annealed and DLIP-processed samples show peaks belonging to the tetragonal WO$_3$ structure (space group P4/nmm PDF 018-1417). The relative intensity of the (110) peak does not match the PDF data for powder tetragonal WO$_3$ structure, indicating that in both samples the crystallites grow with significant preferential orientation. This result is in agreement with previous investigations [25] and indicates that the laser modifications does not destabilize the tetragonal crystal structure. The stability of the crystal structure and the crystallite size are important issues for the sensing mechanism [186].

Table 5.1 reports the cell parameters, the mean crystallite size and microstrain of the crystalline samples. Cell parameters and strain that were calculated by Powley and Le Bail methods, are also very similar for the samples treated and not treated with laser. Nevertheless, even if it remains within the error bars, a slight increase of the crystallite size of the DLIP-processed sample compared to only-annealed WO$_3$ is observed.
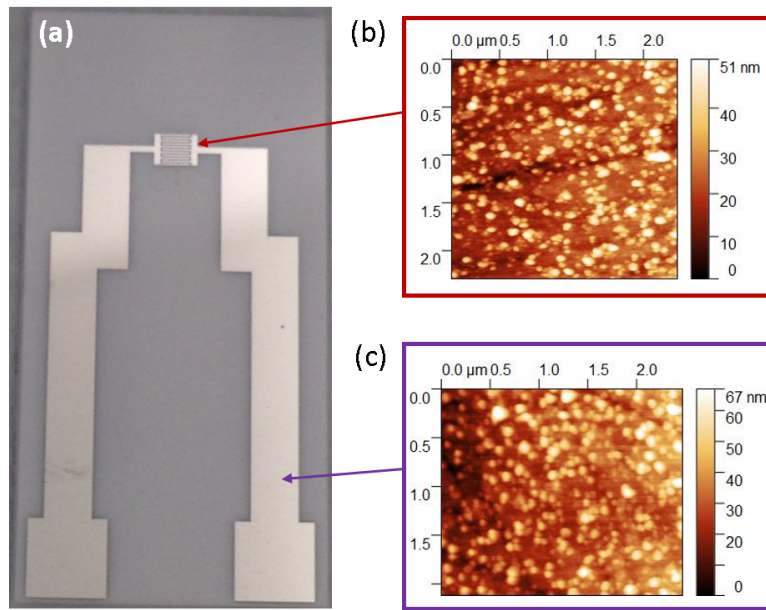
Figure 5.9 – (a) Image of Pt IDT electrode, (b) DLIP-processed Pt over alumina and (c) non-processed Pt over alumina.

Method	Parameters	WO$_3$ TT600C	WO$_3$ TT600C + DLIP50
Le Bail	a (Å)	5.2288(2)	5.2288(2)
	c (Å)	3.7963(6)	3.7974(8)
	size (nm)	47(3)	51(5)
	strain	0.24(1)	0.24(1)
Powley	a (Å)	5.2286(2)	5.2287(3)
	c (Å)	3.7955(7)	3.7967(9)
	size (nm)	44(3)	49(6)
	strain	0.23(1)	0.23(2)

Table 5.1 – Cell parameters, mean crystallite size and microstrain calculated by Le Bail and Powley methods for the two different samples.

Tetragonal phase of WO$_3$ is expected to appear for temperatures higher than 740 °C in bulk WO$_3$ [116] and the annealing performed in this work is at 600 °C. Nevertheless, in structures with nanometric crystals, as it is the case of the samples here, temperature and pressure of phase transitions can be strongly modified. A downshift in temperature for the tetragonal transition is shown in [187] for crystallite sizes between 16 and 60 nm and the samples analysed here are in this range, as shown in Table 5.1.

Raman spectra (see Fig. 5.11) supports the above considerations. The as-grown samples only show peaks coming from the alumina substrate [174] (highlighted with an
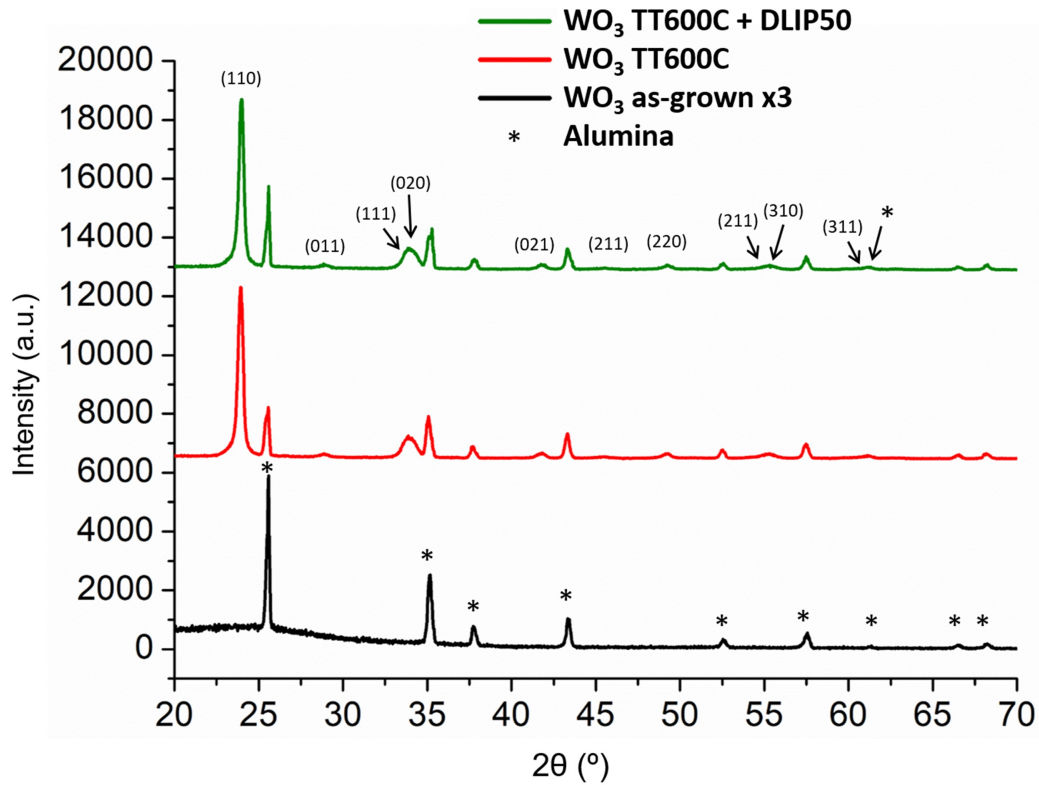
Figure 5.10 – GIXRD measurements of the WO$_3$ thin film as-grown, WO$_3$ only-annealed and WO$_3$ DLIP-processed. All patterns show peaks of the Al$_2$O$_3$ substrates marked with $*$, the other peaks are attributable to WO$_3$ tetragonal phase.

asterisk in Fig. 5.11) while both sample types (only-annealed and DLIP-processed) present the same WO$_3$ Raman modes for the measured spectra.

The peaks coming from the WO$_3$ thin film are found at 267.7, 692.1 and 802.4 cm^{-1}. As it is known, the peaks at low frequencies (200 - 500 cm^{-1}) correspond to bending vibrations, while the high frequency ones that appear at frequencies between 600 and 1000 cm^{-1} are stretching modes [188]. Therefore, the lowest peak can be associated to a bending mode δ(O-W-O) [189] and the peaks in the range of 700 to 800 cm^{-1} are related to stretching modes O-W-O [190] and W^{6+}-O [189], respectively.

5.2.2   TOF-SIMS characterization

Positive TOF-SIMS in depth experiments were performed to analyse the qualitative composition of the samples as a function of thickness. The detected ions related to WO$_3$ were W$^+$, WO$^+$ and WO$_2^+$ and the alumina related ions were Al$^+$ and AlO$^+$.

The measurements were performed twice at different areas of the sample with high repeatability results. In Fig. 5.12, only AlO$^+$ (for alumina) and W$^+$, WO$^+$ and WO$_2^+$ ions (for WO$_3$) of one of the measurement have been plotted, representing the sample behaviour. The signals shown in Fig. 5.12 have been filtered in order to reduce the noise
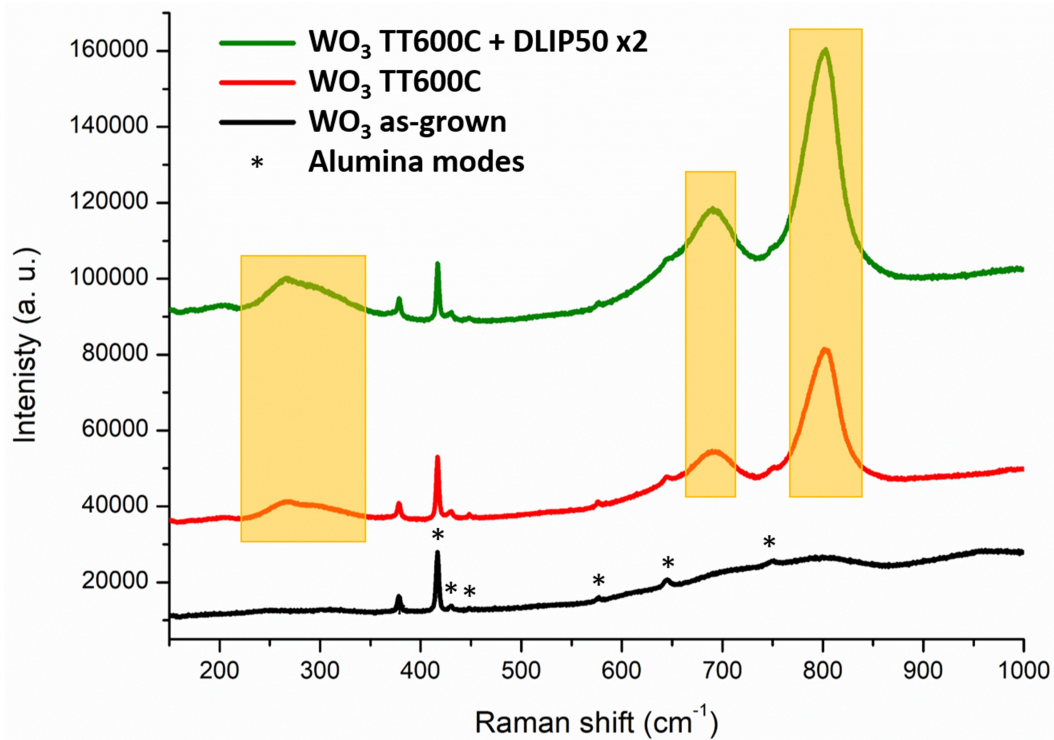
Figure 5.11 – Raman spectra of the WO$_3$ thin film as-grown, WO$_3$ only-annealed and WO$_3$ DLIP-processed.

generated by the equipment. The steep increase in the intensity for the ion WO$_2^+$ in the as-grown sample and the slow decrease of W$^+$ indicate that the sample is more oxidized as deeper points of the WO$_3$ layer are analysed. By contrast, in the other two samples, only a slight increase of the WO$_2^+$ and a decrease of W$^+$ before stabilization are shown. This result means that the first layers of the WO$_3$ are reduced, compared to the rest of the thin film, what could be explained by the existence of oxygen vacancies. As it is known, surface defects promote the gas detection and especially oxygen vacancies have been widely investigated as they increase the adsorption of gas molecules [42, 125, 127, 132, 133]. Moreover, the intensities of WO$^+$ and WO$_2^+$ ions are more parallel for the WO$_3$ DLIP-processed thin film, compared to only-annealed ones (see Fig. 5.12 (b) and (c)). This can be originated by a higher homogeneity degree.

The sputter rate during the TOF-SIMS measurements has been calculated taking into account the WO$_3$ thickness. A small increase of the sputter rate is observed comparing the as-grown with the only-annealed and DLIP-processed sample (see Table 5.2). This could be due to the increase of the homogeneity of the laser-treated sample that raises the sputter velocity. The interface region between the thin film and the alumina is also shown in Table 5.2 and indicated in garnet in Fig. 5.12. As it is expected, the interface region increases significantly with the annealing (62.9 nm) compared to as-grown (39.8 nm), because the atoms receive more energy. Therefore, a slight inter-diffusion can occur at the interface between the WO$_3$ layer and the alumina substrate. In the case of the sample also treated by DLIP, even a larger interface region (75.2 nm) is shown. This is explained by the high temperatures that the sample reaches during the laser shot, as it was shown

(a) WO$_3$ as-grown

(b) WO$_3$ TT600C
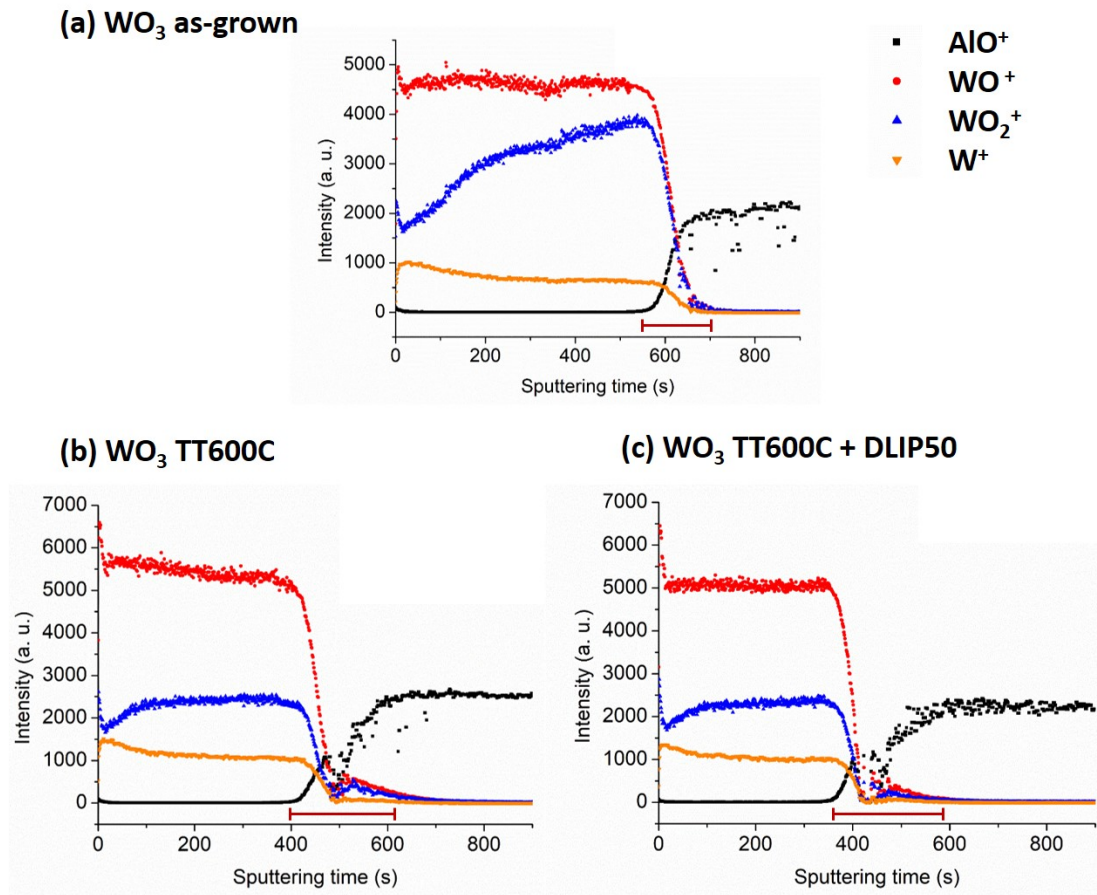
(c) WO$_3$ TT600C + DLIP50

Figure 5.12 – TOF-SIMS measurements of AlO$^+$, WO$^+$ and WO$_2^+$ ions for the samples (a) WO$_3$ as-grown, (b) WO$_3$ only-annealed and (c) WO$_3$ DLIP-processed.

in the chapter 3 for ZnO.

Sample	Sputter rate (nm/s)	Interface region (nm)
As-grown	0.22	39.8
WO$_3$ TT600C	0.27	62.9
WO$_3$ TT600C + DLIP50	0.32	75.2

Table 5.2 – Sputter rate during the TOF-SIMS measurements and interface region between the alumina and the thin film of the WO$_3$ as-grown, WO$_3$ only-annealed and WO$_3$ DLIP-processed.

5.2.3   Gas sensing results

Due to the importance of the working temperature during the gas detection, the response to 5 ppm of NO$_2$ at different stationary temperatures (150 °C - 400 °C) is reported in Fig. 5.13. Two sensors of each type are plotted, showing a good reproducibility

between sensors of the same kind. At temperatures ≥ 250 °C, DLIP-processed sensors respond to NO_2 by decreasing their conductivity but with a very low response, between 1.18 and 1.58. By contrast, sensors only-annealed at 600 °C do not detect NO_2 for these temperatures or increase their conductivity (although the conductivity is increasing, the response is calculated through equation (5.2) because NO_2 is an oxidizing gas). The values of the response for only-annealed sensors at temperatures ≥ 250 °C range from 1.03 to 0.55.
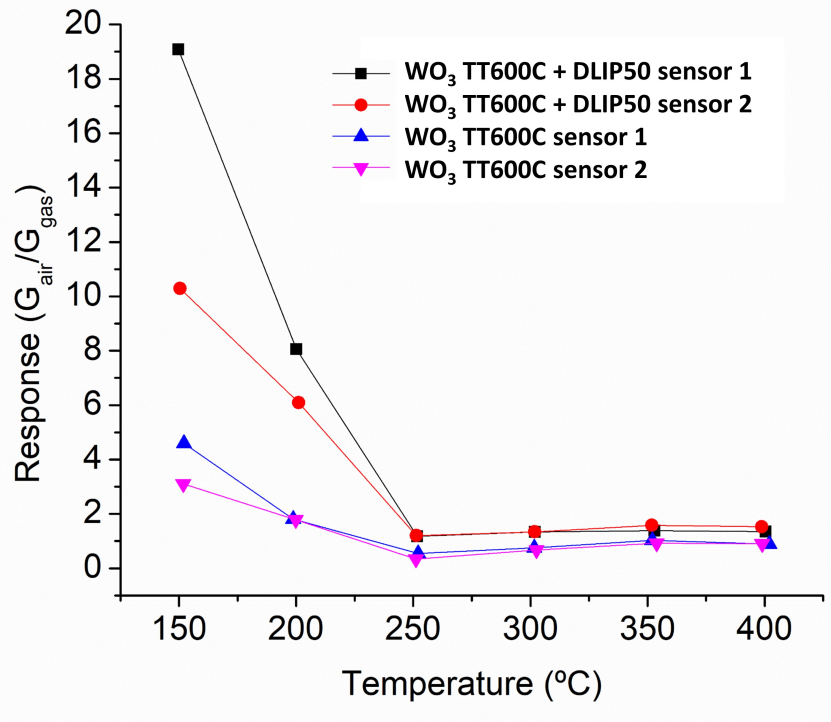
Figure 5.13 – Response as a function of temperature for 5 ppm of NO_2 for two sensors DLIP-processed and two sensors only-annealed.

For temperatures lower than 250 °C, the response of both sensors increases while decreasing the temperature, but DLIP-processed sensors present responses $\simeq 3.5$ times higher than only-annealed sensors. Due to the long recovery time at 150 °C (48 min for only-annealed sensors and 13 min for DLIP-processed sensors), the chosen optimal temperature was 200 °C for both sensors, where the recovery times were decreased to 10 and 7 min approximately for only-annealed and DLIP-processed samples, respectively.

In Fig. 5.14 (a) the response as a function of time of both type of sensors at 200 °C for concentrations ranging from 0.5 to 5 ppm of NO_2 is shown. From the sensitivity graph (see Fig. 5.14 (b)), two different slopes can be observed for concentrations higher and lower than 2 ppm. The average sensitivity values obtained for higher concentrations are 1.74 and 0.47 ppm^{-1} for DLIP + TT600C and TT600C, respectively. Nevertheless, for the lower ones, the sensitivity values of both type of sensors decrease to 0.95 and 0.20 ppm^{-1} for DLIP + TT600C and TT600C, respectively, but the reproducibility of the sensors is higher.

The limit of detection (LOD) has been calculated using the following formula: LOD
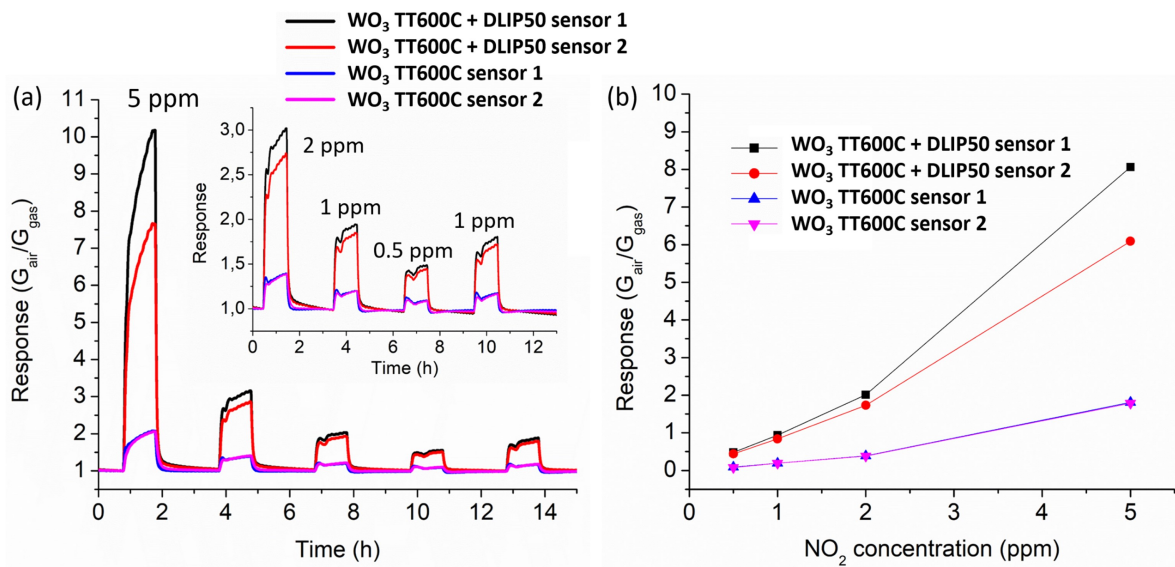
Figure 5.14 – (a) Response of two sensors DLIP-processed and two sensors only-annealed for 5, 2, 1, 0.5 and 1 ppm of NO$_2$ at 200 °C. Magnifications of the low concentrations are shown as an inset. (b) Sensitivity of the different sensors at 200 °C for concentrations between 0.5 and 5 ppm of NO$_2$.

$= 3\sigma/b$, where σ is the standard deviation of the baseline during 5 min and b is the slope of the sensitivity curve in the concentration range of 0.5 ppm - 2 ppm. For sensors processed by laser (LOD = 10 ppb), the LOD decreased to half of the value compared to the only-annealed samples (LOD = 20 ppb).

In order to study the cross sensitivity, mixtures of some interfering gases with 5 ppm of NO$_2$ have also been tested at 200 °C, as shown in Fig. 5.15 (the error bars have been calculated with the data of two different sensors). Common concentrations of interest for the interfering gases have been chosen: 25 ppm of CO and 5 ppm of HCHO. In all the mixtures, responses have been calculated through equation (5.2) (SR = G$_{air}$/G$_{gas}$) because conductivity decreases. This result means that the NO$_2$ oxidizing contribution is dominant, overcoming the reducing interference, especially for the DLIP-processed sensors. The performance of DLIP-processed sensors makes them suitable to be employed as NO$_2$ sensors in atmospheres with CO and HCHO.

As shown in the previous section, significantly different responses have been found for the two type of sensors tested in the experimental conditions considered in the present work. Therefore, different detection mechanisms can be suggested in the two cases.

For low temperatures (T < 250 °C) it is generally accepted that reaction (5.3) takes place, where NO$_2$ reacts directly with the semiconductor surface, generating adsorbed NO$_2$ species and, consequently, decreasing the conductivity of the material [121, 123, 145].

$$NO_{2(g)} + e^- \Longrightarrow NO^-_{2(ads)} \qquad (5.3)$$

At higher temperatures, the reducing behaviour of NO$_2$ has also been reported for WO$_3$ based sensors [191], as in the current case for the only-annealed sensors. The
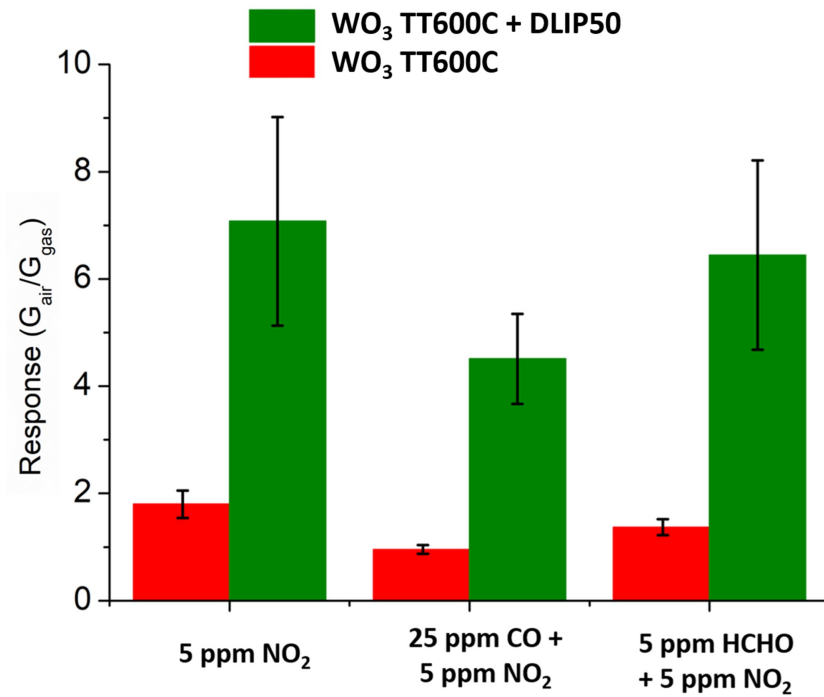
Figure 5.15 – Responses at 200 °C for 5 ppm of NO$_2$, 5 ppm of HCHO + 5 ppm of NO$_2$ and 25 ppm of CO + 5 ppm of NO$_2$. In this graph, to calculate the response, equation (5.2) has been used because the conductivity decreased.

result could be explained by the fact that for temperatures higher than 250 °C and low concentrations, NO$_2$ molecules reacts following the reaction (5.4), which is reducing [88].

$$NO_{2(g)} + O^-_{(ads)} \Longrightarrow NO_{(g)} + O_{2(g)} + e^- \tag{5.4}$$
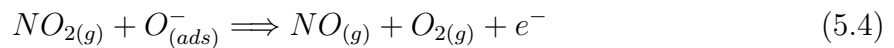
For the DLIP-processed sensors at temperatures higher than 250 °C, the small decrease in conductance could be due to a combination of reaction (5.4) and (5.5) [88].

$$NO_{2(g)} + e^- \Longrightarrow NO_{(g)} + O^-_{(ads)} \tag{5.5}$$
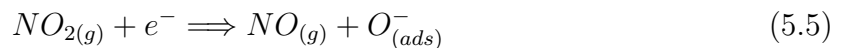
At 200 °C, the main difference between the detection mechanism of reducing and oxidizing gases is that, while reducing gases interact with the adsorbed oxygen species (mainly O$^-$, because for T > 100 °C the reaction (5.6) starts and O$^-$ is dominant at about 200 °C [87]), oxidizing agents such as NO$_2$ tend to be directly adsorbed on the surface (reaction (5.3)).

$$O^-_{2(ads)} + e^- \Longleftrightarrow 2O^-_{(ads)} \tag{5.6}$$

The reactions that are usually reported for CO and HCHO molecules are (5.7) and (5.8), respectively [123, 192]. For both molecules, the interaction exists with the O$^-$ species.

$$CO_{(g)} + O_{ads}^- \Longrightarrow CO_{2(g)} + e^- \tag{5.7}$$

$$HCHO_{(g)} + O_{ads}^- \Longrightarrow HCOOH_{(g)} + e^- \tag{5.8}$$
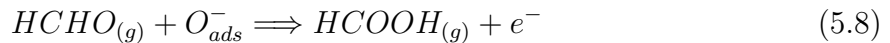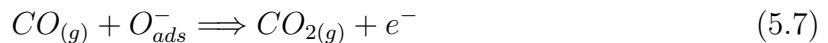
In order to understand the oxygen species adsorbed in each type of sensor, the conductance has been measured as a function of the temperature as described in the experimental section. The Arrhenius plots in air and under 5 ppm of NO$_2$ are shown in Fig. 5.16. From temperatures between 150 °C and 250 °C, it is clear that the difference between the Arrhenius plot in air and in NO$_2$ is higher for the DLIP-processed sensors, indicating higher NO$_2$ adsorption.

Referring to the Arrhenius plot, as explained in [193], the minimum in resistance (or maximum in conductivity) at low temperatures, in the conductance variation in air, is where the O$^-$ adsorption starts counteracting the oxygen physisorption. From Fig. 5.16, it can be appreciated that the slopes before and after the maximum in conductance for the DLIP-processed sensors are steeper than for only-annealed sensors, indicating that laser treated sensors present higher concentration of sites for adsorption or physisorption. This result highlights that the DLIP-processed sensors probably have laser-induced defects that work as adsorption sites, apart from the oxygen vacancies revealed by TOF-SIMS. This would enhance the NO$_2$ sensitivity, since more NO$_2$ molecules could be adsorbed extracting electrons from the conduction band and thus increasing the resistance.

5.3   Conclusions

1D structures have been generated by DLIP technique on WO$_3$ thin film sensors after annealing and compared to only-annealed sensors. The surface morphology modification has not affected the crystal structure, which remains tetragonal for both films, with similar crystallite sizes. Raman characterization confirms the good crystal structure of the WO$_3$ and TOF-SIMS analysis shows reduced layers on the top of the WO$_3$ film, probably due to oxygen vacancies.

Sputtered WO$_3$ based sensors processed by DLIP have shown responses $\simeq 3.5$ times higher than only-annealed sensors to NO$_2$ at 200 °C. The LOD is 20 ppb for the only-annealed sensors and it decreases to 10 ppb for the DLIP-processed sensors. Besides, DLIP-processed sensors show low cross sensitivity to CO and HCHO, what makes them suitable for environmental applications.

Conductance variation as a function of temperature in air atmosphere and under 5 ppm of NO$_2$ points out that DLIP-processed sensors probably present a higher number of adsorption sites. This contributes to the enhancement of the NO$_2$ sensitivity.
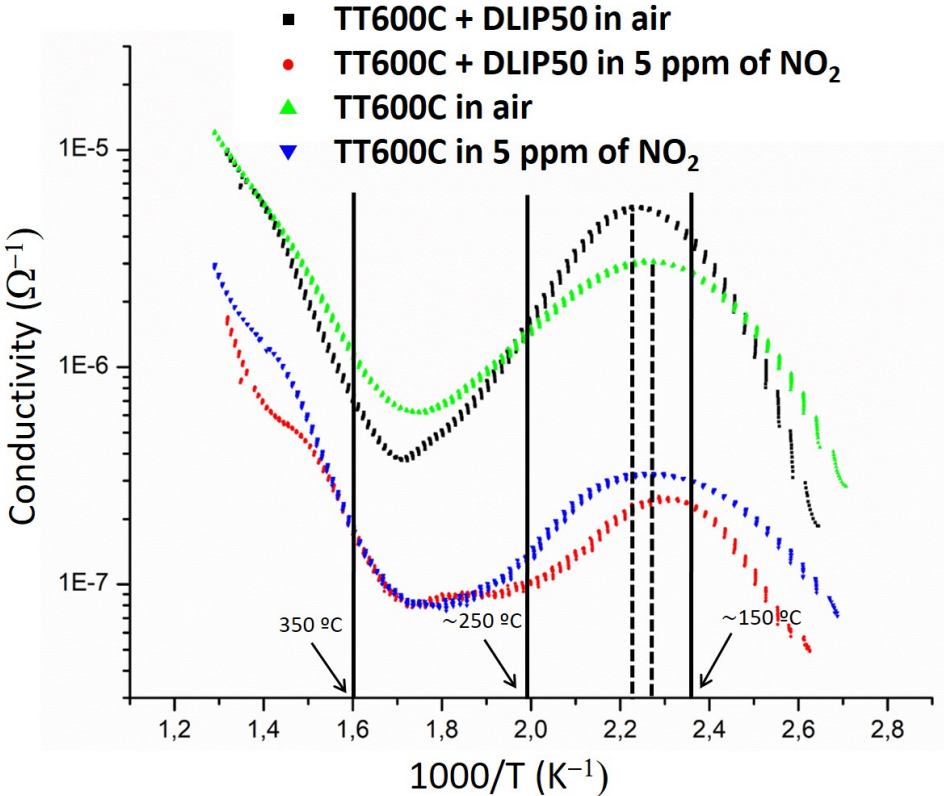
Figure 5.16 – Arrhenius plots in air and in 5 ppm of NO_2 for the sensors only-annealed and DLIP-processed.

Chapter 6

Sensor implementation in a gas detector

The influence of some fabrication parameters in the gas sensor behaviour has already been stated and discussed in previous chapters. Nevertheless, not only the way the material has been obtained is relevant for the sensor performance. The conditions under which the detection is carried out are of great importance, namely the temperature of the material during detection and the gas flow conditions, among others.

For this reason, in the first part of this chapter the influence of the sensor position inside the chamber and the gas flow are analysed, comparing the experimental results with flow dynamic simulations. This work was carried out in collaboration with "Mondragon Unibertsitatea-Goi Eskola Politeknikoa" (MU).

Furthermore, the implementation of a sensor in a practical device, able to operate in a real environment was carried out in close collaboration with IKOR[1]. In this case, the sensor is incorporated in an electronic platform including a circuit with the capacity to provide power to the heater and to measure the resistance variations of the sensor. This circuit is a part of a wireless communication system, able to transmit the data in real time, display it on a screen and store it as requested by the user. The suitability of the platform for a real application is checked by comparing the results obtained with the platform with the results obtained using the laboratory data acquisition devices and methods.

6.1 Influence of position of the sensor and flow in gas detection

The way the flow arrives at the sensor surface has relevance for the sensor response, mainly for the velocity of the response, but also because it can modify the temperature of the sensor. The position of the gas input and output inside the sensor chamber, as well as the magnitude of the gas flow, influence the way the concentration gradient reaches

---

[1]www.ikor.es/

the sensing material.

Moreover, convective flows are generated inside the chamber due to the sensor itself, because it acts as a heat source. As the convective flows can generate random concentration gradients, the response of the sensor will vary regarding the position of the heat source, namely, of the sensor itself.

6.1.1 Gas flow simulations and experimental

The gas flow simulations were entirely performed by the "Mecánica de Fluidos" group of MU. A finite volume method based on numerical fluid flow analysis was used to obtain decoupled solution for both the Navier-Stokes equations and the mass diffusion equations (convection-diffusion equations) in the absence of reaction-transport equations and involving a high degree of convection-diffusion discretisation schemes, applied to solve the combined effects of both convection and diffusion.

The numerical simulations were performed in Ansys Fluent software in 3D manner, based on the assumption of ideal gas conditions, using a K-w SST turbulence model in a transient flow, where a 0.001 s time step was established. A mass flow inlet with a mass fraction of NO_2 of $7.94418 \cdot 10^{-6}$ (5 ppm of NO_2) relative to air was set and atmospheric pressure was imposed in the outlet.

Drawings of the simulated chamber with the sensor at different positions are shown in Fig. 6.1. The inlet and outlet flow positions are also indicated. The temperature of the sensor heater was set at 300 °C for all the simulations.
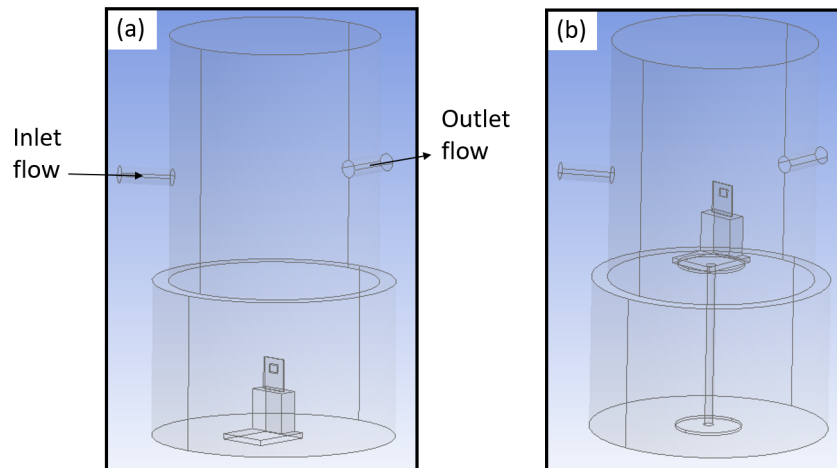
Figure 6.1 – Drawings of the simulated chamber with the (a) sensor at the bottom of the chamber and (b) in the middle of the chamber.

In order to investigate the effects of the position of the sensor and the flow of the gas inside the chamber during the sensing process, three cases were simulated:

 (i) Case I: sensor at the bottom position and 200 sccm of flow (Fig. 6.1 (a)).

 (ii) Case II: sensor at the bottom position and 400 sccm of flow (Fig. 6.1 (a)).

(iii) Case III: sensor in the middle position and 400 sccm of flow (Fig. 6.1 (b)).

To compare the experimental results with the simulations, the same three cases as in the simulations were experimentally studied. The chamber and set-up used for all the electrical measurements were the same as in chapter 3 and the response of a WO_3 based sensor was monitored at 300 °C for 5 ppm of NO_2. The NO_2 was taken from a certified bottle (Air Liquide) of 50 ppm mixed with synthetic air.

6.1.2   Results

The comparison of the simulations and the experimental results for the three different cases are shown in Fig. 6.2, where the simulated NO_2 concentration arriving at the sensor (black) and the response of the sensor (blue) are plotted in the left and right axis, respectively.
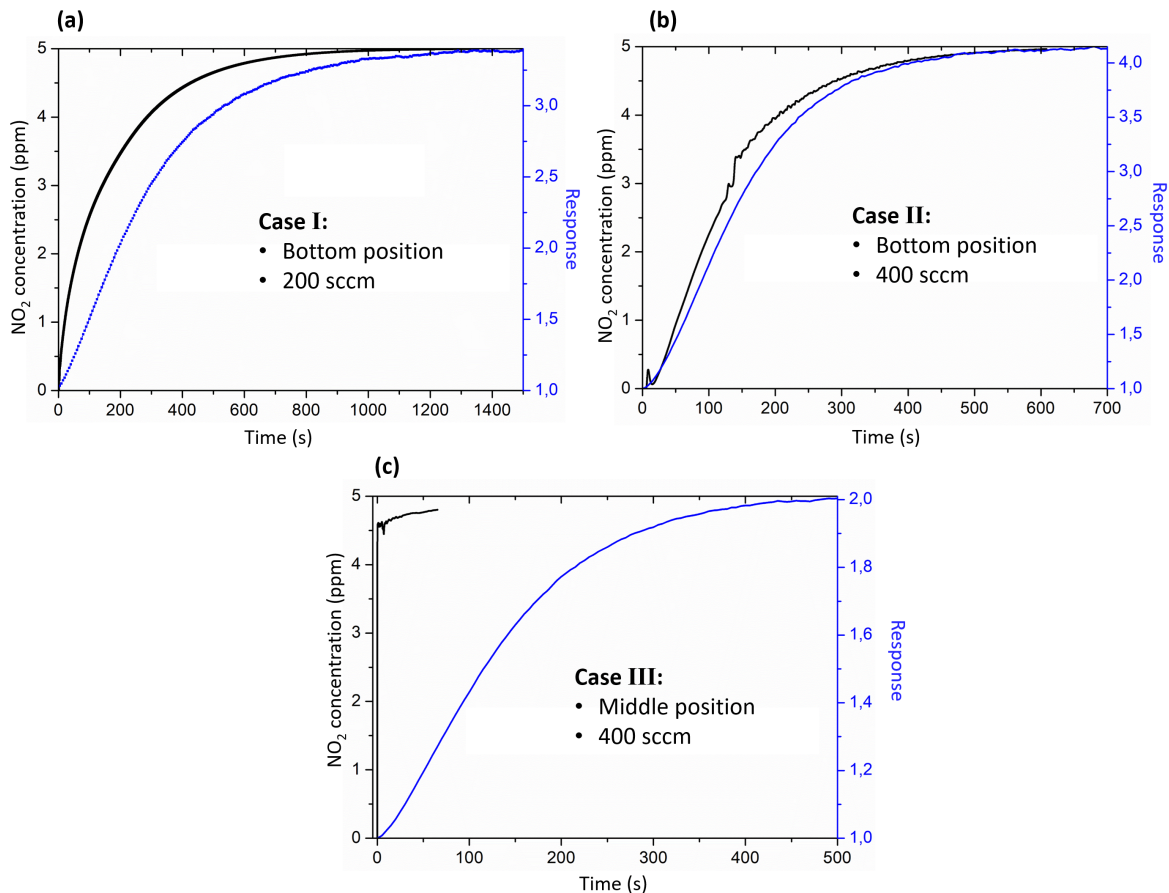
Figure 6.2 – Simulated NO_2 concentration arriving at the sensor and response of the sensor for 5 ppm of NO_2 at 300 °C (a) at the bottom of the chamber and with 400 sccm of flow, (b) at the bottom of the chamber and with 200 sccm of flow and (c) at the middle of the chamber and with 400 sccm of flow.

As expected, the simulation shows that the increase of the flow from 200 to 400 sccm for the same sensor position (case I and II) leads to a decrease of the time needed to have

5 ppm of NO_2 concentration on the sensor surface (from ~ 1400 to ~ 700 s). Moreover, in both cases the curve of the response of the sensor matches the simulation, especially for the case II.

On the other hand, if the sensor is placed in the middle of the chamber and the maximum flow is used (case III), the simulations states that in less than one second more than 4.5 ppm of NO_2 arrive at the sensor surface and then increases more slowly up to the maximum concentration introduced in the chamber (5 ppm). By contrast, from the experimental data, the needed time to reach the maximum response is ~ 500 s (the lowest time regarding the three different cases). This substantial difference between the simulation and the experimental results in the case III could be explained by the fact that this type of sensors have a minimum response time to reach the response value. Therefore, although the desired concentration reaches the sensor surface very fast, the sensors would need at least 8 min, in this case, to reach their maximum response, probably due to diffusion processes.

It is worth noticing that for the same sensor and working temperature, responses have ranged from 2 to 4 approximately, depending on the chamber position and flow introduced, what confirms the strong influence of the operating conditions. From the cases analysed here, case II would be a good compromise between response of the sensor and simulated time that 5 ppm of NO_2 need to reach the sensor surface.

6.2 Sensor implementation in an electronic platform with wireless communication

The wireless platform provided by IKOR is based on two modules: the sensor and the display modules. The sensor module (see Fig. 6.3 (a) and (b)) heats up the sensor to the desired temperature trough a control unit based on a control transistor that allows or blocks the current in order to achieve the necessary power. In order to measure the dynamic variation of the sensors resistance, the module presents five standard resistances (1 MΩ, 100 kΩ, 10 kΩ, 1 kΩ and 100 Ω) that will be compared with the resistance of the sensor, keeping the closest to that value. Comparing both values, it will be able to measure the sensor resistance. The data collected by the sensor module will be transferred by Wireless M-BUS[2] to the Human Machine Interface (HMI).

The HMI is the display module (see Fig. 6.3 (c)) of the IKOR platform, where the measurements can be seen in real time. This module receives the data from the sensor module and plots them instantaneously. The data can be collected with a Universal Serial Bus (USB) after the measurements are performed.

---

[2]M-Bus (Meter-Bus) is an European standard for the remote reading of gas or electricity meters. Specifically, the recently open band for remote reading in Europe (169 MHz) has been used.
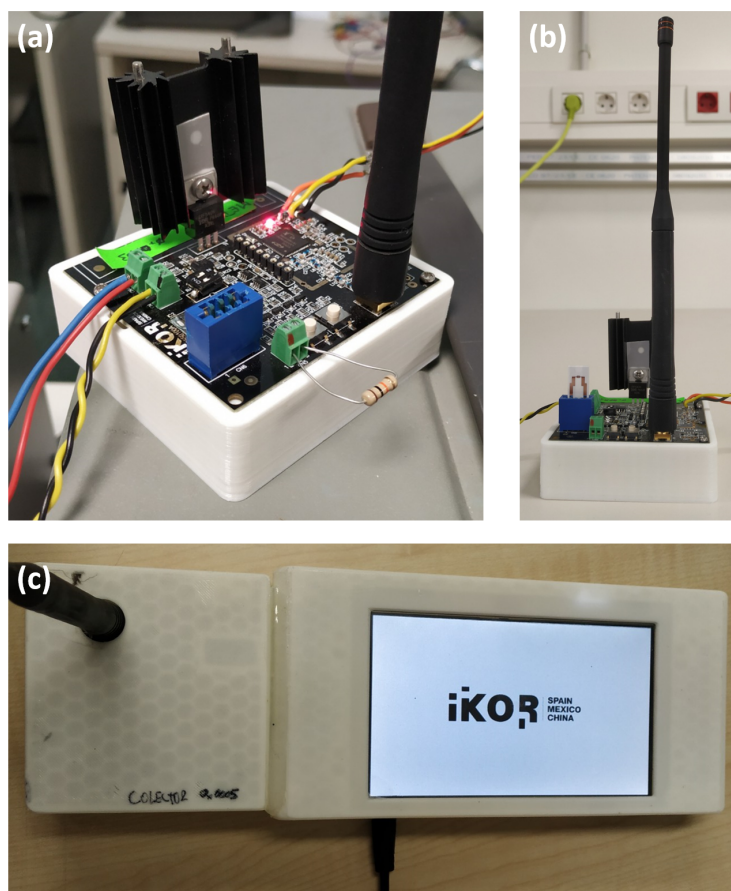
Figure 6.3 – (a) And (b) sensor module and (c) display module of the IKOR platform.

6.2.1   Experimental

The chamber and set-up used for all the electrical measurements were the same as in chapter 3, with the sensor in the middle of the chamber. The sensor used for the experiments is a ZnO based sensor and the gas tested is NO_2 taken from a certified bottle (Air Liquide) of 50 ppm mixed with synthetic air.

During the heating process of the sensor from room to the optimal temperature, in this case 350 °C, the resistance was measured using two different approaches:

- Applying 3 V to the IDT electrodes and measuring the flowing intensity with a Keithley 2000 multimeter (as it was done in chapter 3 and 4). This method will be named Keithley3V.

- Using the wireless platform provided by IKOR. This electrical acquisition will be named IKOR.

Instead, while measuring the signal variation of the device at constant temperature (350 °C) when the atmosphere is modified, an extra mode was attempted:

- Directly acquiring the resistance with a Keithley 2000 multimeter. This method will be named KeithleyR.

6.2.2   Results

The results obtained during the heating procedure are shown in Fig. 6.4. Typical step-shape resistance is shown for the characterization performed with Keithley3V when temperature jumps are introduced. There are also some rapid peaks when no jump in temperature exists, probably due to contact issues with the cables; nonetheless, the measure is reliable. By contrast, the electrical acquisition performed by the IKOR platform does not accurately measure the resistance at low temperatures, as shown in Fig. 6.4 (b). This noise is probably coming from the fact the sensor presents high resistance values at low temperatures and the noise is directly proportional to the resistance value.
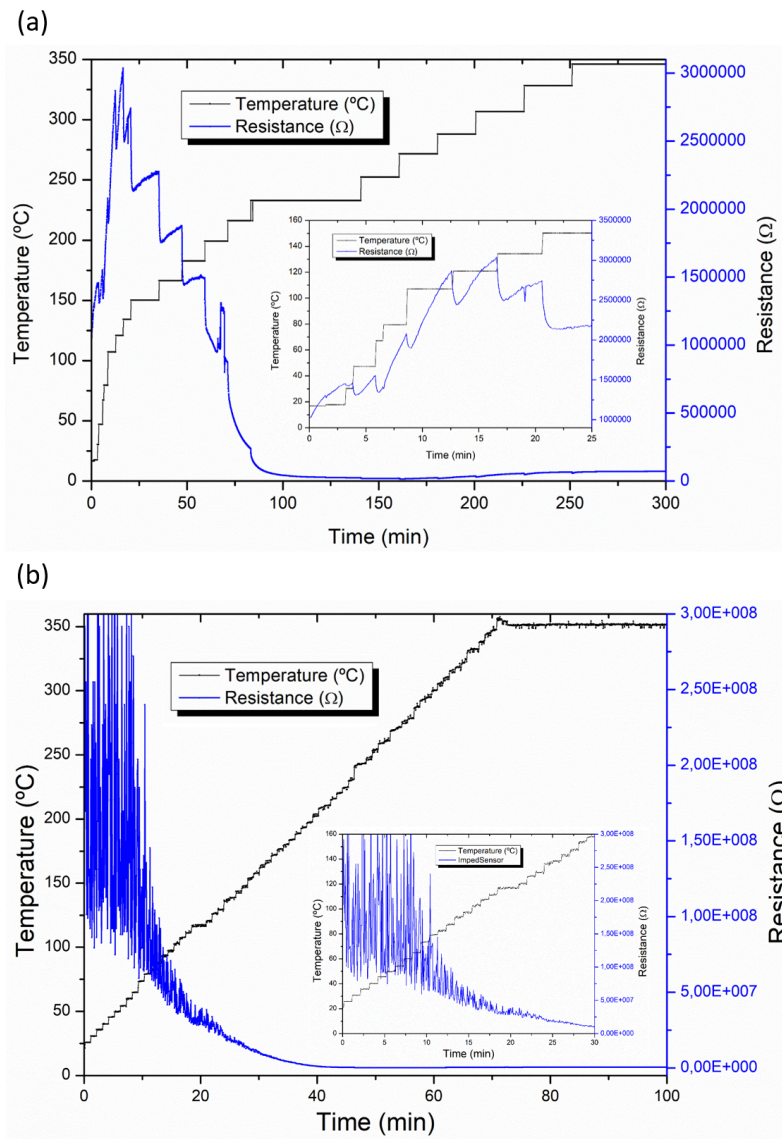
Figure 6.4 – Temperature of the heater and resistance of the sensor versus time measured by (a) Keithley3V and (b) IKOR. The inlet graphs are magnifications of the heating at lower temperatures.

The resistance variation at constant temperature while varying the atmosphere is

shown in Fig. 6.5. As it can be appreciated, the responses are very similar for the case of Keithley3V and IKOR, although the measures acquired by IKOR present slightly higher noise. Nevertheless, as the absolute value of the resistance is lower at 350 °C than at room temperature, the noise has decreased enough to have a sufficiently accurate measurement.
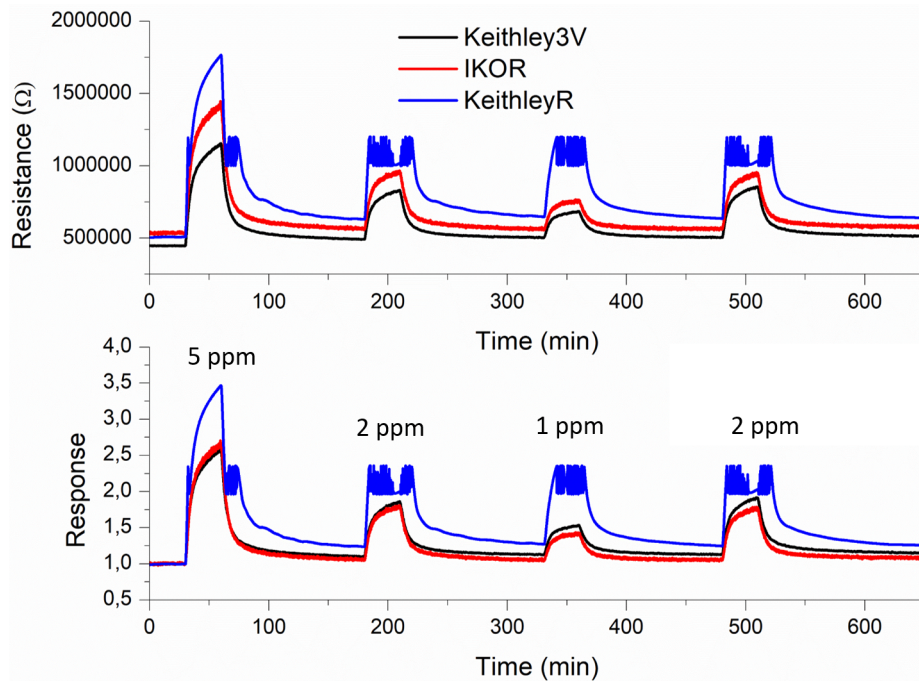
Figure 6.5 – Resistance and response of the ZnO based sensor DLIP85 for 5 ppm, 2 ppm, 1 ppm and 2 ppm of NO_2, acquired with the Keithley while applying 3 V, with the IKOR platform and directly with the Keithley (KeithleyR).

By contrast, the resistance acquired by KeithleyR presents consecutive jumps between 1 MΩ and 1.25 MΩ. This effect can be explained by the Keithley 2000 working mechanism. A Keithley 2000 multimeter applies different values of intensity to the sensor depending on the order of magnitude of the resistance measured. In Table 6.1, the intensity applied by a Keithley 2000 multimeter for each resistance range is shown. Therefore, when the resistance is close to 1 MΩ, as it is the case here, the test current shifts from 10 μA to 70 nA, leading to the consecutive jumps (consecutive shifts in current) until the test current is stabilized again.

6.3   Conclusions

Simulation and experimental data were compared for three different operating conditions, in order to understand the influence of the flow and sensor position inside the chamber on the final sensing response. As a conclusion, a strong influence was detected for the sensor position inside the chamber, doubling the sensor response when the sensor is at the bottom of the chamber compared to having the sensor in the middle. Besides, when the flow is increased from 200 to 400 sccm, the time needed to reach the maximum concentration on the sensor surface also decreases by a factor of 2.

	Range	Resolution	Test current
Resistance	100.0000 Ω	100 $\mu\Omega$	1 mA
	1.000000 kΩ	1 mΩ	1 mA
	10.00000 kΩ	10 mΩ	100 μA
	100.0000 kΩ	100 mΩ	10 μA
	1.000000 MΩ	1 Ω	10 μA
	10.00000 MΩ	10 Ω	70 nA
	100.0000 MΩ	100 Ω	70 nA

Table 6.1 – Resistance range, resolution and test current used in a Keithley 2000 multimeter. The information is extracted from the equipment data sheet.

In the second section of this chapter, one of the sensors designed in this thesis was successfully implemented in an electronic platform with wireless communication provided by IKOR. Although the IKOR platform does not provide an accurate measurement when the resistances are too high, as for example during the heating process of the sensor, it works properly for measurements performed at a constant working temperature. In a real sensor device for pollutants detection, the harmful pollutant concentration will be measured once the sensor is at the desired temperature; therefore, the IKOR platform presents the necessary features for such a purpose.

Chapter 7

Global discussion, conclusions and future work

After the detailed description of the results obtained in this work, this chapter presents a comparison between all the fabricated sensors in this thesis. In addition, a summary of the main conclusions and future work suggestions to continue the research in this area are given.

7.1   Global discussion

First, it is important to point out that chapters 3, 4 and 5 presented a slightly different experimental set-ups, due to distinct laboratory conditions. Therefore, in this section, where comparison between chapters is presented, the experimental conditions have to be taken into account.

In Table 7.1 the comparison between the fabricated sensors is exposed. As shown, there exists an improvement of the sensor response for the three type of laser nanostructuring approaches compared to their respectively annealed counterparts, indicating the benefits provided by the laser treatment.

For ZnO based sensors, the thermal treatment improves the sensing response as the annealing temperature increases, probably due to the influence of the crystal structure and crystallite size. Nevertheless, it is worth mentioning that ZnO DLIP85 and DLIP165 sensors that do not require annealing process, present sensor responses, response and recovery times comparable to the annealed ones. Especially for the lower fluence sensor (DLIP85), which could be a very promising substitute of the annealed sensors, avoiding the thermal treatment step.

The sensors in chapter 4 and 5 (ZnO with LIPSS and WO_3 processed by DLIP) present a substantial enhancement of the response compared with the respective sensors without laser treatment and furthermore, a significant decrease of the recovery time, what makes them very suitable for real applications. In the case of WO_3 based sensors, the decrease of the recovery time is probably influenced by the higher gas flow used during the experiments (500 sccm vs 400 sccm), nevertheless it has to be taken into account that

also the optimal temperature is the lowest among all the sensors (200 °C).

Among all the sensors, the ZnO based sensors annealed at 800 °C and processed with LIPSS present the best response, even if the chamber where the gas experiments were performed was the one with the highest volume (0.97 l). Comparing its performance with other published pure ZnO nanostructured sensors [135–137], comparable results are found. Although in the other works, the optimal temperatures are slightly lower than for the sensor with LIPSS, the reported fabrication techniques require several steps avoided here by the in-situ nanostructuring. It also worth mentioning that selectivity is not shown in any of the investigations. Moreover, repeatability measurements are rarely performed, leading to a lack of information for further comparison. By contrast, in chapter 4, a good repeatability over more than two months was successfully demonstrated, what is a key requirement for real applications.

7.2   Summary of results and conclusions

With this research work, three different types of laser nanostructured semiconductor gas sensors have been developed for the detection of low concentration of NO_2. Improvements in the sensing performance compared to classic annealing treatments have been obtained for the different approaches, pointing out the laser technologies potential for gas sensor applications. Following the outline of the this thesis, the main conclusions are summarized.

1. ZnO based gas sensors were fabricated by means of RF sputtering. Some of them were annealed and others nanostructured by DLIP at 85 and 165 mJ/cm^2 with a period of 730 nm. In all cases, the IDT electrodes are above the ZnO processed thin film.

   - Morphological characterization shows a granular surface for the annealed samples, a linear pattern with two different textures (granular and smooth) in the case of the DLIP85 sample and smooth with dispersed spheres for DLIP165. All samples present wurtzite ZnO crystal structure with a preferred orientation in the (002) direction.

   - The heat transfer equation was simulated for the DLIP process on the ZnO thin film and a thermal threshold of 900 K, where crystal modification occurs, was calculated, indicating a lateral and depth processing around 173 nm and 140 nm, respectively.

   - XPS reveals that all samples become richer on Zn compared to as-grown, possibly through an increase of oxygen vacancies and/or Zn interstitials. For DLIP85 sample, low influence on the thin film/substrate interface is demonstrated by TOF-SIMS, what can be suitable for temperature sensitive substrates.

   - As NO_2 sensors, DLIP85 presents the highest response and comparable response and recovery times with annealed sensors. As a result, this type of sensor could substitute of the annealed sensors, decreasing significantly the fabrication time of the device.

2. ZnO based gas sensors were fabricated by means of RF sputtering, annealed at 800 °C and then nanostructured with LIPSS on the ZnO surface. The IDT electrodes are beneath the ZnO thin film.

   - The femtosecond laser subwavelength patterning technique was integrated successfully into the sensor design by processing two lines of LIPSS on the ZnO thin film between every IDT electrode. The total processed area is 12.5 %.

   - The LIPSS nanostructures were identified as high spatial frequency LIPSS (HSFL) with an average period of 145 nm. Through Raman analysis, a decrease of the typical wurtzite ZnO structure is shown, with a possible increase of defects such as Zn interstitials.

   - The response under NO_2 is enhanced if compared with the only-annealed ZnO thin film for concentrations as low as 1 ppm, reaching 1 ppb of detection limit (LOD) for the sensors with LIPSS. The Zn interstitials defects could be the source of the adsorbed NO_2 species increasing the sensitivity.

   - Reproducible results have been measured during 11 weeks in a row.

3. WO_3 based gas sensors were fabricated by means of RF sputtering, annealing at 600 °C and then, some of the them nanostructured by DLIP at 50 mJ/cm^2 with a period of 500 nm. The IDT electrodes are beneath the WO_3 processed thin film. It was proved that the IDT Pt electrodes are not processed by the DLIP technique.

   - Morphological and structural characterization showed a hole structure in a periodic line-pattern for the DLIP-processed sensors while a flat surface for the only-annealed sensors, both with a tetragonal WO_3 phase. TOF-SIMS analysis revealed that the first WO_3 layers are reduced for both samples, which could improve sensing performances.

   - Promising response enhancement of DLIP-processed sensors were observed for low concentrations of NO_2 (from 0.5 ppm to 5 ppm) at 200 °C, lowering the limit of detection (LOD) to 10 ppb, half of the LOD of the only-annealed sensors (20 ppb).

   - Low cross sensitivity was demonstrated to CO and HCHO compared with NO_2 for both type of sensors, but especially for TT600C + DLIP50.

   - Conductance variation versus temperature in air atmosphere and under 5 ppm of NO_2 points out that DLIP-processed sensors probably present a higher number of adsorption sites, what contributes to the enhancement of the NO_2 sensitivity.

4. The influence of some operating conditions during the sensing measurements were analysed.

   - The sensor position inside the chamber affects especially on the sensor response, while the flow injected in the chamber modifies the response time of the gas sensor.

5. Sensors fabricated in this thesis were successfully integrated into a wireless platform.

- The IKOR wireless platform is able to monitor gas detection at constant temperature (350 °C) integrating the sensors fabricated in this thesis.

7.3   Future work

From the results and conclusions obtained in this dissertation, the following future research lines are proposed:

- Increase the number of beams of the DLIP technique and study of the influence on the sensing performance of the fabricated nanostructures.

- Increase the number of lines with LIPSS between the IDT electrodes and study of the influence of the processed area by femtosecond laser subwavelength patterning on the sensing performance.

- Fabrication of nanostructures using a combination of the two laser nanostructuring techniques studied in this thesis for gas sensing applications. **Two or three-beam interference of femtosecond laser:** this technique would generate a new pack of nanostructures with two different periods, one determined by the two or three-beam interference pattern and the other one induced by the single femtosecond laser beam [177, 194].

- Heading towards the industrialization of the fabrication process:

  - Miniaturization of the sensing device to optimize energy consumption.

  - Encapsulation of the device to control the gas amount arriving to the sensor and avoid fluctuations due to air flow variations.

  - Integrating humidity and interfering gas filters before the detection to improve the sensing performance.

Type of sensor	IDT position	Anneal. (°C)	Chamber volume (l)	Flow (sscm)	$T_{opt.}$ [a] (°C)	SR [b]	t_{90} (min)	t_{10} (min)	Sensitivity (ppm^{-1})	LOD (ppb)
ZnO TT600C	above	600	0.86	400	350	3.12	23.3	13.6	0.46	4
ZnO TT700C	above	700	0.86	400	350	3.97	14.1	70.0	0.57	1
ZnO DLIP85	above	—	0.86	400	350	6.49	17.9	16.2	1.15	2
ZnO DLIP165	above	—	0.86	400	350	2.29	16.2	17.9	0.24	1
ZnO TT800C	beneath	800	0.97	400	350	5.00	22.7	50.1	0.76	3
ZnO TT800C + LIPSS	beneath	800	0.97	400	350	10.30	13.9	32.1	1.71	1
WO$_3$ TT600C	beneath	600	0.60	500	200	1.80	24.0	9.8	0.20	20
WO$_3$ TT600C + DLIP50	beneath	600	0.60	500	200	7.08	24.1	6.7	0.95	10

Table 7.1 – Comparison of the sensor results obtained in the previous chapters.

[a]Optimal temperature of the sensors.
[b]Sensor response for 5 ppm of NO_2.

Bibliography

[1] M. J. Madou, S. R. Morrison, Chemical sensing with solid state devices, Elsevier, 2012.

[2] G. Korotcenkov, Handbook of Gas Sensor Materials, Vol. 1, Springer, 2013.

[3] G. Neri, First fifty years of chemoresistive gas sensors, Chemosensors 3 (1) (2015) 1–20.

[4] F. Schedin, A. Geim, S. Morozov, E. Hill, P. Blake, M. Katsnelson, K. Novoselov, Detection of individual gas molecules adsorbed on graphene, Nature materials 6 (9) (2007) 652.

[5] S. S. Varghese, S. Lonkar, K. Singh, S. Swaminathan, A. Abdala, Recent advances in graphene based gas sensors, Sensors and Actuators B: Chemical 218 (2015) 160–183.

[6] E. Llobet, Gas sensors using carbon nanomaterials: A review, Sensors and Actuators B: Chemical 179 (2013) 32–45.

[7] T. Hübert, L. Boon-Brett, G. Black, U. Banach, Hydrogen sensors–a review, Sensors and Actuators B: Chemical 157 (2) (2011) 329–352.

[8] F. E. Annanouch, S. Vallejos, T. Stoycheva, C. Blackman, E. Llobet, Aerosol assisted chemical vapour deposition of gas-sensitive nanomaterials, Thin Solid Films 548 (2013) 703–709.

[9] Y. Shen, B. Zhang, X. Cao, D. Wei, J. Ma, L. Jia, S. Gao, B. Cui, Y. Jin, Microstructure and enhanced H_2S sensing properties of Pt-loaded WO_3 thin films, Sensors and Actuators B: Chemical 193 (2014) 273–279.

[10] M. Penza, C. Martucci, G. Cassano, NO_x gas sensing characteristics of WO_3 thin films activated by noble metals (Pd, Pt, Au) layers, Sensors and Actuators B: Chemical 50 (1) (1998) 52–59.

[11] R. Jaaniso, O. K. Tan, Semiconductor gas sensors, Elsevier, 2013.

[12] Figaro.
URL http://www.figarosensor.com/

[13] E. Hamann, H. Manger, L. Steinke, Lambda-sensor with Y_2O_3-stabilized ZrO_2 ceramic for application in automotive emission control systems, SAE Transactions (1977) 1729–1734.

[14] A. A. Tomchenko, G. P. Harmer, B. T. Marquis, J. W. Allen, Semiconducting metal oxide sensor array for the selective detection of combustion gases, Sensors and Actuators B: Chemical 93 (1-3) (2003) 126–134.

[15] W. H. Brattain, J. Bardeen, Surface properties of germanium, Bell System Technical Journal 32 (1) (1953) 1–41.

[16] T. Seiyama, A. Kato, K. Fujiishi, M. Nagatani, A new detector for gaseous components using semiconductive thin films., Analytical Chemistry 34 (11) (1962) 1502–1503.

[17] N. Taguchi, Gas-detecting device, US Patent 3,631,436 (Dec. 28 1971).

[18] S. Vallejos, V. Khatko, J. Calderer, I. Gracia, C. Cané, E. Llobet, X. Correig, Micromachined WO_3-based sensors selective to oxidizing gases, Sensors and Actuators B: Chemical 132 (1) (2008) 209–215.

[19] S. Rank, S. Hafner, N. Barsan, U. Weimar, The impact of the nature of the electrode material on SnO_2 thick film sensor performance: Influence on oxygen adsorption, Procedia Engineering 47 (2012) 514–517.

[20] X. Vilanova, E. Llobet, J. Brezmes, J. Calderer, X. Correig, Numerical simulation of the electrode geometry and position effects on semiconductor gas sensor response, Sensors and Actuators B: Chemical 48 (1-3) (1998) 425–431.

[21] J. Prades, R. Jimenez-Diaz, F. Hernandez-Ramirez, S. Barth, A. Cirera, A. Romano-Rodriguez, S. Mathur, J. Morante, Ultralow power consumption gas sensors based on self-heated individual nanowires, Applied Physics Letters 93 (12) (2008) 123110.

[22] X. Huang, F. Meng, Z. Pi, W. Xu, J. Liu, Gas sensing behavior of a single tin dioxide sensor under dynamic temperature modulation, Sensors and Actuators B: Chemical 99 (2-3) (2004) 444–450.

[23] J. Prades, R. Jimenez-Diaz, F. Hernandez-Ramirez, J. Pan, A. Romano-Rodriguez, S. Mathur, J. Morante, Direct observation of the gas-surface interaction kinetics in nanowires through pulsed self-heating assisted conductometric measurements, Applied Physics Letters 95 (5) (2009) 053101.

[24] G. G. Mandayo, Gas detection by semiconductor ceramics: tin oxide as improved sensing material, Sensor Letters 5 (2) (2007) 341–360.

[25] I. Castro-Hurtado, T. Tavera, P. Yurrita, N. Pérez, A. Rodriguez, G. G. Mandayo, E. Castaño, Structural and optical properties of WO_3 sputtered thin films nanostructured by laser interference lithography, Applied Surface Science 276 (2013) 229–235.

[26] Z. Liu, T. Yamazaki, Y. Shen, T. Kikuta, N. Nakatani, Influence of annealing on microstructure and NO_2-sensing properties of sputtered WO_3 thin films, Sensors and Actuators B: Chemical 128 (1) (2007) 173–178.

[27] I. Castro-Hurtado, J. Herran, N. Perez, S. Olaizola, G. G. Mandayo, E. Castano, Toxic gases detection by NiO sputtered thin films, Sensor letters 9 (1) (2011) 64–68.

[28] F. E. Annanouch, G. Bouchet, P. Perrier, N. Morati, C. Reynard-Carette, K. Aguir, M. Bendahan, How the chamber design can affect gas sensor responses, in: Multi-disciplinary Digital Publishing Institute Proceedings, Vol. 2, 2018, p. 820.

[29] N. Yamazoe, New approaches for improving semiconductor gas sensors, Sensors and Actuators B: Chemical 5 (1-4) (1991) 7–19.

[30] B. Bhushan, Y. C. Jung, Wetting, adhesion and friction of superhydrophobic and hydrophilic leaves and fabricated micro/nanopatterned surfaces, Journal of Physics: Condensed Matter 20 (22) (2008) 225010.

[31] W. Fan, S. Zhang, N.-C. Panoiu, A. Abdenour, S. Krishna, R. M. Osgood, K. J. Malloy, S. R. J. Brueck, Second harmonic generation from a nanopatterned isotropic nonlinear material, Nano Letters 6 (5) (2006) 1027–1030.

[32] Y. Wang, K. Zang, S. Chua, C. Fonstad, Catalyst-free growth of uniform ZnO nanowire arrays on prepatterned substrate, Applied physics letters 89 (26) (2006) 263116.

[33] E. Menard, M. A. Meitl, Y. Sun, J.-U. Park, D. Jay-Lee Shir, Y.-S. Nam, S. Jeon, J. A. Rogers, Micro-and nanopatterning techniques for organic electronic and opto-electronic systems, Chem. Rev 107 (2007) 1117–1160.

[34] J. Hermann, M. Benfarah, S. Bruneau, E. Axente, G. Coustillier, T. Itina, J. Guille-moles, P. Alloncle, Comparative investigation of solar cell thin film processing using nanosecond and femtosecond lasers, Journal of Physics D: Applied Physics 39 (3) (2006) 453.

[35] S.-W. Fan, A. K. Srivastava, V. P. Dravid, Nanopatterned polycrystalline ZnO for room temperature gas sensing, Sensors and Actuators B: Chemical 144 (1) (2010) 159–163.

[36] G. Jimenez-Cadena, J. Riu, F. X. Rius, Gas sensors based on nanostructured materials, Analyst 132 (11) (2007) 1083–1099.

[37] S. R. Morrison, Semiconductor gas sensors, Sensors and Actuators 2 (1981) 329–341.

[38] C. Wang, L. Yin, L. Zhang, D. Xiang, R. Gao, Metal oxide gas sensors: sensitivity and influencing factors, Sensors 10 (3) (2010) 2088–2106.

[39] E. Comini, G. Faglia, G. Sberveglieri, Z. Pan, Z. L. Wang, Stable and highly sensitive gas sensors based on semiconducting oxide nanobelts, Applied Physics Letters 81 (10) (2002) 1869–1871.

[40] Y.-F. Sun, S.-B. Liu, F.-L. Meng, J.-Y. Liu, Z. Jin, L.-T. Kong, J.-H. Liu, Metal oxide nanostructures and their gas sensing properties: a review, Sensors 12 (3) (2012) 2610–2631.

[41] L. Zhang, J. Zhao, J. Zheng, L. Li, Z. Zhu, Shuttle-like ZnO nano/microrods: Facile synthesis, optical characterization and high formaldehyde sensing properties, Applied Surface Science 258 (2) (2011) 711–718.

[42] M. Chen, Z. Wang, D. Han, F. Gu, G. Guo, Porous ZnO polygonal nanoflakes: synthesis, use in high-sensitivity NO_2 gas sensor, and proposed mechanism of gas sensing, The Journal of Physical Chemistry C 115 (26) (2011) 12763–12773.

[43] Z. Liu, M. Miyauchi, T. Yamazaki, Y. Shen, Facile synthesis and NO_2 gas sensing of tungsten oxide nanorods assembled microspheres, Sensors and Actuators B: Chemical 140 (2) (2009) 514–519.

[44] R. Wagner, W. Ellis, Vapor-liquid-solid mechanism of single crystal growth, Applied Physics Letters 4 (5) (1964) 89–90.

[45] I. Castro-Hurtado, J. Herrán, G. Mandayo, E. Castaño, SnO_2-nanowires grown by catalytic oxidation of tin sputtered thin films for formaldehyde detection, Thin Solid Films 520 (14) (2012) 4792–4796.

[46] N. Kaur, E. Comini, D. Zappa, N. Poli, G. Sberveglieri, Nickel oxide nanowires: vapor liquid solid synthesis and integration into a gas sensing device, Nanotechnology 27 (20) (2016) 205701.

[47] S. Vallejos, S. Selina, F. E. Annanouch, I. Gràcia, E. Llobet, C. Blackman, Aerosol assisted chemical vapour deposition of gas sensitive SnO_2 and Au-functionalised SnO_2 nanorods via a non-catalysed vapour solid (VS) mechanism, Scientific reports 6 (2016) 28464.

[48] S. Vallejos, N. Pizúrová, I. Gràcia, C. Sotelo-Vazquez, J. Čechal, C. Blackman, I. Parkin, C. Cané, ZnO rods with exposed {100} facets grown via a self-catalyzed vapor–solid mechanism and their photocatalytic and gas sensing properties, ACS applied materials & interfaces 8 (48) (2016) 33335–33342.

[49] C. Zou, F. Liang, S. Xue, Synthesis and oxygen vacancy related NO_2 gas sensing properties of ZnO:Co nanorods arrays gown by a hydrothermal method, Applied Surface Science 353 (2015) 1061–1069.

[50] S. Shendage, V. Patil, S. Vanalakar, S. Patil, N. Harale, J. Bhosale, J. Kim, P. Patil, Sensitive and selective NO_2 gas sensor based on WO_3 nanoplates, Sensors and Actuators B: Chemical 240 (2017) 426–433.

[51] R. Ab Kadir, Z. Li, A. Z. Sadek, R. Abdul Rani, A. S. Zoolfakar, M. R. Field, J. Z. Ou, A. F. Chrimes, K. Kalantar-Zadeh, Electrospun granular hollow SnO_2 nanofibers hydrogen gas sensors operating at low temperatures, The Journal of Physical Chemistry C 118 (6) (2014) 3129–3139.

[52] L. Giancaterini, S. Emamjomeh, A. De Marcellis, E. Palange, A. Resmini, U. Anselmi-Tamburini, C. Cantalini, The influence of thermal and visible light activation modes on the NO_2 response of WO_3 nanofibers prepared by electrospinning, Sensors and Actuators B: Chemical 229 (2016) 387–395.

[53] H. J. Fan, P. Werner, M. Zacharias, Semiconductor nanowires: from self-organization to patterned growth, small 2 (6) (2006) 700–717.

[54] P. Candeloro, A. Carpentiero, S. Cabrini, E. Di Fabrizio, E. Comini, C. Baratto, G. Faglia, G. Sberveglieri, A. Gerardino, SnO_2 sub-micron wires for gas sensors, Microelectronic Engineering 78 (2005) 178–184.

[55] L. Müller-Meskamp, Y. H. Kim, T. Roch, S. Hofmann, R. Scholz, S. Eckardt, K. Leo, A. F. Lasagni, Efficiency enhancement of organic solar cells by fabricating periodic surface textures using direct laser interference patterning, Advanced Materials 24 (7) (2012) 906–910.

[56] R. R. Gattass, E. Mazur, Femtosecond laser micromachining in transparent materials, Nature photonics 2 (4) (2008) 219.

[57] A. Lasagni, T. Roch, M. Bieda, D. Benke, E. Beyer, High speed surface functionalization using direct laser interference patterning, towards 1 m²/min fabrication speed with sub-μm resolution, in: Laser-based Micro-and Nanoprocessing VIII, Vol. 8968, International Society for Optics and Photonics, 2014, p. 89680A.

[58] A. Rodriguez, M. Echeverría, M. Ellman, N. Perez, Y. K. Verevkin, C. S. Peng, T. Berthou, Z. Wang, I. Ayerdi, J. Savall, et al., Laser interference lithography for nanoscale structuring of materials: From laboratory to industry, Microelectronic Engineering 86 (4-6) (2009) 937–940.

[59] P. Rodríguez-Franco, A. Arriola, N. Darwish, J. Jaramillo, H. Keshmiri, T. Tavera, S. Olaizola, M. Moreno, Fabrication of broad area optical nanostructures for high throughput chemical sensing, Sensors and Actuators B: Chemical 187 (2013) 356–362.

[60] A. Arriola, A. Rodriguez, N. Perez, T. Tavera, M. J. Withford, A. Fuerbach, S. M. Olaizola, Fabrication of high quality sub-micron Au gratings over large areas with pulsed laser interference lithography for SPR sensors, Optical Materials Express 2 (11) (2012) 1571–1579.

[61] H. Li, X. Luo, C. Du, X. Chen, Y. Fu, Ag dots array fabricated using laser interference technique for biosensing, Sensors and Actuators B: Chemical 134 (2) (2008) 940–944.

[62] E. Stankevičius, M. Gedvilas, B. Voisiat, M. Malinauskas, G. Račiukaitis, Fabrication of periodic micro-structures by holographic lithography, Lithuanian Journal of Physics 53 (4).

[63] S. Eckhardt, C. Sachse, A. Lasagni, Light management in transparent conducting oxides by direct fabrication of periodic surface arrays, Physics Procedia 41 (2013) 552–557.

[64] M. Bieda, E. Beyer, A. F. Lasagni, Direct fabrication of hierarchical microstructures on metals by means of direct laser interference patterning, Journal of Engineering Materials and Technology 132 (3) (2010) 031015.

[65] A. F. Lasagni, D. F. Acevedo, C. A. Barbero, F. Mücklich, One-step production of organized surface architectures on polymeric materials by direct laser interference patterning, Advanced Engineering Materials 9 (1-2) (2007) 99–103.

[66] M. Soldera, K. Taretto, J. Berger, A. F. Lasagni, Potential of photocurrent improvement in μc-si: H solar cells with tco substrates structured by direct laser interference patterning, Advanced Engineering Materials 18 (9) (2016) 1674–1682.

[67] S. Ring, B. Stannowski, F. Fink, R. Schlatmann, Micro gratings written in ZnO:Al thin films using picosecond UV-laser interference patterning, physica status solidi (RRL)–Rapid Research Letters 7 (9) (2013) 635–638.

[68] T. Roch, V. Weihnacht, H.-J. Scheibe, A. Roch, A. F. Lasagni, Direct laser interference patterning of tetrahedral amorphous carbon films for tribological applications, Diamond and Related Materials 33 (2013) 20–26.

[69] L. Guo, H.-B. Jiang, R.-Q. Shao, Y.-L. Zhang, S.-Y. Xie, J.-N. Wang, X.-B. Li, F. Jiang, Q.-D. Chen, T. Zhang, H.-B. Sun, Two-beam-laser interference mediated reduction, patterning and nanostructuring of graphene oxide for the production of a flexible humidity sensing device, Carbon 50 (4) (2012) 1667–1673.

[70] L. Guo, Y.-W. Hao, P.-L. Li, J.-F. Song, R.-Z. Yang, X.-Y. Fu, S.-Y. Xie, J. Zhao, Y.-L. Zhang, Improved NO_2 gas sensing properties of graphene oxide reduced by two-beam-laser interference, Scientific reports 8 (1) (2018) 4918.

[71] M. Birnbaum, Semiconductor surface damage produced by ruby lasers, Journal of Applied Physics 36 (11) (1965) 3688–3689.

[72] M. Huang, F. Zhao, Y. Cheng, N. Xu, Z. Xu, Origin of laser-induced near-subwavelength ripples: interference between surface plasmons and incident laser, ACS nano 3 (12) (2009) 4062–4070.

[73] R. Nemanich, D. Biegelsen, W. Hawkins, Aligned, coexisting liquid and solid regions in laser-annealed si, Physical Review B 27 (12) (1983) 7817.

[74] E. Granados, M. Martinez-Calderon, M. Gomez, A. Rodriguez, S. M. Olaizola, Photonic structures in diamond based on femtosecond UV laser induced periodic surface structuring (LIPSS), Optics Express 25 (13) (2017) 15330–15335.

[75] J. Bonse, A. Rosenfeld, J. Krüger, On the role of surface plasmon polaritons in the formation of laser-induced periodic surface structures upon irradiation of silicon by femtosecond-laser pulses, Journal of Applied Physics 106 (10) (2009) 104910.

[76] J. Bonse, S. Höhm, S. V. Kirner, A. Rosenfeld, J. Krüger, Laser-induced periodic surface structures-a scientific evergreen, IEEE Journal of Selected Topics in Quantum Electronics 23 (3) (2017) 109–123.

[77] J. Reif, F. Costache, M. Henyk, S. V. Pandelov, Ripples revisited: non-classical morphology at the bottom of femtosecond laser ablation craters in transparent dielectrics, Applied Surface Science 197 (2002) 891–895.

[78] A. Borowiec, H. Haugen, Subwavelength ripple formation on the surfaces of compound semiconductors irradiated with femtosecond laser pulses, Applied Physics Letters 82 (25) (2003) 4462–4464.

[79] R. Buividas, L. Rosa, R. Šliupas, T. Kudrius, G. Šlekys, V. Datsyuk, S. Juodkazis, Mechanism of fine ripple formation on surfaces of (semi) transparent materials via a half-wavelength cavity feedback, Nanotechnology 22 (5) (2010) 055304.

[80] X. Wang, C. A. Ohlin, Q. Lu, J. Hu, Cell directional migration and oriented division on three-dimensional laser-induced periodic surface structures on polystyrene, Biomaterials 29 (13) (2008) 2049–2059.

[81] B. Wu, M. Zhou, J. Li, X. Ye, G. Li, L. Cai, Superhydrophobic surfaces fabricated by microstructuring of stainless steel using a femtosecond laser, Applied Surface Science 256 (1) (2009) 61–66.

[82] A. A. Ionin, S. I. Kudryashov, S. V. Makarov, L. V. Seleznev, D. V. Sinitsyn, E. V. Golosov, A. G. Ol'ga, Y. R. Kolobov, A. E. Ligachev, Femtosecond laser color marking of metal and semiconductor surfaces, Applied Physics A 107 (2) (2012) 301–305.

[83] X. Chen, Y. Shen, W. Zhang, J. Zhang, D. Wei, R. Lu, L. Zhu, H. Li, Y. Shen, In-situ growth of ZnO nanowire arrays on the sensing electrode via a facile hydrothermal route for high-performance NO_2 sensor, Applied Surface Science 435 (2018) 1096–1104.

[84] J. Zeng, M. Hu, W. Wang, H. Chen, Y. Qin, NO_2-sensing properties of porous WO_3 gas sensor based on anodized sputtered tungsten thin film, Sensors and Actuators B: Chemical 161 (1) (2012) 447–452.

[85] H. Lüth, H. Lèuth, Solid surfaces, interfaces and thin films, Vol. 4, Springer, 2001.

[86] J. Lagowski, E. Sproles Jr, H. Gatos, Quantitative study of the charge transfer in chemisorption; oxygen chemisorption on ZnO, Journal of Applied Physics 48 (8) (1977) 3566–3575.

[87] K. Wetchakun, T. Samerjai, N. Tamaekong, C. Liewhiran, C. Siriwong, V. Kruefu, A. Wisitsoraat, A. Tuantranont, S. Phanichphant, Semiconducting metal oxides as sensors for environmentally hazardous gases, Sensors and Actuators B: Chemical 160 (1) (2011) 580–591.

[88] B. Ruhland, T. Becker, G. Müller, Gas-kinetic interactions of nitrous oxides with SnO_2 surfaces, Sensors and Actuators B: Chemical 50 (1) (1998) 85–94.

[89] S. Sharma, M. Madou, A new approach to gas sensing with nanotechnology, Phil. Trans. R. Soc. A 370 (1967) (2012) 2448–2473.

[90] W.-Y. Li, L.-N. Xu, J. Chen, Co_3O_4 nanomaterials in lithium-ion batteries and gas sensors, Advanced Functional Materials 15 (5) (2005) 851–857.

[91] K. Schneider, M. Lubecka, A. Czapla, V_2O_5 thin films for gas sensor applications, Sensors and Actuators B: Chemical 236 (2016) 970–977.

[92] C. Bunn, The lattice-dimensions of zinc oxide, Proceedings of the Physical Society 47 (5) (1935) 835.

[93] G. Zonta, G. Anania, B. Fabbri, A. Gaiardo, S. Gherardi, A. Giberti, V. Guidi, N. Landini, C. Malagù, Detection of colorectal cancer biomarkers in the presence of interfering gases, Sensors and Actuators B: Chemical 218 (2015) 289–295.

[94] M. Law, L. E. Greene, J. C. Johnson, R. Saykally, P. Yang, Nanowire dye-sensitized solar cells, Nature materials 4 (6) (2005) 455.

[95] A. P. Chatterjee, P. Mitra, A. K. Mukhopadhyay, Chemically deposited zinc oxide thin film gas sensor, Journal of Materials Science 34 (17) (1999) 4225–4231.

[96] B. Fabbri, A. Gaiardo, A. Giberti, V. Guidi, C. Malagù, A. Martucci, M. Sturaro, G. Zonta, S. Gherardi, P. Bernardoni, Chemoresistive properties of photo-activated thin and thick ZnO films, Sensors and Actuators B: Chemical 222 (2016) 1251–1256.

[97] M. C. Carotta, A. Cervi, A. Fioravanti, S. Gherardi, A. Giberti, B. Vendemiati, D. Vincenzi, M. Sacerdoti, A novel ozone detection at room temperature through UV-LED-assisted ZnO thick film sensors, Thin Solid Films 520 (3) (2011) 939–946.

[98] J. Gonzalez-Chavarri, L. Parellada-Monreal, I. Castro-Hurtado, E. Castaño, G. G. Mandayo, ZnO nanoneedles grown on chip for selective NO_2 detection indoors, Sensors and Actuators B: Chemical 255 (2018) 1244–1253.

[99] H. Hamrouni, I. Jaouali, M. Nsib, E. Fazio, F. Neri, A. Bonavita, S. Leonardi, G. Neri, Sunflower pollen-assisted synthesis of nanosized semiconducting ZnO and its application in the selective sensing of NO_2, Journal of Materials Science: Materials in Electronics (2018) 1–8.

[100] M. Jiao, N. V. Chien, N. Van Duy, N. D. Hoa, N. Van Hieu, K. Hjort, H. Nguyen, On-chip hydrothermal growth of ZnO nanorods at low temperature for highly selective NO_2 gas sensor, Materials Letters 169 (2016) 231–235.

[101] A. Janotti, C. G. Van de Walle, Fundamentals of zinc oxide as a semiconductor, Reports on progress in physics 72 (12) (2009) 126501.

[102] R. Kumar, O. Al-Dossary, G. Kumar, A. Umar, Zinc oxide nanostructures for NO_2 gas–sensor applications: A review, Nano-Micro Letters 7 (2) (2015) 97–120.

[103] K. Ellmer, A. Klein, B. Rech, Transparent Conductive Zinc Oxide: Basics and Applications in Thin Film Solar Cells. Springer Series in Materials Science, 104, Springer, 2008.

[104] N. Han, X. Wu, L. Chai, H. Liu, Y. Chen, Counterintuitive sensing mechanism of ZnO nanoparticle based gas sensors, Sensors and Actuators B: Chemical 150 (1) (2010) 230–238.

[105] Y. Zhang, J. Xu, Q. Xiang, H. Li, Q. Pan, P. Xu, Brush-like hierarchical ZnO nanostructures: synthesis, photoluminescence and gas sensor properties, The Journal of Physical Chemistry C 113 (9) (2009) 3430–3435.

[106] C. Li, L. Li, Z. Du, H. Yu, Y. Xiang, Y. Li, Y. Cai, T. Wang, Rapid and ultrahigh ethanol sensing based on Au-coated ZnO nanorods, Nanotechnology 19 (3) (2007) 035501.

[107] C. G. Granqvist, Electrochromic tungsten oxide films: review of progress 1993–1998, Solar Energy Materials and Solar Cells 60 (3) (2000) 201–262.

[108] V. Shapovalov, A. Lapshin, A. Komlev, A. Komlev, Crystallization and thermochromism in tungsten oxide films annealed in vacuum, Technical Physics Letters 38 (6) (2012) 555–558.

[109] S. Yamamoto, T. Hakoda, A. Miyashita, M. Yoshikawa, Structural and gasochromic properties of WO_3 films prepared by reactive sputtering deposition, Materials Research Express 2 (2) (2015) 026401.

[110] H. Zheng, Y. Tachibana, K. Kalantar-zadeh, Dye-sensitized solar cells based on WO_3, Langmuir 26 (24) (2010) 19148–19152.

[111] H. Zheng, J. Z. Ou, M. S. Strano, R. B. Kaner, A. Mitchell, K. Kalantar-zadeh, Nanostructured tungsten oxide–properties, synthesis, and applications, Advanced Functional Materials 21 (12) (2011) 2175–2196.

[112] P. Woodward, A. Sleight, T. Vogt, Ferroelectric tungsten trioxide, Journal of Solid State Chemistry 131 (1) (1997) 9–17.

[113] R. Diehl, G. Brandt, E. Saije, The crystal structure of triclinic WO_3, Acta Crystallographica Section B 34 (4) (1978) 1105–1111.

[114] T. Vogt, P. M. Woodward, B. A. Hunter, The high-temperature phases of WO_3, Journal of Solid State Chemistry 144 (1) (1999) 209–215.

[115] E. Salje, The orthorhombic phase of WO_3, Acta Crystallographica Section B 33 (2) (1977) 574–577.

[116] W. Kehl, R. Hay, D. Wahl, The structure of tetragonal tungsten trioxide, Journal of Applied Physics 23 (2) (1952) 212–215.

[117] I. M. Szilágyi, S. Saukko, J. Mizsei, A. L. Tóth, J. Madarász, G. Pokol, Gas sensing selectivity of hexagonal and monoclinic WO_3 to H_2S, Solid State Sciences 12 (11) (2010) 1857–1860.

[118] L. S. Pilotto, R. M. Douglas, R. G. Attewell, S. R. Wilson, Respiratory effects associated with indoor nitrogen dioxide exposure in children., International Journal of Epidemiology 26 (4) (1997) 788–796.

[119] S. A. Abdul-Wahab, S. C. F. En, A. Elkamel, L. Ahmadi, K. Yetilmezsoy, A review of standards and guidelines set by international bodies for the parameters of indoor air quality, Atmospheric Pollution Research 6 (5) (2015) 751–767.

[120] Recommendation from the scientific committee on occupational exposure limits for nitrogen dioxide.

[121] M. Epifani, J. D. Prades, E. Comini, E. Pellicer, M. Avella, P. Siciliano, G. Faglia, A. Cirera, R. Scotti, F. Morazzoni, et al., The role of surface oxygen vacancies in the NO_2 sensing properties of SnO_2 nanocrystals, The Journal of Physical Chemistry C 112 (49) (2008) 19540–19546.

[122] J. Tamaki, M. Nagaishi, Y. Teraoka, N. Miura, N. Yamazoe, K. Moriya, Y. Nakamura, Adsorption behavior of CO and interfering gases on SnO_2, Surface science 221 (1-2) (1989) 183–196.

[123] M. Hjiri, L. El Mir, S. G. Leonardi, N. Donato, G. Neri, CO and NO_2 selective monitoring by ZnO-based sensors, Nanomaterials 3 (3) (2013) 357–369.

[124] A. Tamvakos, K. Korir, D. Tamvakos, D. Calestani, G. Cicero, D. Pullini, NO_2 gas sensing mechanism of ZnO thin-film transducers: physical experiment and theoretical correlation study, ACS Sensors 1 (4) (2016) 406–412.

[125] M. Chen, Z. Wang, D. Han, F. Gu, G. Guo, High-sensitivity NO_2 gas sensors based on flower-like and tube-like ZnO nanomaterials, Sensors and Actuators B: Chemical 157 (2) (2011) 565–574.

[126] C. Zhang, M. Debliquy, A. Boudiba, H. Liao, C. Coddet, Sensing properties of atmospheric plasma-sprayed WO_3 coating for sub-ppm NO_2 detection, Sensors and Actuators B: Chemical 144 (1) (2010) 280–288.

[127] Y. Qin, Z. Ye, DFT study on interaction of NO_2 with the vacancy-defected WO_3 nanowires for gas-sensing, Sensors and Actuators B: Chemical 222 (2016) 499–507.

[128] C. Cantalini, L. Lozzi, M. Passacantando, S. Santucci, The comparative effect of two different annealing temperatures and times on the sensitivity and long-term stability of WO_3 thin films for detecting NO_2, IEEE Sensors Journal 3 (2) (2003) 171–179.

[129] N. Yamazoe, K. Shimanoe, Receptor function and response of semiconductor gas sensor, Journal of sensors 2009.

[130] D. Barreca, D. Bekermann, E. Comini, A. Devi, R. A. Fischer, A. Gasparotto, C. Maccato, C. Sada, G. Sberveglieri, E. Tondello, Urchin-like ZnO nanorod arrays for gas sensing applications, CrystEngComm 12 (11) (2010) 3419–3421.

[131] F. Fan, Y. Feng, S. Bai, J. Feng, A. Chen, D. Li, Synthesis and gas sensing properties to NO_2 of ZnO nanoparticles, Sensors and Actuators B: Chemical 185 (2013) 377–382.

[132] M.-W. Ahn, K.-S. Park, J.-H. Heo, J.-G. Park, D.-W. Kim, K. J. Choi, J.-H. Lee, S.-H. Hong, Gas sensing properties of defect-controlled ZnO-nanowire gas sensor, Applied physics letters 93 (26) (2008) 263103.

[133] W. An, X. Wu, X. C. Zeng, Adsorption of O_2, H_2, CO, NH_3, and NO_2 on ZnO nanotube: a density functional theory study, The Journal of Physical Chemistry C 112 (15) (2008) 5747–5755.

[134] D. Zappa, E. Comini, G. Sberveglieri, Thermally oxidized zinc oxide nanowires for use as chemical sensors, Nanotechnology 24 (44) (2013) 444008.

[135] M. Procek, A. Stolarczyk, T. Pustelny, Impact of temperature and UV irradiation on dynamics of NO_2 sensors based on ZnO nanostructures, Nanomaterials 7 (10) (2017) 312.

[136] V. L. Patil, S. A. Vanalakar, P. S. Patil, J. H. Kim, Fabrication of nanostructured ZnO thin films based NO_2 gas sensor via SILAR technique, Sensors and Actuators B: Chemical 239 (2017) 1185–1193.

[137] X. Wang, F. Sun, Y. Duan, Z. Yin, W. Luo, Y. Huang, J. Chen, Highly sensitive, temperature-dependent gas sensor based on hierarchical ZnO nanorod arrays, Journal of Materials Chemistry C 3 (43) (2015) 11397–11405.

[138] H. Van Han, N. D. Hoa, P. Van Tong, H. Nguyen, N. Van Hieu, Single-crystal zinc oxide nanorods with nanovoids as highly sensitive NO_2 nanosensors, Materials Letters 94 (2013) 41–43.

[139] S. An, S. Park, H. Ko, C. Jin, W. I. Lee, C. Lee, Enhanced gas sensing properties of branched ZnO nanowires, Thin Solid Films 547 (2013) 241–245.

[140] M. Z. Ahmad, J. Chang, M. S. Ahmad, E. R. Waclawik, W. Wlodarski, Non-aqueous synthesis of hexagonal ZnO nanopyramids: gas sensing properties, Sensors and Actuators B: Chemical 177 (2013) 286–294.

[141] J. Tamaki, Z. Zhang, K. Fujimori, M. Akiyama, T. Harada, N. Miura, N. Yamazoe, Grain-size effects in tungsten oxide-based sensor for nitrogen oxides, Journal of the Electrochemical Society 141 (8) (1994) 2207–2210.

[142] J.-S. Kim, J.-W. Yoon, Y. J. Hong, Y. C. Kang, F. Abdel-Hady, A. Wazzan, J.-H. Lee, Highly sensitive and selective detection of ppb-level NO_2 using multi-shelled WO_3 yolk–shell spheres, Sensors and Actuators B: Chemical 229 (2016) 561–569.

[143] H. G. Moon, S. D. Han, M.-G. Kang, W.-S. Jung, B. Kwon, C. Kim, T. Lee, S. Lee, S.-H. Baek, J.-S. Kim, et al., Glancing angle deposited WO_3 nanostructures for enhanced sensitivity and selectivity to NO_2 in gas mixture, Sensors and Actuators B: Chemical 229 (2016) 92–99.

[144] C. Wang, R. Sun, X. Li, Y. Sun, P. Sun, F. Liu, G. Lu, Hierarchical flower-like WO_3 nanostructures and their gas sensing properties, Sensors and Actuators B: Chemical 204 (2014) 224–230.

[145] B. Xiao, D. Wang, F. Wang, Q. Zhao, C. Zhai, M. Zhang, Preparation of hierarchical WO_3 dendrites and their applications in NO_2 sensing, Ceramics International 43 (11) (2017) 8183–8189.

[146] L. Han, J. Chen, Y. Zhang, Y. Liu, L. Zhang, S. Cao, Facile synthesis of hierarchical carpet-like WO_3 microflowers for high NO_2 gas sensing performance, Materials Letters 210 (2018) 8–11.

[147] A. K. Zak, W. A. Majid, M. E. Abrishami, R. Yousefi, X-ray analysis of zno nanoparticles by Williamson–Hall and size–strain plot methods, Solid State Sciences 13 (1) (2011) 251–256.

[148] Z. Fang, Z. Yan, Y. Tan, X. Liu, Y. Wang, Influence of post-annealing treatment on the structure properties of ZnO films, Applied Surface Science 241 (3) (2005) 303–308.

[149] M. Puchert, P. Timbrell, R. Lamb, Postdeposition annealing of radio frequency magnetron sputtered ZnO films, Journal of Vacuum Science & Technology A: Vacuum, Surfaces, and Films 14 (4) (1996) 2220–2230.

[150] A. Moustaghfir, E. Tomasella, S. B. Amor, M. Jacquet, J. Cellier, T. Sauvage, Structural and optical studies of thin films deposited by RF magnetron sputtering: Influence of annealing, Surface and Coatings Technology 174 (2003) 193–196.

[151] J. Berger, T. Roch, S. Correia, J. Eberhardt, A. F. Lasagni, Controlling the optical performance of transparent conducting oxides using direct laser interference patterning, Thin Solid Films 612 (2016) 342–349.

[152] M. D'alessandria, A. Lasagni, F. Mücklich, Direct micro-patterning of aluminum substrates via laser interference metallurgy, Applied Surface Science 255 (5) (2008) 3210–3216.

[153] N. B. Dahotre, Lasers in surface engineering, Vol. 1, ASM international, 1998.

[154] Y. G. Wang, S. P. Lau, H. W. Lee, S. F. Yu, B. K. Tay, X. H. Zhang, K. Y. Tse, H. H. Hng, Comprehensive study of ZnO films prepared by filtered cathodic vacuum arc at room temperature, Journal of Applied Physics 94 (3) (2003) 1597–1604.

[155] O. Lupan, T. Pauporté, L. Chow, B. Viana, F. Pellé, L. K. Ono, B. Roldan Cuenya, H. Heinrich, Effects of annealing on properties of ZnO thin films prepared by electrochemical deposition in chloride medium, Applied Surface Science 256 (6) (2010) 1895–1907.

[156] M. Bieda, M. Siebold, A. F. Lasagni, Fabrication of sub-micron surface structures on copper, stainless steel and titanium using picosecond laser interference patterning, Applied Surface Science 387 (2016) 175–182.

[157] D. W. Green, R. H. Perry, Perry's Chemical Engineers' Handbook, no. C 660.28 P47 2008., 1973.

[158] M. Arafat, B. Dinan, S. A. Akbar, A. Haseeb, Gas sensors based on one dimensional nanostructured metal-oxides: a review, Sensors 12 (6) (2012) 7207–7258.

[159] J. N. Reddy, An Introduction to The Finite Element Method, 3rd Edition, New York, 1993.

[160] N. Nedyalkov, M. Koleva, R. Nikov, P. Atanasov, Y. Nakajima, A. Takami, A. Shibata, M. Terakawa, Laser nanostructuring of ZnO thin films, Applied Surface Science 374 (2015) 172–176.

[161] R. Naeem, R. Yahya, A. Pandikumar, H. N. Ming, M. Mazhar, Optical and optoelectronic properties of morphology and structure controlled ZnO, CdO and PbO thin films deposited by electric field directed aerosol assisted CVD, Journal of Materials Science: Materials in Electronics 28 (1) (2017) 868–877.

[162] J. T. Li, V. Maurice, J. Swiatowska-Mrowiecka, A. Seyeux, S. Zanna, L. Klein, S. G. Sun, P. Marcus, XPS, time-of-flight-SIMS and polarization modulation IRRAS study of Cr_2O_3 thin film materials as anode for lithium ion battery, Electrochimica Acta 54 (14) (2009) 3700–3707.

[163] L. Zhang, J. Zhao, H. Lu, L. Gong, L. Li, J. Zheng, H. Li, Z. Zhu, High sensitive and selective formaldehyde sensors based on nanoparticle-assembled ZnO micro-octahedrons synthesized by homogeneous precipitation method, Sensors and Actuators, B: Chemical 160 (1) (2011) 364–370.

[164] K. G. Saw, K. Ibrahim, Y. T. Lim, M. K. Chai, Self-compensation in ZnO thin films: An insight from X-ray photoelectron spectroscopy, Raman spectroscopy and time-of-flight secondary ion mass spectroscopy analyses, Thin Solid Films 515 (5) (2007) 2879–2884.

[165] X. Li, Y. Wang, W. Liu, G. Jiang, C. Zhu, Study of oxygen vacancies' influence on the lattice parameter in ZnO thin film, Materials Letters 85 (2012) 25–28.

[166] T. P. Rao, M. S. Kumar, A. Safarulla, V. Ganesan, S. Barman, C. Sanjeeviraja, Physical properties of ZnO thin films deposited at various substrate temperatures using spray pyrolysis, Physica B: Condensed Matter 405 (9) (2010) 2226–2231.

[167] O. Kappertz, R. Drese, M. Wuttig, Correlation between structure, stress and deposition parameters in direct current sputtered zinc oxide films, Journal of Vacuum Science & Technology A: Vacuum, Surfaces, and Films 20 (6) (2002) 2084–2095.

[168] T. Tsuji, M. Hirohashi, Influence of oxygen partial pressure on transparency and conductivity of RF sputtered Al-doped ZnO thin films, Applied surface science 157 (1) (2000) 47–51.

[169] J. Alda, Laser and gaussian beam propagation and transformation, Vol. 2013, 2003, pp. 999–1013.

[170] P. Feng, L. Jiang, X. Li, K. Zhang, X. Shi, B. Li, Y. Lu, Femtosecond laser-induced subwavelength ripples formed by asymmetrical grating splitting, Applied Surface Science 372 (2016) 52–56.

[171] X. D. Guo, R. X. Li, Y. Hang, Z. Z. Xu, B. K. Yu, H. L. Ma, X. W. Sun, Raman spectroscopy and luminescent properties of ZnO nanostructures fabricated by femtosecond laser pulses, Materials letters 61 (23-24) (2007) 4583–4586.

[172] X. D. Guo, R. X. Li, Y. Hang, Z. Z. Xu, B. K. Yu, Y. Dai, B. Lu, X. W. Sun, Coherent linking of periodic nano-ripples on a ZnO crystal surface induced by femtosecond laser pulses, Applied Physics A: Materials Science and Processing 94 (2) (2009) 423–426.

[173] M. Zamfirescu, M. Ulmeanu, F. Jipa, O. Cretu, A. Moldovan, G. Epurescu, M. Dinescu, R. Dabu, Femtosecond laser induced periodic surface structures on ZnO thin films, Journal of Laser Micro Nanoengineering 4 (1) (2009) 7–10.

[174] C. Bundesmann, N. Ashkenov, M. Schubert, D. Spemann, T. Butz, E. Kaidashev, M. Lorenz, M. Grundmann, Raman scattering in ZnO thin films doped with Fe, Sb, Al, Ga, and Li, Applied Physics Letters 83 (10) (2003) 1974–1976.

[175] G. J. Exarhos, S. K. Sharma, Influence of processing variables on the structure and properties of ZnO films, Thin Solid Films 270 (1-2) (1995) 27–32.

[176] H. Fan, R. Scholz, F. Kolb, M. Zacharias, U. Gösele, F. Heyroth, C. Eisenschmidt, T. Hempel, J. Christen, On the growth mechanism and optical properties of ZnO multi-layer nanosheets, Applied Physics A 79 (8) (2004) 1895–1900.

[177] P. Xiong, T. Jia, X. Jia, D. Feng, S. Zhang, L. Ding, Z. Sun, J. Qiu, Z. Xu, Ultraviolet luminescence enhancement of zno two-dimensional periodic nanostructures fabricated by the interference of three femtosecond laser beams, New Journal of Physics 13 (2) (2011) 023044.

[178] G. Pawley, Unit-cell refinement from powder diffraction scans, Journal of Applied Crystallography 14 (6) (1981) 357–361.

[179] A. Le Bail, H. Duroy, J. Fourquet, Ab-initio structure determination of $LiSbWO_6$ by X-ray powder diffraction, Materials Research Bulletin 23 (3) (1988) 447–452.

[180] Bruker AXS GmbH. Karlsruhe, Germany, Bruker AXS. TOPAS 4-1, User Manual.

[181] R. W. Cheary, A. Coelho, A fundamental parameters approach to X-ray line-profile fitting, Journal of Applied Crystallography 25 (2) (1992) 109–121.

[182] R. W. Cheary, A. A. Coelho, J. P. Cline, Fundamental parameters line profile fitting in laboratory diffractometers, Journal of Research of the National Institute of Standards and Technology 109 (1) (2004) 1.

[183] E. J. Mittemeijer, P. Scardi, Diffraction analysis of the microstructure of materials, Vol. 68, Springer Science & Business Media, 2013.

[184] D. Balzar, Voigt-function model in diffraction line-broadening analysis, International union of crystallography monographs on crystallography 10 (1999) 94–126.

[185] R. Catrin, A. F. Lasagni, C. Gachot, U. Schmid, F. Mücklich, Microstructural design of advanced architectures in titanium/platinum thin films by laser interference metallurgy, Advanced Engineering Materials 10 (5) (2008) 466–470.

[186] G. Korotcenkov, The role of morphology and crystallographic structure of metal oxides in response of conductometric-type gas sensors, Materials Science and Engineering: R: Reports 61 (1-6) (2008) 1–39.

[187] M. Boulova, G. Lucazeau, Crystallite nanosize effect on the structural transitions of WO_3 studied by Raman spectroscopy, Journal of Solid State Chemistry 167 (2) (2002) 425–434.

[188] Y. Zou, Y. Zhang, D. Lou, H. Wang, L. Gu, Y. Dong, K. Dou, X. Song, H. Zeng, Structural and optical properties of WO_3 films deposited by pulsed laser deposition, Journal of Alloys and Compounds 583 (2014) 465–470.

[189] V. Shapovalov, A. Komlev, V. Vitḱo, A. Zavýalov, A. Lapshin, S. Moshkalev, V. Ermakov, Influence of annealing on the optical properties and chemical and phase compositions of tungsten-oxide films, Journal of Surface Investigation. X-ray, Synchrotron and Neutron Techniques 10 (5) (2016) 1077–1086.

[190] W. Wu, Q. Yu, J. Lian, J. Bao, Z. Liu, S.-S. Pei, Tetragonal tungsten oxide nanobelts synthesized by chemical vapor deposition, Journal of Crystal Growth 312 (21) (2010) 3147–3150.

[191] Y.-K. Chung, M.-H. Kim, W.-S. Um, H.-S. Lee, J.-K. Song, S.-C. Choi, K.-M. Yi, M.-J. Lee, K.-W. Chung, Gas sensing properties of WO_3 thick film for NO_2 gas dependent on process condition, Sensors and Actuators B: Chemical 60 (1) (1999) 49–56.

[192] I. Castro-Hurtado, J. Gonzalez-Chavarri, S. Morandi, J. Sama, A. Romano-Rodriguez, E. Castano, G. G. Mandayo, Formaldehyde sensing mechanism of SnO_2 nanowires grown on-chip by sputtering techniques, RSC Adv. 6 (22) (2016) 18558–18566.

[193] J. Samà, S. Barth, G. Domènech-Gil, J.-D. Prades, N. López, O. Casals, I. Gràcia, C. Cané, A. Romano-Rodríguez, Site-selectively grown SnO_2 NWs networks on micromembranes for efficient ammonia sensing in humid conditions, Sensors and Actuators B: Chemical 232 (2016) 402–409.

[194] T. Jia, M. Baba, M. Suzuki, R. A. Ganeev, H. Kuroda, J. Qiu, X. Wang, R. Li, Z. Xu, Fabrication of two-dimensional periodic nanostructures by two-beam interference of femtosecond pulses, Optics express 16 (3) (2008) 1874–1878.

Appendix A

Journal articles and conferences contributions

This appendix contains the scientific contributions published upon the development of this thesis. In particular, three articles were published in high impact scientific journals and another one is currently under review. Four oral presentations and six poster contributions were presented in international and national scientific conferences.

- **Journal articles**

    (i) L. Parellada-Monreal, I. Castro-Hurtado, M. Martínez-Calderón, L. Presmanes & G. G. Mandayo (2019). *Laser-induced periodic surface structures on ZnO thin film for high response NO_2 detection.* Applied Surface Science, 476, 569-575.

    (ii) L. Parellada-Monreal, I. Castro-Hurtado, M. Martínez-Calderón, A. Rodriguez, S. M. Olaizola, D. Gamarra, J. Lozano & G. G. Mandayo (2018). *Study of sputtered ZnO modified by Direct Laser Interference Patterning: Structural characterization and temperature simulation.* Applied Surface Science, 441, 331-340.

    (iii) J. Gonzalez-Chavarri, L. Parellada-Monreal, I. Castro-Hurtado, E. Castaño & G. G. Mandayo (2018). *ZnO nanoneedles grown on chip for selective NO_2 detection indoors.* Sensors and Actuators B: Chemical, 255, 1244-1253.

    (iv) L. Parellada-Monreal, S. Gherardi, G. Zonta, C. Malagù, D. Casotti, G. Cruciani, V. Guidi, M. Martínez-Calderón, I. Castro-Hurtado, D. Gamarra, J. Lozano, L. Presmanes & G. G. Mandayo. *WO_3 processed by direct laser interference patterning for NO_2 detection.* Submitted to Sensors and Actuators B: Chemical.

- **Conferences contributions**
    Oral presentations

    (i) L. Parellada-Monreal, M. Martínez-Calderón, A. Rodriguez, M. Gomez-Aranzadi, S. M. Olaizola, I. Castro-Hurtado, I. Ayerdi, E. Castaño & G. G. Mandayo.

Semiconductor oxide surfaces modified by LIL for pollutant detection, E-MRS Spring meeting, 2-6 May 2016, Lille (France).

(ii) L. Parellada-Monreal, M. Martínez-Calderón, I. Castro-Hurtado, D. Gamarra, J. Lozano, A. Rodriguez, S. M. Olaizola & G. G. Mandayo. *Laser-modified ZnO for Conductometric Sensors*, 8th Franco-Spanish Workshop IBERNAM-CMC2, 13-14 October 2016, Toulouse (France).

(iii) G. G. Mandayo, J. Gonzalez-Chavarri, E. A. Hammes, L. Parellada-Monreal, I. Castro-Hurtado, E. Castaño, I. Ayerdi & H. Knapp. *Multisensor platform for indoor air quality*, 11th Spanish Conference on Electron Devices, 8-10 February 2017, Barcelona (Spain).

(iv) L. Parellada-Monreal, M. Martínez-Calderón, I. Castro-Hurtado, D. Gamarra, J. Lozano, A. Rodriguez, S. M. Olaizola & G. G. Mandayo. *Surface and in depth characterization of thin film ZnO processed by Direct Laser Interference Patterning*, 9th Franco-Spanish Workshop IBERNAM-CMC2, 4-5 October 2018, Tarragona (Spain).

Posters

(i) L. Parellada-Monreal, M. Martínez-Calderón, I. Castro-Hurtado, A. Rodriguez, S. M. Olaizola, M. Gomez-Aranzadi, I. Ayerdi, E. Castaño & G. G. Mandayo. *Temperature simulation at ZnO surface processed by Laser Interference Lithography*, SPIE MICROTECHNOLOGIES, 8-10 May 2017, Barcelona (Spain).

(ii) M. Moreno-Serrano, N. Pérez, G. Domènech-Gil, L. Parellada-Monreal, M. Martínez-Calderón, M. Gomez-Aranzadi, N. Darwish, G. G. Mandayo & A. Romano-Rodriguez. *Fabrication of broad area optical nanostructures for high throughput chemical sensing*, Eurosensors XXXI, 3-6 September 2017, Paris (France).

(iii) L. Parellada-Monreal, M. Martínez-Calderón, I. Castro-Hurtado, A. Rodriguez & G. G. Mandayo. *Laser-induced periodic surface structures on ZnO thin film for NO_2 detection*, Workshop IBERNAM, 28-29 September 2017, Tordesillas (Spain).

(iv) L. Parellada-Monreal, M. Martínez-Calderón, I. Castro-Hurtado, S. M. Olaizola, G. Zonta, S. Gherardi, C. Malagù & G. G. Mandayo. *Enhancement of gas sensing response on WO_3 thin films processed by Direct Laser Interference Patterning*, Eurosensors XXXII, 9-12 September 2018, Graz (Austria).

(v) C. Cané, S. Vallejos, M. Salleras, M. Tomic, E. Figueras, I. Gràcia, G. Domènech-Gil, E. López-Aymerich, M. Moreno, P. Pellegrino, A. Romano-Rodríguez, L. Parellada-Monreal, I. Castro-Hurtado, I. Ayerdi & G. G. Mandayo. *Nanostructured MOX materials for gas sensors applied to environment*, 11th Ibero-American Congress on Sensors, 17-20 September 2018, Barcelona (Spain).

(vi) L. Parellada-Monreal, I. Castro-Hurtado, M. Martínez-Calderón, S. M. Olaizola & G. G. Mandayo. *ZnO thin film processed by direct laser interference patterning for formaldehyde detection*, 12th Spanish Conference on Electron Devices, 14-16 November 2018, Salamanca (Spain).
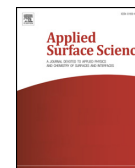
A.1   Journal articles

Full Length Article

Laser-induced periodic surface structures on ZnO thin film for high response NO$_2$ detection

L. Parellada-Monreal[a,b], I. Castro-Hurtado[a,b], M. Martínez-Calderón[a,b], L. Presmanes[c], G.G. Mandayo[a,b,*]

[a] Ceit, Manuel Lardizábal 15, 20018 Donostia/San Sebastián, Spain
[b] Universidad de Navarra, Tecnun, Manuel Lardizábal 13, 20018 Donostia/San Sebastián, Spain
[c] CIRIMAT, Université de Toulouse, CNRS, INPT, UPS, Toulouse Cedex 9, France

ARTICLE INFO

ABSTRACT

Femtosecond laser-induced periodic structures (LIPSS) have been processed on ZnO thin film gas sensor devices for nitrogen dioxide (NO$_2$) detection. From the morphology point of view, the nanostructures have been identified as high spatial frequency LIPSS (HSFL) with an average period of 145 nm. Through Raman analysis, a decrease of the typical wurtzite ZnO structure is shown, with a possible increase of defects such as Zn interstitials. The response under NO$_2$ is enhanced if compared with the only-annealed ZnO thin film for concentrations as low as 1 ppm, reaching 1 ppb of detection limit (LOD) for the sensors with LIPSS. The Zn interstitials defects could be the source of the adsorbed NO$_2$ species increasing the sensitivity. Reproducible results have been measured during 11 weeks in a row.

Full Length Article

Study of sputtered ZnO modified by Direct Laser Interference Patterning: Structural characterization and temperature simulation

L. Parellada-Monreal [a], I. Castro-Hurtado [a], M. Martínez-Calderón [a], A. Rodriguez [a], S.M. Olaizola [a], D. Gamarra [b], J. Lozano [b], G.G. Mandayo [a],*

[a] CEIT and Tecnun, University of Navarra, San Sebastián, Spain
[b] Escuela de Ingenierías Industriales, University of Extremadura, Badajoz, Spain

ARTICLE INFO

ABSTRACT

ZnO thin film sputtered on alumina substrate is processed by Direct Laser Interference Patterning (DLIP). The heat transfer equation has been simulated for interference patterns with a period of 730 nm and two different fluences (85 mJ/cm^2 and 165 mJ/cm^2). A thermal threshold of 900 K, where crystal modification occurs has been calculated, indicating a lateral and depth processing around 173 nm and 140 nm, respectively. The experimentally reproduced samples have been analyzed from the structural and composition point of view and compared to conventional thermal treatments at three different temperatures (600 °C, 700 °C and 800 °C). Promising properties have been observed for the laser treated samples, such as low influence on the thin film/substrate interface, an improvement of the crystallographic structure, as well as a decrease of the oxygen content from O/Zn = 2.10 to 1.38 for the highest fluence, getting closer to the stoichiometry. The DLIP characteristics could be suitable for the replacement of annealing process in the case of substrates that cannot achieve high temperatures as most of flexible substrates.

Contents lists available at ScienceDirect

Sensors and Actuators B: Chemical

journal homepage: www.elsevier.com/locate/snb

Research Paper

ZnO nanoneedles grown on chip for selective NO$_2$ detection indoors

Jurgi Gonzalez-Chavarri, Laura Parellada-Monreal, Irene Castro-Hurtado,
Enrique Castaño, Gemma G. Mandayo*

Ceit & Tecnun, Donostia-San Sebastian, Spain

ARTICLE INFO

ABSTRACT

A conductometric sensor based on ZnO nanoneedles for the detection of NO$_2$ is described. The material is grown on chip over Pt interdigitated electrodes patterned on alumina substrates without the need of a catalyst layer. The nanostructure growth relies on two different mechanisms (Vapor–Solid and Liquid–Solid) so nanoneedles with few μm of length and wurtzite structure are obtained. The procedure is optimized on chip, which supposes a significant advantage in the fabrication of nanostructures on sensing devices. The sensor response has been measured under a target gas (NO$_2$) and two interfering pollutants (benzene and formaldehyde). Lower working temperatures than other pure ZnO nanostructures found in the literature have been achieved and limit of detection (LOD) in the order of ppb has been reached. The significant higher response to NO$_2$ with respect to benzene and formaldehyde makes this sensing device suitable for selective NO$_2$ detection indoors.

WO$_3$ processed by direct laser interference patterning for NO$_2$ detection

L. Parellada-Monreal[a,b,*], S. Gherardi[c], G. Zonta[c,d], C. Malagù[c,d],
D. Casotti[d,e], G. Cruciani[d], V. Guidi[d,e], M. Martínez-Calderón[a,b],
I. Castro-Hurtado[a,b], D. Gamarra[f], J. Lozano[f], L. Presmanes[g],
G. G. Mandayo[a,b]

[a]*1Ceit, Manuel Lardizabal 15, 20018 Donostia / San Sebastián, Spain.*
[b]*Universidad de Navarra, Tecnun, Manuel Lardizabal 13, 20018 Donostia / San Sebastián, Spain*
[c]*SCENT, S.r.l., Ferrara, Italy*
[d]*Department of Physics and Earth Science, University of Ferrara, Via Saragat 1/c, 44122 Ferrara, Italy*
[e]*INFN section of Ferrara, Via Saragat 1/c, 44122 Ferrara, Italy*
[f]*Escuela de Ingenierías Industriales, University of Extremadura, Badajoz, Spain*
[g]*Institut Carnot CIRIMAT, UPS-INPT-CNRS 5085, University Paul Sabatier, Toulouse, France*

Abstract

In this paper two kind of sensors based on WO$_3$ sputtered by magnetron sputtering and 600 °C annealed have been studied. The first kind was processed by two-dimensional direct laser interfering patterning (DLIP) and the second without any additional treatment. Morphological and structural characterization have shown a hole structure in a periodic line-pattern for the DLIP-processed sensors while a flat surface for the only-annealed sensors, both with a tetragonal WO$_3$ phase. TOF-SIMS analysis has revealed that the first WO$_3$ layers are reduced for both samples, which could improve sensing performances. Promising response enhancement of DLIP-processed sensors have been observed for low concentrations of NO$_2$ (from 0.5 ppm to 5 ppm) at 200 °C, lowering the limit of detection (LOD) to 10 ppb, half of the LOD of the only-annealed sensors (20 ppb). Cross sensitivity to CO and HCHO have been investigated and the sensing mechanisms discussed.

*Corresponding author
Email address: `lparellada@ceit.es` (L. Parellada-Monreal)

A.2   Conference contributions

A.2.1   Oral presentations

(i) E-MRS Spring meeting, 2-6 May 2016, Lille (France)

Semiconductor oxide surfaces modified by laser interference lithography (LIL) for pollutant detection

L. Parellada-Monreal, I. Castro-Hurtado, E. Castaño, G. G. Mandayo

Ceit and Tecnun (University of Navarra)

Abstract

Metal oxide semiconductors and their different nanostructured forms have been widely researched in the last years. They show high interest to fabricate cheap chemoresistive gas sensing devices. Materials like ZnO, SnO_2, In_2O_3 or TiO_2 are well known for their cost-effectiveness, fast response and high sensitivity when exposed to target gases. As it is well known, chemoresistive gas sensors rely on the electric response caused by the gas on the material surface. The grain size and morphology of the material are also of great relevance in the gas sensing mechanism. Therefore, research efforts are focused on finding easy-to-implement and efficient fabrication routes, which at the same time give rise to an optimum morphology. In particular, several routes have been researched to obtain nanostructures. Some of them are bottom-up methods, such as the chemical vapor based routes such as the VL (vapor-liquid) or the VLS (vapor-liquid-solid) methods, widely reported to obtain nanowires, nanoneedles, nanobelts and other similar one dimensional nanostructures. But there are also some interesting top-down routes such as e-beam lithography or nano-imprint lithography. Among those, laser interference lithography is a technique that uses interference patterns generated from two or more coherent laser beams to structure materials. One of its advantages is that the material processing is fast, repeatable and can be applied at wafer level during the fabrication process of the sensing devices. In this work, zinc oxide sputtered thin films have been processed on alumina substrates using the laser interference lithography tripled Q-switched Nd:YAG laser source with an output wavelength of 355 nm. The aim is to obtain periodic structures on the surface, varying the process conditions in order to increase the surface area of the devices but also to modify the morphological properties of the devices and study their influence on the gas sensing properties of ZnO. The structural characterization has shown that the material changes its morphological properties and two-dimensional patterns have been obtained and implemented in gas sensing devices (including interdigitated electrodes and a back-side heater). Their gas sensing behavior is being researched and compared to the thin film ZnO oxide. Preliminary results show response enhancement in some of the obtained structures.

(ii) 8th Franco-Spanish Workshop IBERNAM-CMC2, 13-14 October 2016, Toulouse (France)

Laser-modified ZnO for Conductometric Sensors

L. Parellada (1,*), I. Castro-Hurtado (1), E. Castaño (1), G-G. Mandayo (1)

(1)   Ceit and Tecnun (University of Navarra)
(*) e-mail corresponding Author

Keywords: ZnO, formaldehyde, gas sensor, laser interference lithography and femtolaser

Formaldehyde (HCHO) is one of the most dangerous volatile organic compounds (VOC's) for human health. The Occupational and Safety Health Administration (OSHA) established a short-term exposure limit of 2 parts per million (ppm) and the National Institute for Occupational Safety and Health (NIOSH) recommends a long-term (30 min) exposure limit of 0.07 ppm of formaldehyde due to the risk of accumulation in indoor environments. As a consequence, a rapid sensor device to detect small concentrations of formaldehyde is needed urgently and this is the aim of this investigation.

Nanostructured materials are promising in this research field since their surface-to-volume ratio is increased, leading to a probable faster response due to gas diffusion improvement. Nevertheless, the research community only started focusing on formaldehyde sensors based on nanostructures a decade ago. Metal oxide nanowires are an example of sensitive layers for formaldehyde sensor although the fabrication procedures are difficult to scale to mass production.

ZnO is an n-type semiconductor with hexagonal wurtzite crystal structure widely used in several applications such as optoelectronics or chemical sensors. Thanks to its properties: chemical stability, sensitivity to different adsorbed gases, non-toxicity and low cost it is one of the two most sensitive and used materials for formaldehyde detection jointly with SnO_2.

In this work, zinc oxide sputtered thin films have been processed on alumina substrates using the laser interference lithography tripled Q-switched Nd:YAG laser source with an output wavelength of 355 nm. The aim is to obtain 2-dimensional structures on the surface, varying the process conditions in order to increase the surface area of the devices but also to modify the morphological properties of the devices and study their influence on the gas sensing properties of ZnO. The structural characterization has shown that the material changes its morphological properties and two-dimensional patterns have been obtained and implemented in gas sensing devices (including interdigitated electrodes and a back-side heater). Their gas sensing behavior is being researched and compared to the thin film ZnO. One of the unique features of LIL technique is that not only produces a change on the surface morphology allowing rugosity control, but also acts as a rapid thermal treatment.

Furthermore, early investigations have been done on the creation of Laser Induced Periodic Surface Structures (LIPPS) on ZnO surface using a femtolaser of 800 nm of wavelength. Preliminary results showed LIPSS structures with a period much lower than usual (≈140 nm).

(iii) 11th Spanish Conference on Electron Devices, 8-10 February 2017, Barcelona (Spain)

Multisensor platform for indoor air quality measurements

J. González-Chávarri[1], E. Hammes[2], L. Parellada[1], I. Castro-Hurtado[1], E. Castaño[1], I. Ayerdi[1],

H. Knapp[2], G.G. Mandayo[1]

[1]Ceit-IK4 and Tecnun (Universidad de Navarra), P. Manuel Lardizabal 15, 20018, San Sebastián, Spain
Telephone: +34 943 212 800 Fax: +34 943 213 076
[2]CSEM, Center Central Switzerland, Untere Gründlistrasse 1, CH-6055 Alpnach, Switzerland
Corresponding author: ggmandayo@ceit.es

1. Abstract

The objective of this work is to develop a platform for a set of three conductometric sensors, able to deliver a controlled flow of indoor air samples in parallel to the three sensors. The system controls, on one hand, the air flow and, on the other hand, adds the capability of humidity control in two different ways: measuring humidity at the input and output, and stabilizing it through a filtering material. This way the performance of conductometric sensors can be enhanced, because one of the main causes of their low specificity is the cross-sensitivity to ambient humidity. The controlled amount of gas arriving at the sensors also avoids possible fluctuations in the sensor signals due to the air flow variations.

2. Platform description and fabrication

The platform has three main elements, as shown in the flow diagram in Fig.1. Following the flow path from the input, the platform firstly has a filtering and drying unit. Next, the three sensors are placed in a module with separate chambers, after that, a flow sensor monitors the amount of flow through the system and finally the pump generating the flow is situated before the air output (see Fig.2).

Plastic components were milled from PMMA (poly-methyl methacrylate) and PEEK (Polyetheretherketone) NBR (nitrile rubber) and silicon gaskets were cut fitting the dimensions of the different parts, to seal them. The different components were glued with epoxy and channels sealed with adhesive foil. The filter for humidity control was made up of silica gel beads sandwiched between particle filters.

The humidity changes are monitored using a Sensirion SHT71 sensors and flow is measured with the Sensirion SDP610 sensor. The pump is a micro vane model Schwarzer Precision SP 135FZ.

Three different sensing materials, whose performance had been previously studied, were implemented in the same alumina chip, reported in [1]: a ZnO nanoneedle sensor, a NiO thin film sensor [2] and a Pt doped thin film SnO_2 sensor [3].

3. Results and discussion

First, the effect of the silica gel on the humidity of the gas flow arriving at the sensors has been tested under different pulses of humid air. The silica gel adsorbs the fast humidity pulses avoiding the resistance change due to humidity in the sensor (Fig. 3)

Then, the performance of the three conductometric sensors (NiO, SnO_2 and ZnO) was tested with benzene, formaldehyde and nitrogen dioxide (Figs. 4, 5, and 6), inside the system, and compared to previous experiments in a different test chamber. Some simulations were carried out to optimize the sensors' position inside the chambers.

The sensors are set to their respective optimal temperatures for the three sensors in order to perform the measurements.

4. Conclusions

A preconditioning platform for three conductometric sensors has been proven to stabilize the sensor response under fluctuating humidity. Three conductometric sensors were measured inside the preconditioning unit for three indoor air pollutants at typical concentrations for indoor air quality measurements, showing adequate detection limits for this purpose.

References

[1] E. Hammes, J. Gonzalez-Chavarri, G.G. Mandayo, H. F. Knapp, P. Ryser "The Transport Phenomena within the Intasense Indoor Air Quality Monitor Design" AIChE Spring Meeting in Austin, TX, USA, 26-30 April 2015

[2] J. González-Chávarri1, I. Castro-Hurtado, I. Ayerdi, E.Castaño, G.G. Mandayo, "ZnO conductometric sensor for indoor air quality measurement inside buildings", Proceedings of the 10th Spanish Conference on Electron Devices, CDE 2015.

[3] I. Castro-Hurtado, J. Herrán, G. G. Mandayo, and E. Castaño "Studies of influence of structural properties and thickness of NiO thin films on formaldehyde detection" Thin Solid Films, 520(3):947–952, 2011.

[4] G. G. Mandayo, E. Castano, F. Gracia, A. Cirera, A. Cornet, and J. Morante, "Strategies to enhance the carbon monoxide sensitivity of tin oxide thin films", Sensors and Actuators B: Chemical, 95(1):90–96, 2003.

(iv) 9th Franco-Spanish Workshop IBERNAM-CMC2, 4-5 October 2018, Tarragona (Spain)

Surface and in depth composition characterization of thin film ZnO processed by Direct Laser Interference Processing

L. Parellada-Monreal (1, 2), M. Martínez-Calderón (1, 2), I. Castro-Hurtado (1, 2),

D. Gamarra (3), J. Lozano (3) and G. G. Mandayo (1, 2, *)

(1) Ceit, Manuel Lardizábal 15, 20018 Donostia/San Sebastián, Spain
(2) Universidad de Navarra, Tecnun, Manuel Lardizábal 13, 20018 Donostia/San Sebastián Spain
(3) Escuela de Ingenierías Industriales, University of Extremadura, Badajoz, Spain
(*) ggmandayo@ceit.es

Keywords: ZnO, DLIP, XPS, TOF-SIMS

ZnO is one of the most stable n-type semiconductors, with a wide direct band gap of 3.37 eV and presents attractive features for device fabrication such a good stability and nontoxicity. Direct Laser Interference Patterning (DLIP) is a nanostructuring technique that uses the interference generated by the interaction of two or more beams to produce a pattern on a surface's material.

In this work, a 2-beam DLIP setup is used to nanostructure one-dimensional (line shape) structures on sputtered ZnO deposited on alumina at two different fluences (85 and 165 mJ/cm^2). The fabricated structures are characterized in order to investigate the laser influence both on the composition of the thin film surface and in the bulk.

From the X-ray Photoelectron Spectroscopy (XPS) it can be concluded that the samples processed by DLIP became richer on Zn, compared to as-grown ZnO thin film. This phenomenon could be explained through an increase of oxygen vacancies regions and/or Zn interstitials, what is an important issue for gas sensing applications.

In order to study the composition in the ZnO depth, the concentration of different ions was measured using a Time of Flight Secondary Ion Mass Spectrometer (TOF-SIMS). In Fig. 1, only ZnO$^+$ and Al^{2+} ions have been plotted, representing the ZnO and alumina behavior, respectively. As a result, sample processed by DLIP at 165 mJ/cm^2, shows an increase of the interface region (indicated in blue on the x axis) between the ZnO and the alumina comparing with the sample processed at 85 mJ/cm^2. The reason is that for the higher fluence, a higher temperature is achieved, so atoms received more energy, and therefore they can diffuse and travel longer distances.
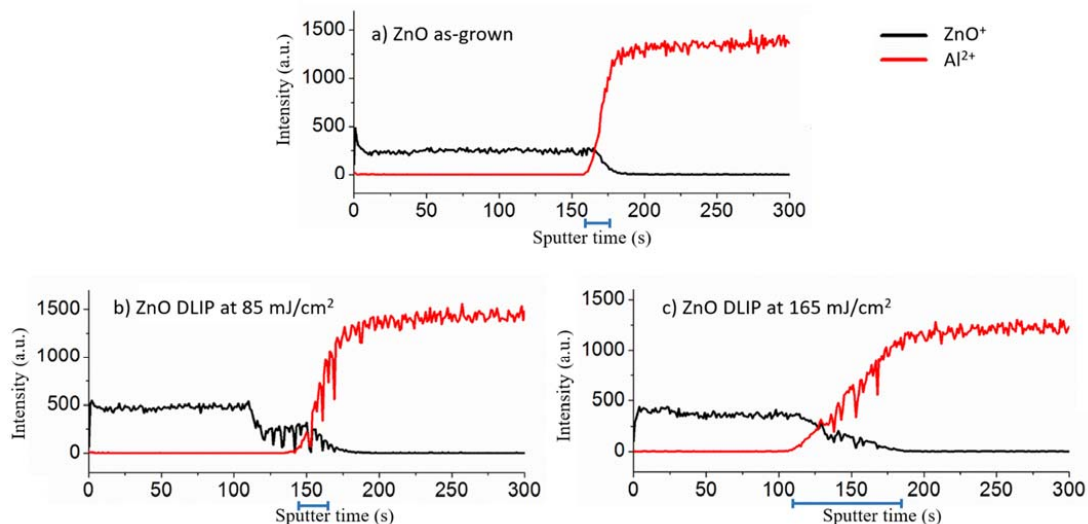

Fig.1: TOF-SIMS measurements of ZnO$^+$ and Al^{2+} ions for the samples (a) ZnO as-grown, (b) ZnO DLIP at 85 mJ/cm^2 and (c) ZnO DLIP at 165 mJ/cm^2.

These results are relevant in order to study the interaction of the material at the thin film/substrate interface under the laser effect, what is crucial for devices that use substrates sensitives to low temperatures.

A.2.2   Posters

(i) SPIE MICROTECHNOLOGIES, 8-10 May 2017, Barcelona (Spain)

Temperature simulation at ZnO surface processed by Laser Interference Lithography

ZnO is a wide band gap and n-type semiconductor with hexagonal wurtzite crystal structure widely used in several applications such as solar cells, transparent electronics, optoelectronics and thin film chemical sensors. The research community has deeply studied ZnO because of its numerous properties: good transparency, high electron mobility, large exciton binding energy and non-toxicity.

Laser interference lithography (LIL) is a technique that uses interference patterns generated from two or more coherent laser beams to structure materials. Without the need of a mask, nanopatterning with LIL is a fast and simple technique that can be applied at wafer level during the device fabrication process.

In this work, zinc oxide sputtered thin films have been processed on alumina substrates using the laser interference lithography tripled Q-switched Nd:YAG laser source with an output wavelength of 355 nm in a 2-beam configuration. The aim is to obtain periodic structures on the surface, varying the fluence of the laser in order to control the surface area processed and compare with ZnO thin film thermal annealed at 600ºC, 700ºC and 800ºC degrees during 4 hours in synthetic air.

The structural characterization has shown that two-dimensional patterns have been obtained and also that the material changes its morphological properties (for example a stress release is observed in the (002) direction, when compared to as-grown ZnO).

In order to understand the periodic structure generated on the surface with this technique, the temperature profile on the surface of the ZnO has been simulated using Matlab. For this purpose optical properties of the films have been measured and used in the simulation of the heat transfer equation at the surface of the ZnO. Temperature evolution with time and distance at different laser fluences have been simulated and compared to morphological results obtained. For fluencies around 165 mJ/cm^2 in as grown samples, the results show up temperatures up to 1800 K few nanoseconds after the laser pulse is sent.

(ii) Eurosensors XXXI, 3-6 September 2017, Paris (France)

Topic: Materials and micro- nano- technology, Microfabrication.

Laser Interferometry for broad area SPR-grating couplers in chemical applications.

M. Moreno-Sereno[1], N. Pérez[2], G. Domenech-Gil[1], L. Parellada[3], M. Martínez-Calderón[3], M. Gómez-Aranzadi[3], N. Darwish[1,4], G.G. Mandayo[3], A. Romano-Rodriguez[1]

1. Department of Electronics, Universitat de Barcelona, Barcelona, Spain
2. Universidad de Navarra, Tecnun, San Sebastian, Spain
3. Ceit and Tecnun, Universidad de Navarra, San Sebastián, Spain
4. Institute of Science and Technology, Klosterneuburg, Austria

Summary

In this work we present the fabrication of SPR (Surface Plasmon Resonance)-grating coupler using Laser Interference Lithography (LIL), giving rise to large area diffraction gratings on a 100 nm-thick gold film. The period of the diffraction grating is $\Lambda = 500$ nm, and the etching depth is 30 nm. The SPR sensor has been tested towards several liquids showing a bulk sensitivity of S=414 nm/RIU.

Motivation and results

SPR is a usual optical technique for label-free biosensing. Surface Plasmons (SP) can be excited at the interface between a metal and a dielectric using a diffraction grating patterned on a gold film [1]. This technique is simpler than Krestchmann's configuration [1] because it does not require a prism nor a mechanical pressure system. The period of the diffraction grating must be submicron and, thus, nanolithography techniques must be used. Electron Beam Lithography (EBL) is an ideal technique for prototyping nanostructured surfaces, in an area of few mm^2. However, time and costs increase linearly with the size of the patterned area. LIL, on the other hand, can be used to define a specific 1D or 2D periodical patterns on a photoresist over a large area and cost-effectively.

In this work we have used LIL to fabricate diffraction gratings within a large area, about 1 cm^2, by using two laser beam interference from a frequency-tripled Nd:YAG laser, at λ=355nm, on a photoresist on top of a 100 nm-thick gold film. In order to pattern the photoresist, it was exposed to a 16 mJ single pulse of 8 ns, developed and etched by Reactive Ion Etching (RIE). Trenches 250 nm wide and 30 nm deep were obtained over a circular area of 1 cm^2. In Figure 1 a photograph of the optical SPR-G sensor is shown, and in Figure 2 a detailed SEM micrograph of the etched grating. The LIL technique has been used by the authors in [2] for patterning diffraction gratings on Si_3N_4.

We have used spectral interrogation, with a broadband source and a spectrometer SD-2000, both from Ocean Optics, to measure the reflectivity of the SPR-G sensor. Figure 3 is a typical reflection spectrum showing the dip in the measurement, corresponding to the resonance. A detailed description of the optical set-up can be found in [3]. The SPR sensor is scanned using optomechanical components from THORLABS, two low-cost linear actuators and a MSP430 microcontroller from TEXAS™. Figure 4 shows the scanning map with the DIP resonance wavelength around 650nm as a function of the position. Finally, the sensitivity of the sensor for different liquid external media, has been measured. The bulk sensitivity resulted in S = 414 nm/RIU, similar to other literature results [3]. At this moment, we are testing the samples of 50 nm-thick gold film and different etching depths.

Word count: 461

References

[1] Jirí Homola - Editor (2006): Surface Plasmon Resonance Based Sensors. Springer Series on Chemical Sensors and Biosensors.
[2] P. Rodríguez-Franco et al. (2013): Fabrication of broad area optical nanostructures for high throughput chemical sensing. Sensors and Actuators B **187**, 356-362.
[3] S. Kumari et al. (2016): Nano-imprint gold grating as refractive index sensor. AIP Conference Proceedings 1728, 020539 ; doi: 10.1063/1.4946590.

Corresponding author

M. Moreno-Sereno, C/ Martí i Franquès 1, 08028 Barcelona Spain, phone: (+34) 934029150, mmoreno@el.ub.edu

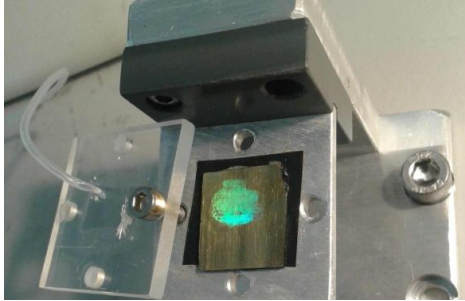*Topic: Materials and micro- nano- technology, Microfabrication.*

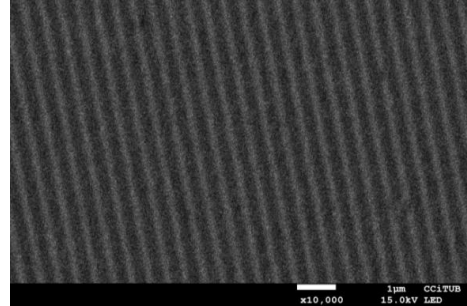*Figure 1: Photograph of the area of the gold film patterned with a diffraction grating.*

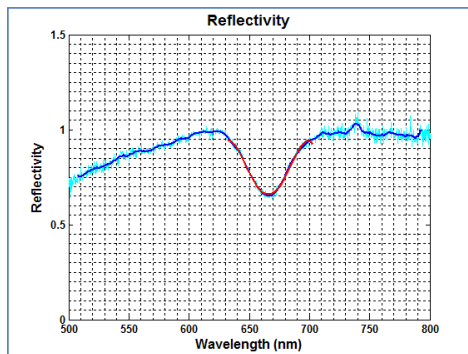*Figure 2: SEM photograph of the $\Lambda=500nm$ period diffraction grating.*

Figure 3: Reflectance spectrum showing the dip at $\lambda_{DIP}=670nm$.
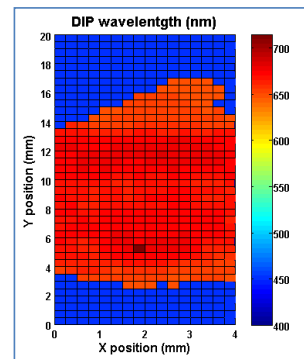

Figure 4: Scanning map of the surface of SPR sensor with water as external medium.

(iii) Workshop IBERNAM, 28-29 September 2017, Tordesillas (Spain)

Laser-induced periodic surface structures on ZnO thin film for NO₂ detection

L. Parellada-Monreal, Miguel Martínez-Calderón, Irene Castro-Hurtado, Ainara Rodriguez and Gemma G. Mandayo*
Ceit-IK4 and Tecnun (University of Navarra), San Sebastián-Donostia, Spain
e-mail: lparellada@ceit.es

Laser-induced periodic structures (LIPSS) were discovered by Birnbaum in 1965 [1] and during the last two decades the research community has been trying to understand their origin and generation mechanism [2]. LIPSS structures have been widely used in many kinds of applications: controlling cell growth direction [3], modifying the hydrophobic/hydrophilic properties of materials [4] or generating structural color [5].

Nevertheless, as far as gas sensing is concerned, it has never been used for a possible enhancement of the response of sensing materials. Due to the increase of surface-to-volume ratio generated by the LIPSS on the surface of the semiconductor, a better sensitivity of the sensor is expected. Generating LIPSS with a femtosecond laser on the ZnO surface is an innovative technique able to modify the surface morphology and also increase the surface area leading to an enhancement of the gas response.

In order to understand the effect of the LIPSS on the ZnO response, sensors using ZnO thin films with and without LIPSS have been compared. The optimum temperature has been studied between 200 ºC and 400 ºC for both sensing devices with a constant concentration of 5 ppm of NO₂. In Fig. 1 the response of both sensors is presented at their optimum temperature, where the sensor with LIPSS exhibits about three times higher response compared with thin film.
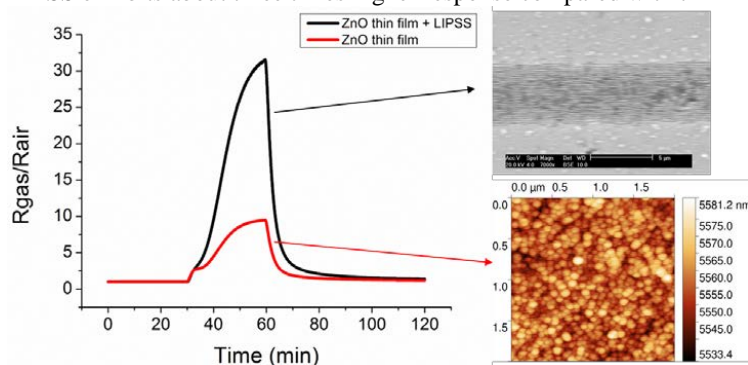

Fig. 1. Sensor response to 5 ppm of NO₂ at an operating temperature of 321 ºC and 325 ºC for the sensor with LIPSS and without them (left) and SEM image of the LIPSS on the ZnO (right-up) and AFM image of ZnO surface without LIPSS (right-down).

[1]   *Birnbaum, M. J. Appl. Phys.* **1965**, *36* (*11*), *3688–3689*.
[2]   *Huang, M.; Zhao, F.; Cheng, Y.; Xu, N.; Xu, Z. ACS Nano* **2009**, *3* (*12*), *4062–4070*.
[3]   *Wang, X.; Ohlin, C. A.; Lu, Q.; Hu, J. Biomaterials* **2008**, *29* (*13*), *2049–2059*.
[4]   *Wu, B.; Zhou, M.; Li, J.; Ye, X.; Li, G.; Cai, L. Appl. Surf. Sci.* **2009**, *256* (*1*), *61–66*.
[5]   *Ionin, A. A.; Kudryashov, S. I.; Makarov, S. V; Seleznev, L. V; Sinitsyn, D. V; Golosov, E. V; Ol'ga, ·; Golosova, A.; Kolobov, Y. R.; Ligachev, A. E. Appl. Phys. A* **2012**, *107*, *301– 305*.

(iv) Eurosensors XXXII, 9-12 September 2018, Graz (Austria)

Advanced Functional Materials for Sensing and Actuating

Enhancement of gas sensing response on WO₃ thin films processed by Direct Laser Interference Patterning

L. Parellada-Monreal [1], M. Martínez-Calderón [1], I. Castro-Hurtado [1], S. M. Olaizola [1], G. Zonta [2, 3],

S. Gherardi [3], C. Malagù [2, 3] and G. G. Mandayo [1]

[1] *Ceit-IK4 and Tecnun, University of Navarra, San Sebastián-Donostia, 20018, Spain*
[2] *Department of Physics and Earth Science, University of Ferrara, Ferrara, 44122, Italy*
[3] *SCENT, S.r.l., Ferrara, 44124, Italy*

1. Summary

Direct Laser Interference Patterning (DLIP) technique has been used to generate a line pattern on the surface of WO₃ thin films, due to the interference of two coherent laser beams, modifying its surface morphology and physical properties. Gas sensing devices based on WO₃ thin films annealed at 600 ºC and nanostructured by DLIP have been fabricated and compared to samples simply annealed at the same temperature.
The sensors have been tested under NO₂ atmospheres. Their optimal operating temperature is 200 ºC, with responses about four times higher for the sensors with annealing + DLIP compared with only annealing at concentrations as low as 2, 1 and 0.5 ppm. This great enhancement on the response for the sensors processed by DLIP indicates modifications on the crystallographic structure, aside from the morphological one.

2. Motivation and results

DLIP is a one step and automatable technique able to generate submicrometric structures without the need of a mask [1]. The main advantage is that the process is fast, repeatable and can be implemented at wafer level. This method has been previously investigated on other semiconductors as ZnO [2], but has never been used to tune crystallographic characteristics for an enhancement of the sensitivity on gas sensing applications. From previously published work about WO₃ processed by 3 and 4 beam DLIP [3], innovative properties have been shown, indicating a possible application on the sensing field.

As can be appreciated in Fig. 1 (a), thermal annealed WO₃ at 600 ºC presents a flat surface with a roughness around 7 nm. By contrast, when the sample is processed by DLIP at a fluence of 50 mJ/cm², a hole structure appears in a periodic line-pattern (Fig. (b) and (d)). The holes have an average depth of 16 nm. This characteristic indicates that the holes area is where higher intensity has been accumulated and consequently a higher temperature has been reached, melting and removing the material. As a consequence, there is an increase of the total surface exposed to the gas for the sensors processed by DLIP, what could explain the sensitivity enhancement. Nevertheless, structural properties of the material have also been modified and may also have an influence on the NO₂ detection mechanism. On Fig. 2, the response obtained by entering pulses of 2, 1 and 0.5 ppm of NO₂ in the testing chamber with the sensors at the optimal working temperature has been plotted. As shown, sensors processed by DLIP present an enhance in the response for all the concentrations.

Word count: 406

References

1. Berger. J. et al. Controlling the optical performance of transparent conducting oxides using direct laser interference patterning. *Thin Solid Fillms.* **612,** 342–349 (2016).
2. Parellada-Monreal, L. *et al.* Study of sputtered ZnO modified by Direct Laser Interference Patterning: Structural characterization and temperature simulation. *Appl. Surf. Sci.* **441,** 331–340 (2018).
3. Castro-Hurtado, I. *et al.* Structural and optical properties of WO₃ sputtered thin films nanostructured by laser interference lithography. *Appl. Surf. Sci.* **276,** 229–235 (2013).

Corresponding author

Laura Parellada-Monreal, Paseo de Manuel Lardizábal 15, San Sebastián-Donostia, 20018, Spain, (+34) 943212800, Fax: (+34) 943213076, lparellada@ceit.es
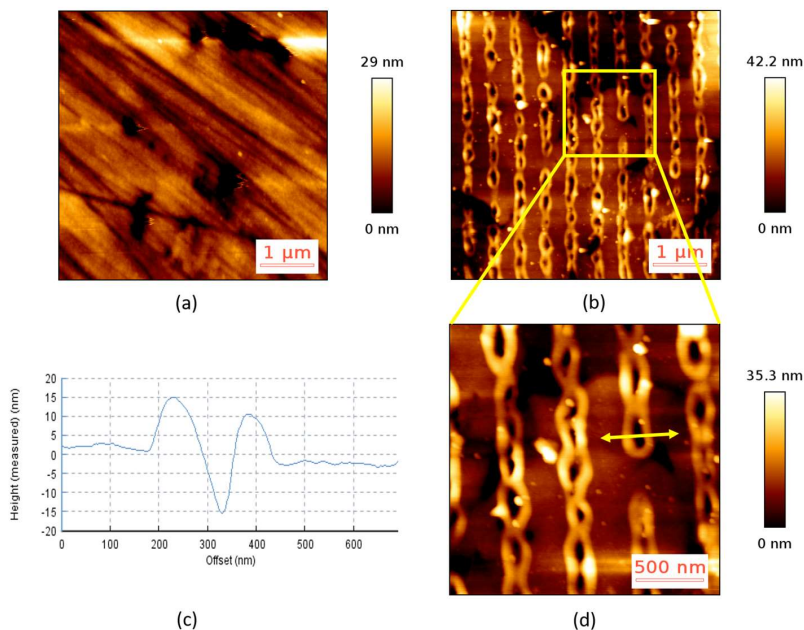

Figure 1. AFM tapping mode images of WO3 thin film (**a**) annealed at 600 ºC; (**b**) annealed at 600 ºC and processed by DLIP at 50 mJ/cm². (**c**) Section profile of the line point out in (**d**); (**d**) zoomed image of the sample annealed at 600 ºC and processed by DLIP.
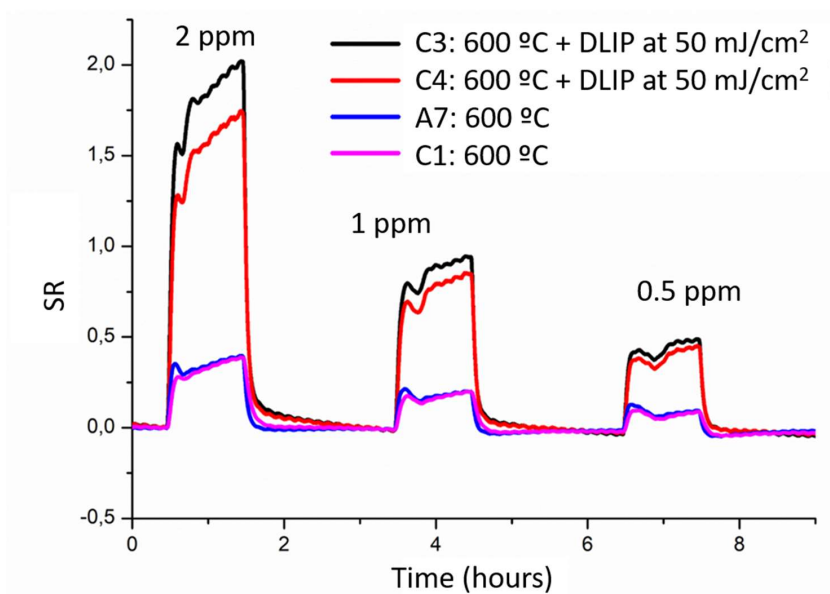

Figure 2. Pulses of 2, 1 and 0.5 ppm of NO₂ for WO₃ thin film sensors annealed at 600 ºC, processed and non-processed by DLIP at 50 mJ/cm². SR is defined as $R_{air}/R_{gas} - 1$, where Rair is the resistance of the sensor in air, and Rgas is the resistance in presence of the gas.

(v) 11th Ibero-American Congress on Sensors, 17-20 September 2018, Barcelona (Spain)

Ibersensor 2018

NANOSTRUCTURED MOX MATERIALS FOR GAS SENSORS APPLIED TO ENVIRONMENT

C.Cané[1], S. Vallejos[1], M.Salleras[1], M.Tomic[1], E. Figueras[1], I. Gràcia[1],
G Domènech-Gi[,2], E. López-Aymerich[2], M. Moreno[2], P. Pellegrino[2], A. Romano-Rodríguez[2]
L. Parellada-Monreal[3], I. Castro-Hurtado[3], I. Ayerdi[3], G.G. Mandayo[3]
[1] *Centre Nacional Microelectrònica (IMB-CNM, CSIC), Campus UAB, Bellaterra, Spain.*
[2] *Institute of Nanoscience and Nanotechnology (IN2UB) and Department of Electronic and Biomedical
Engineering, Universitat de Barcelona (UB), Barcelona, Spain.*
[3] *Ceit and Tecnun, University of Navarra, San Sebastian, Spain.*
[*]*e-mail: cane@cnm.es*

Introduction

In Spain, three groups are working together on the development of enhanced sensitive materials for gas sensors as part of the TEMINAIR+ project on new tools for environmental control. In this application it is important to monitor key parameters that allow making predictions and decisions efficiently. New components that can be operated with ultra-low power consumption for high autonomy at low cost are needed, fabricated with eco-friendly materials and robust enough to have long-term stability and full connectivity to be part of tools such as wireless sensor networks (WSN) or IoT nodes. Semiconductor Metal Oxide (MoX) materials are a good alternative for gas sensing because they satisfy these requirements.

Methods

Gas sensors based on different MoX materials are of interest as they provide a simple change of resistance that is related to the type and concentration of the gas to which sensors are exposed [1]. A variety of MoX materials are being studied and developed in the project in order to get faster response, higher sensitivity, better selectivity and higher stability compared to commercial devices. Apart from the well-known SnO_2, TEMINAIR+ groups are working with other materials like ZnO, In_2O_3, and WO_3. The current trend is to nano-pattern the material by top-down approaches like modifying sputtered layers with Direct Laser Interference Patterning (DLIP) [2] or by using bottom-up techniques and growing 1D nanostructures with different CVD techniques [3,4]. This last approach allows both the direct and indirect deposition of single or arrays of nanostructures also modified with catalytic nanoparticles on different types of substrates.

Results

Functional devices have been obtained on alumina, Si-MEMS and flexible substrates depending on the requirements of the application. In figure 1, a picture showing AACVD nano structured WO_3, single In_2O_3 nanowires grown by CVD and ZnO patterned with DLIP, are presented. CVD techniques allow tuning morphologies of the material (see figure 2), to obtain different responses to gases. Chemical tests are being carried out for gases of interest for indoor and outdoor air quality control (mainly CO_2, NO_X, SO_X, CO and Volatiles) at concentration ranges around 100 ppm, with very promising results that will be shown at the conference.

Conclusions

The use of the Direct Laser Interference Patterning (DLIP) technique for structuring is shown as a more simple and faster approach compared to other top-down techniques. In addition, CVD has also allowed the direct integration of 1D nano-patterned structures on Silicon micromachined and polymeric substrates, with good results. The main objective is to develop new technologies for gas sensors that are robust and that may bring enhanced performances compared to commercial devices and that can be easily scaled-up in the future. The new techniques widen the palette of techniques of the consortium for gas sensing that also include optical (NDIR) and mass (SAW) devices and systems.

Ibersensor 2018

References

[1] E. Comini, "Metal oxide nanowire chemical sensors: innovation and quality of life," Materials Today, vol. 19, pp. 559-567, 2016.

[2] L. Parellada-Monreal, I. Castro-Hurtado, M. Martínez-Calderón, A. Rodriguez, S.M. Olaizola, D.Gamarra, J.Lozano, G.G.Mandayo. "Study of sputtered ZnO modified by Direct Laser Interference Patterning: Structural characterization and temperature simulation". Applied Surface Science, 441, 331-340. 2018.

[3] S. Vallejos, I. Grácia, O. Chmela, E. Figueras, J. Hubálek, and C. Cané, "Chemoresistive micromachined gas sensors based on functionalized metal oxide nanowires: Performance and reliability," Sensors and Actuators B: Chemical, vol. 235, pp. 525-534, 2016.

[4] G. Domènech-Gil, S. Barth, J. Samà, P. Pellegrino, I. Gràcia, C. Cané, A. Romano-Rodriguez. "Gas sensors based on individual indium oxide nanowire". Sensors and Actuators B 238 (2017) 447–454.
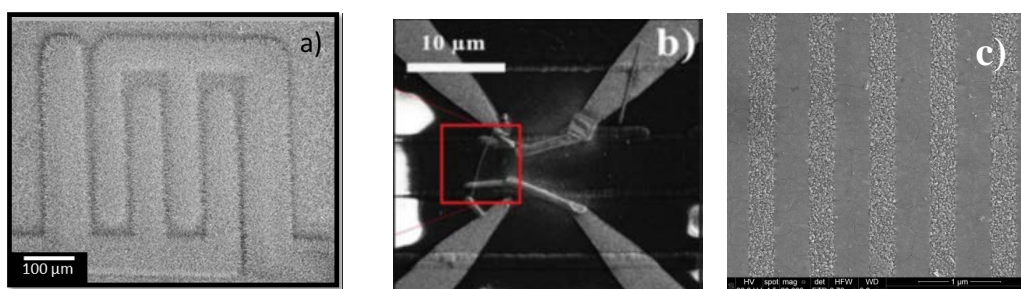
Figure 1: a) Mesh of 1-D WO3 nanowires grown on top of a polymeric foil, b) single In_2O_3 wire on top of a Si- micromachined microhotplate, and c) Sputtered layer of ZnO patterned by DLIP.
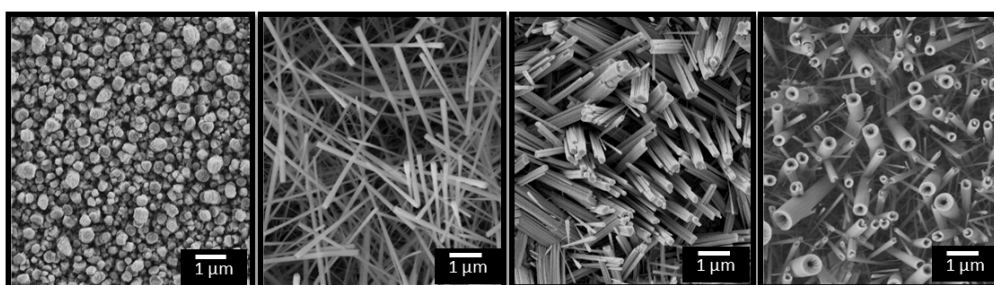

Figure 2: SEM images of tungsten oxide grown via AACVD (from polycrystalline to various nanostructured morphologies).

(vi) 12th Spanish Conference on Electron Devices, 14-16 November 2018, Salamanca (Spain)

ZnO thin film processed by Direct Laser Interference Patterning for formaldehyde detection

Laura Parellada-Monreal, Irene Castro-Hurtado, M. Martínez-Calderón, Santiago M. Olaizola,

Gemma G. Mandayo

Ceit-IK4 and Tecnun, University of Navarra, San Sebastián-Donostia, Spain
lparellada@ceit.es

1. Abstract

Direct Laser Interference Patterning (DLIP) is a fast nanostructuring technique able to generate periodic patterns in the submicrometric range, what modifies the morphology and structural properties of semiconductors [1]. In ZnO thin films, DLIP acts as a thermal treatment from the crystallographic point of view, so it could replace it for example in gas sensing devices.

2. Experimental

A ZnO sensing layer is deposited on top of Pt electrodes by photolithography followed by RF sputtering in an Argon atmosphere (ZnO target 99.999 % purity) in a Pferiffer-Iontech system. Subsequently, the ZnO thin films are annealed in a quartz oven at two different temperatures: 600 °C and 700 °C during 4 hours in synthetic air. Other samples are first deposited directly on the alumina substrate and then processed by 2-beam DLIP setup with a tripled Q-switched Nd:YAG laser source provided by Thales, the Saga HP model (with a wavelength of 355 nm and a pulse duration of 8 ns) to obtain one-dimensional (1D) interference patterns on the surface. In this case, the Pt interdigitated electrodes are deposited afterwards on top of the ZnO. On the DLIP setup, an optical beam splitter divides the laser source into two different beams, which are reflected on mirrors and finally addressed towards the sample surface with the same incident angle. To study the influence of the laser fluence, the samples were processed at 85 mJ/cm^2 and 165 mJ/cm^2 and a single shot was used in all the processes. At the back side of the sensing device, a Pt resistance is used as a heater to reach working temperatures between 200 °C and 400 °C.

The films topography is studied with a SEM Quanta 3D FEG from FEI Company. The crystal structure is characterized by Grazing Incident X-ray Diffraction (GIXRD) at 2° of incident angle by means of a PANalytical X' PERT PRO MRD diffractometer (Cu Ka1, k = 1.5406 Å and Cu Ka2, k = 1.544 Å).

The gas test is carried out inside a sealed stainless steel chamber. The formaldehyde (HCHO) vapour is taken from a certified bottle (Air Liquide) of 50 ppm mixed with synthetic air. The gas mixture is obtained by a system consisting of PC-controlled mass flow controllers (MFCs) Bronkhorst Hi-Tech.

In this work, the response of the devices is defined as follows: $Response = (R_0 - R)/R_0 \cdot 100$, where R_0 is the resistance of the sensor in air, and R is the resistance in the presence of HCHO.

3. Results

As can be appreciated in Fig.1 (a), a linear pattern is obtained with two different textures in the case of the lower fluence (granular and smooth) and smooth with particles due to possible ablation of the material for the higher fluence (Fig.1 (b)). By contrast, for the samples annealed at 600 °C and 700 °C, the morphology shows homogenous granular ZnO surface (Fig.1 (c) and (d)).

As shown in Fig.2, for all the samples, the peaks of the wurtzite ZnO structure have been identified (ICDD PDF card #00-036-1451). As a general trend, the laser treatment is acting similarly to the annealing process from the crystallographic point of view, since it improves the crystal structure with the temperature.

In Fig.3, the response for the different sensors heated at 420 °C under 20 ppm of HCHO is plotted. The devices annealed at 600 °C and 700 °C and the processed by DLIP at the lower fluence show very similar response, between 23% and 26%, indicating that DLIP could replace the annealing process, avoiding the long time of the thermal treatment. In the case of the sample processed by DLIP at the higher fluence (165 mJ/cm^2), the response decreases down to 16%, probably due to the ablation.

The responses for different concentrations of HCHO (20, 10, 5 and 2.5 ppm) are shown for the sensors annealed at 600 °C and processed by DLIP at 85 mJ/cm^2.

4. Conclusions

ZnO thin film sensors processed by DLIP have been compared to annealed sensors at 600 °C and 700 °C for HCHO detection. The sensors processed at the lower laser fluence (85 mJ/cm^2) present similar responses than the annealed samples, what indicates that could be an alternative of the long annealing process.

References

[1] I. Castro-Hurtado, et al. Structural and optical properties of WO3 sputtered thin films nanostructured by laser interference lithography, Appl. Surf. Sci. 276 (2013) 229–235.
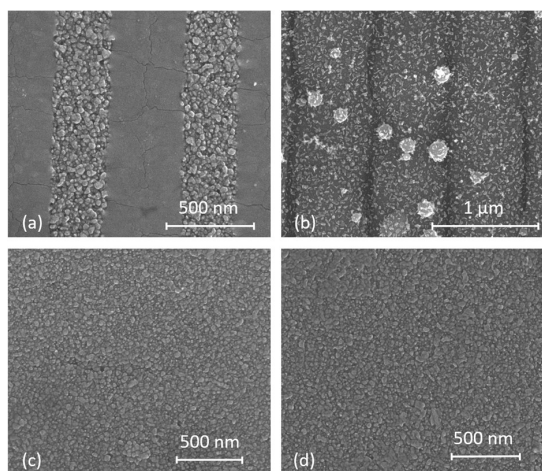
Fig.1. SEM images of ZnO thin film processed by DLIP at 85 mJ/cm^2 (a), at 165 mJ/cm^2 (b), annealed at 600 ºC (c) and at 700 ºC (d).
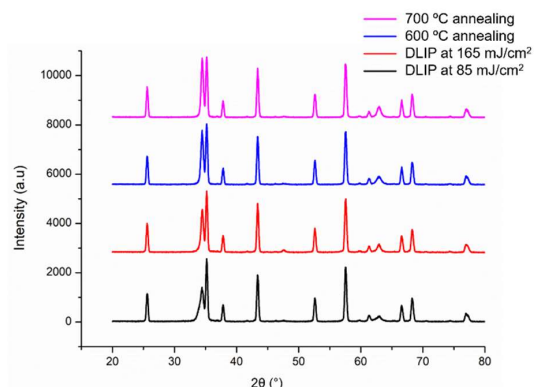

Fig.2. GIXRD of the ZnO thin films processed by DLIP at 85 mJ/cm^2 and 165 mJ/cm^2 and annealed at 600 ºC and 700 ºC.
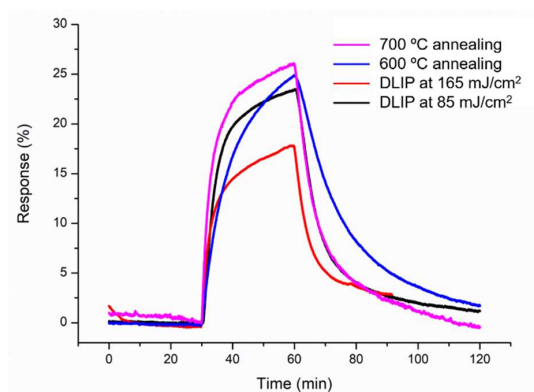

Fig.3. Response of the different sensors at 420 ºC under 20 ppm of HCHO.
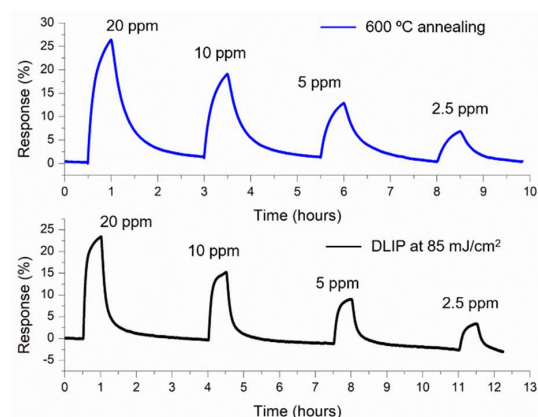

Fig.4. Sensor response for 20, 10, 5 and 2.5 ppm of HCHO at 420 ºC for the sensor annealed at 600 ºC and as grown processed by DLIP at 85 mJ/cm^2.